NASA CONTRACTOR
REPORT

NASA CR-1690

ROCKET MEASUREMENTS OF UPPER ATMOSPHERIC NITRIC OXIDE AND THEIR CONSEQUENCES TO THE LOWER IONOSPHERE

by Luiz Gylvan Meira, Jr.

Prepared by
UNIVERSITY OF COLORADO
Boulder, Colo. 80302
for

NATIONAL AERONAUTICS AND SPACE ADMINISTRATION •• WASHINGTON, D. C. •• FEBRUARY 1971

1. Report No. NASA CR-1690	2. Government Accession No.	3. Recipient's Catalog No.
4. Title and Subtitle ROCKET MEASUREMENTS OF UPPER ATMOSPHERIC NITRIC OXIDE AND THEIR CONSEQUENCES TO THE LOWER IONOSPHERE		5. Report Date February 1971
		6. Performing Organization Code
7. Author(s) Luiz Gylvan Meira, Jr.		8. Performing Organization Report No.
9. Performing Organization Name and Address Laboratory for Atmospheric & Space Physics University of Colorado Boulder, Colorado 80302		10. Work Unit No.
		11. Contract or Grant No. NGL-06-003-064
		13. Type of Report and Period Covered
12. Sponsoring Agency Name and Address National Aeronautics and Space Administration Washington, D. C. 20546		Contractor Report
		14. Sponsoring Agency Code

15. Supplementary Notes

16. Abstract   The nitric oxide density profile in the upper atmosphere between 70 and 110 km was measured with scanning ultraviolet spectrometers aboard two Nike-Apache rockets on 31 January and 6 February 1969. The observed nitric oxide density profile has a maximum of about $10^8 cm^{-3}$ at 105 km, and a minimum of about $10^7 cm^{-3}$ at 85 km. Photochemical equilibrium is prevalent at about 85 km while mixing dominates below that altitude. A model in which nitric oxide is formed from $N(^2D)$ atoms can explain the observed features of the height profile, provided that the recombination of nitric oxide ions produces excited nitrogen atoms more efficiently than ground state atoms. The contribution made by nitric oxide ionization by solar Lyman-alpha to the total ions production is dominant in the middle D region (below 90 km) for the solar activity level at the time of the experiments. Dissociative recombination of nitric oxide ions is the main loss process in the region about 85 km. Below that height, a faster mechanism is required.

17. Key Words (Selected by Author(s)) Rocket Measurements, Nitric Oxide, Lower Ionosphere	18. Distribution Statement Unclassified - Unlimited		
19. Security Classif. (of this report) Unclassified	20. Security Classif. (of this page) Unclassified	21. No. of Pages 144	22. Price* $3.00

FOREWORD

The nitric oxide density profile in the upper atmosphere
was determined from the measurement of fluorescence-scattered
solar radiation in the (1,0) gamma band at 2149 Å. Two sets
of observations were made with scanning ultraviolet spectro-
meters aboard Nike-Apache rockets. The flights were launched
from Wallops Island, Va., on 31 January and 6 February 1969,
with a solar zenith angle of about 60 degrees. Nitric oxide
densities were derived for the region from 70 to 110 km.
Careful consideration of the Rayleigh scattering contribution
to the observed airglow allows for an improvement over past
nitric oxide measurements in the mesosphere.

It is found that the nitric oxide density profile has a
maximum of about 10^8 cm^{-3} at 105 km, and a minimum of about
10^7 cm^{-3} at 85 km. From the observed densities, it concluded
that photochemical equilibrium is prevalent above an altitude
between 85 and 95 km, while mixing dominates below that altitude.
Quantitative consideration is given to a model for the nitric
oxide chemistry in which excited atomic nitrogen in the (^{2}D)
state is responsible for its formation. This model can explain
the significant observed features of the height profile, provided
that the recombination of nitric oxide ions produces excited
nitrogen atoms more efficiently than ground state atoms.

The contribution made by nitric oxide ionization by solar
Lyman-alpha to the total ion production is found to be dominant
in the middle D region (below 90 km, for the solar activity
level at the time of the experiments). It is concluded that
dissociative recombination of nitric oxide ions is the main
loss process in the region above 85 km. Below that height,
however, a faster mechanism is required.

ACKNOWLEDGEMENTS

TABLE OF CONTENTS

LIST OF FIGURES

LIST OF TABLES

CHAPTER I

INTRODUCTION

The existence of the ionosphere, a region of the upper atmosphere where free electrons exist in significant amounts, was first suggested last century in connection with variations in the geomagnetic field, and later as an explanation for the propagation of short-wave radio signals to large distances around the curvature of the Earth. The several regions of the ionosphere have been studied intially with ground-based radio propagation techniques and in the last two decades with the help of in situ rocket measurements; satellites have also been used to study the upper ionospheric regions. The result of these efforts has been an understanding of the major processes responsible for the formation of the E and F regions (above roughly 100 km). (See, e.g., Ratcliffe and Weekes, 1960, and Whitten and Poppoff, 1965)

The D region (the lower portion of the ionosphere, between 60 and 90 km) is important practically for the propagation of short-wave radio signals in spite of its relatively low electron densities ($\leq 10^4$ cm^{-3}, contrasted with 10^5 cm^{-3} in the E region and 10^6 in the F region): the higher neutral densities and consequently higher electron collision frequencies make the D region the site of most of the absorption of sky-wave radio signals by a transfer of energy from the electromagnetic waves into the motion of ambient particles.

The basic processes thought to be responsible for the formation of the D region were presented in the literature in a comprehensive form almost a decade ago (Nicolet and Aikin, 1960), with the notable exception of ionization of $O_2(^1\Delta)$ (Hunten and McElroy, 1968). The details of the mechanisms involved have turned out to be much harder to explain, one of the reasons being the relatively large role played by minor atmospheric neutral constituents in this region.

Ion-pair production in the D region is believed to be due to X-rays in its upper portion, Lyman-alpha ionization of nitric oxide and extreme ultraviolet (EUV) ionization of $O_2(^1\Delta)$ in the middle, and cosmic ray ionization in its lower portion (see, e.g., Bowhill, 1969). The Lyman-alpha ionization of nitric oxide was first suggested as a source of ions by Nicolet (1945). Its importance is based on the existence of a "window" in atmospheric absorption by molecular oxygen at the wavelength of the strong solar hydrogen Lyman-alpha line, which makes this radiation able to penetrate to mesospheric levels, and on the relatively low ionization potential of nitric oxide as compared to more abundant neutral atmospheric constituents. The quantitative evaluation of this source of ions depends critically on the knowledge of nitric oxide densities, since its ionization cross-section and the Lyman-alpha flux are known with reasonable certainty.

The purpose of this work is to measure nitric oxide densities and to assess the importance of its ionization as a source of ions in

2

the daytime mid-latitude D region. Also, we consider the possible implications of the measurements to the nitric oxide chemistry and to the D region ion chemistry. The importance of neutral nitric oxide in this latter context is derived from the fact that ions of major atmospheric constituents undergo fast charge transfer reactions with nitric oxide (see Chapter VI).

An upper limit to nitric oxide densities has been set by Jursa et al., (1959) from a solar absorption experiment, and measurements have been made by Barth (1966) and Pearce (1969d) from resonance fluorescence of the gamma bands. A discussion of these measurements is presented in Chapter IV. The determination of nitric oxide densities reported here are, however, the first to be performed during daytime conditions and with good height resolution in the D region. Furthermore, an improved data analysis is believed to make these the best determinations to date (see Chapter IV).

The nitric oxide density profile was measured twice in the region from 70 to 110 km by observing the intensity of fluorescence scattering in the (1,0) gamma band (Barth, 1964) at 2149 Å, with rocket-borne ultraviolet spectrometers similar to that flown by Pearce (1968). The flights took place from Wallops Island, Va.: rocket NA14.389UA on 31 January 1969 and rocket NA14.390UA on 6 February 1969. These flight numbers are associated with the data in the text.

In Chapter II the experiments are described from the point of view of the instrument. Details of the laboratory calibration of the spectrometers and of the data handling process are presented in Appendices A and B respectively. The rather elaborate computer data processing was necessary in view of the need to take into account properly the Rayleigh scattering by the atmosphere, which contributes a substantial background to the UV airglow at the wavelengths of interest (~ 2150 Å).

Chapter III describes the Rayleigh scattering background problem and the method used to subtract its contribution to the observed fluxes. Details of the geometry of the polarization of Rayleigh scattering are presented in Appendix C.

The apparent emission rates from the nitric oxide (1,0) gamma band are derived in Chapter IV by integration of the measured specific fluxes and corrections for the deviations from a vertical line of sight. These rates are differentiated to yield volume emission rates which are in turn interpreted in terms of local densities of nitric oxide, for a single fluorescence scattering mechanism. It is shown also that the atmosphere is optically thin in the spectral region of interest, with regard to absorption by ozone, absorption by molecular oxygen, Rayleigh scattering by air, and fluorescence scattering by nitric oxide.

The measured densities of nitric oxide are found to be significantly lower than those found in a previous determination for the

same height range (Pearce, 1969d). The discrepancy is attributed to the Rayleigh scattering contribution to the UV dayglow (see Chapter IV).

In Chapter V, the photochemistry of nitric oxide is discussed in the light of the measured density profiles. Reaction of ground-state nitrogen atoms with oxygen molecules is found to be too slow to explain the observed values. Consideration is given to the suggestion by Norton (1967) that the nitrogen atoms might be in the electronically excited (^2D) State.

Calculations are performed for the photochemical equilibrium densities of atomic nitrogen, in the ground and excited states, and nitric oxide, using the atmospheric data from Appendix E. It is concluded that the observed nitric oxide profiles can be explained in terms of a photochemical equilibrium above 90 km, with production by $N(^2D) + O_2$ and loss by $N(^4S)$ + NO as the dominant processes; below that altitude, mixing is found to be the dominant mechanism, based on the very long lifetime against chemical destruction.

In Chapter VI, the ion production rate is computed for Lyman-alpha ionization of nitric oxide, using the observed NO profile and an estimate for the Lyman-alpha flux outside the atmosphere. Attenuation of that radiation by molecular oxygen is taken from a rocket measurement on the same day. It is found that indeed nitric oxide photoionization is the major source of ions in the middle D region, at least for the solar activity level at the time of the measurements.

Also, dissociative recombination of nitric oxide ions is found to be too slow a process to explain the observed ion densities in terms of the ion production rate computed from the experimental nitric oxide. Consideration is given to an alternate loss mechanism involving water cluster ions (Fehsenfeld and Ferguson, 1969), and the required rate coefficient is derived.

A substantial amount of other atmospheric data was used not only in Chapters V and VI, but also in the determination of the Rayleigh scattering background (Chapter III). These are presented in Appendix E in a unified fashion. Some of the data were obtained by other rocket experiments flown on the same days as ours. These experiments were all part of a joint effort coordinated by the University of Illinois to study the lower ionosphere.

CHAPTER II

THE EXPERIMENT

The experimental portion of this work consisted of measuring the nitric oxide dayglow in the (1,0) and (2,0) gamma bands (2149 and 2047 Å respectively) by means of two almost identical scanning ultraviolet spectrometers flown on Nike-Apache sounding rockets.

The instruments were very similar to those used by Pearce (1968); our description will thus be brief. Each rocket payload consisted of an Ebert-Fastie monochromator, photomultiplier tube housing and an electronics package, besides the standard telemetry and instrumentation section.

Both the electronics package and the photomultiplier tube housing (detector head) were vacuum sealed to maintain a pressure of one atmosphere inside the experiment throughout the flight.

The monochromators were operated in first order; actually, in one instrument the grating was facing the exit slit (14.389) and in the other, it was facing the entrance slit (14.390). There was no noticeable difference in the amount of light scattered inside the instrument due to the change in grating orientation.

The instruments used Electro Mechanical Research (EMR) photomultiplier tubes, model 542F-08-18, operated at 2500 V, approximately. Their CsTe cathodes and LiF windows provided a response from 1100 to 3000 Å. The vacuum sealing suprasil window in front of the tube raised the high frequency cut-off to 1900 Å.

Plane replica gratings were used with 3600 lines/mm, blazed at 25°36'. The useful area was 64 x 64 mm. The gratings were rotated by means of an arm, spring-pressed against a cam driven by a synchronous motor. The motor in turn was driven by a 400 cps signal monitored from the ground through a telemetry channel. The cam was shaped so as to scan 150 Å in 3 seconds and then scan the same spectral region in the opposite direction in another 3 seconds. A micro-switch was actuated once each cam revolution, providing a fiducial mark on two of the telemetry channels (high gain data and 400 cps monitor). In the first case, the height of the fiducial mark was also a measure of the high voltage applied to the photomultiplier tube.

A solid-state electrometer transformed the current signal from the photomultiplier tube into a 0 to 5 V signal appropriate for the telemetry input. A voltage amplifier with a tenfold gain fed a second telemetry data channel. These will be referred to as low gain and high gain data channels respectively in the description of the data reduction process.

The photometric calibration of the instruments is described in Appendix A. These results, with other characteristics of the instruments, are summarized in Table II-1.

An excellent check of the calibration of the instruments was provided by the comparison of computed with observed values of the Rayleigh scattered radiation (see Chapter IV). This test indicates that column emission rates measured with our instruments might be too high by a factor of at most 13%.

Both flights took place from Wallops Island, Virginia, without incident. Table II-2 shows a summary of the flight performance data.

Information was retrieved by means of a 243.1 MHz FM-FM telemetry system with 8 channels, two of which were used for engineering functions. In-flight calibration of all channels was provided every 50 seconds, starting at 10 sec. before lift-off.

The signal was recorded on magnetic tape after the first detection, together with a 100 kHz reference, 36-bit coded time and receiver AGC. Photographic paper records were made from these tapes for visual inspection. These showed that the instruments operated normally throughout the flight. No high voltage discharges were observed. The spectrometer channels showed a constant low reading, corresponding to an offset voltage, from lift-off to clamshell ejection. After that, the nitric oxide gamma bands were visible

TABLE II-1.

SPECTROMETER CHARACTERISTICS.

Rocket Number	14.389	14.390
Focal Length	250 mm	250 mm
Slit Width	.5 mm	.5 mm
Spectral Resolution at 2149 Å	5 Å	5 Å
Focal Ratio at 2149 Å	f/4	f/4
Scan Period (in each direction)	3 sec.	3 sec.
Calibration at 2149 Å	.227 kR/Å/V	.288 kR/Å/V

TABLE II-2.

FLIGHT PERFORMANCE DATA.

Rocket Number	14.389	14.390
Launch Date	31 Jan. 1969	6 Feb. 1969
Launch Time	19.10.00 U.T.	19.29.00 U.T.
Launch Site	Wallops Island, Va. (37.84°N, 75.48°W)	
Length of Flight (Telemetry)	361.6 sec.	360.5 sec.
Clamshell Ejection	60.0 sec.	60.2 sec.
Roll Rate	3.55 r.p.s.	3.35 r.p.s.
Coning Half-Angle	6°	10°
Apogee Height	115.40 km	114.01 km
Apogee Time	170.0 sec.	170.5 sec.
Apogee Horizontal Range	38.41 km	51.07 km
Flight Azimuth	92.47°	104.55°
Solar Zenith Angle at Apogee	63°	64°

in each spectrum accompanied, for low altitudes, by a Rayleigh scattering background (see Chapter III).

A total of 34 useful spectral scans were obtained for rocket 14.389, and 33 for rocket 14.390. The instruments went into saturation about 260 sec. after lift-off, when the reentering rockets tumbled and pointed at the bright horizon.

On-board gyroscopes provided a continuous monitoring of the rocket attitude. The upward looking instruments never deviated by more than 27° from the vertical.

The data from the experiments were originally in the form of an analog magnetic tape with the telemetry video signal, and a digital magnetic tape with the smoothed trajectory from radar tracking. Appendix B describes a series of computer programs used to bring the data into the form of:

1. Emission rate in kR/Å (Spectrometer);

2. Angular position of optical axis of instrument (Attitude);

3. Altitude and horizontal range (Trajectory).

In each of the three cases, the independent variable is a common time scale.

CHAPTER III

RAYLEIGH SCATTERING BACKGROUND

It was mentioned in Chapter II that the observed UV spectra contained a background emission besides the nitric oxide gamma bands; its intensity is about 0.3 kR/Å at 2130 Å for the first half of the second spectral scan of rocket 14.390 (see Fig. B-8). The corresponding height is 62 km.

The theoretical flux of Rayleigh scattered radiation under these conditions is of the order of:

$$\pi R = 10^{-9}\, \pi \mathcal{F}\, \sigma\, \eta \sec \chi \qquad \text{(III-1)}$$

where:

πR = specific flux of Rayleigh scattered radiation;

$\pi \mathcal{F}$ = solar flux, 4×10^{11} photons/cm^2/sec/Å (see Chapter VII);

σ = Rayleigh scattering cross-section, 2×10^{-25} cm^2 (from expression III-5);

η = vertical overhead air column density, 3×10^{21} cm^{-2}, above 62 km (see Chapter VII);

χ = angle between the vertical and the optical axis of the instrument, $\sim 20°$ (see Chapter II).

Substituting these values into (III-1), πR is found to be

0.26 kR/Å, in good agreement with the observed intensity, consider-

ing the approximations involved in the calculation.

Furthermore, an inspection of the background in Fig. B-8

shows a periodic component with a period of half that of the rocket

roll. This is consistent with the observation of Rayleigh scattering

with an instrument sensitive to polarization in a spinning rocket.

We therefore decided to interpret the observed background

in terms of Rayleigh scattering of solar radiation by air molecules;

the detailed treatment described in the rest of this chapter proved

this assumption to be correct.

The flux of Rayleigh scattered light is:

$$\pi R(\lambda) = 10^{-9} \, \eta \, \sec\chi \, P(\theta) \int_{\lambda-\Delta\lambda}^{\lambda+\Delta\lambda} \pi \mathcal{F}(\lambda') \, \sigma(\lambda') \, S(\lambda-\lambda') \, d\lambda' \qquad (III-2)$$

where:

λ = wavelength in Å;

$\pi R(\lambda)$ = specific Rayleigh scattered flux in kR/Å;

$\pi \mathcal{F}(\lambda)$ = specific incident solar flux in photons/cm^2/sec/Å;

$\sigma(\lambda)$ = Rayleigh scattering cross-section in cm^2;

$S(\lambda-\lambda')$ = normalized slit function of the instrument;

η = vertical column density of air above the instrument in cm^{-2};

χ = angle between the vertical and the optical axis of the instrument;

θ = angle between the radius vector to the sun and the optical axis of the instrument;

$P(\theta)$ = phase function for Rayleigh scattering;

$\Delta\lambda$ = wavelength difference between maximum of slit function and point where it becomes zero; equal to the resolution for our instruments.

The cross-section for Rayleigh scattering, excluding the phase function, is (Goody, 1964):

$$\sigma = \frac{32\pi^3 (n-1)^2}{3\lambda^4 N^2} \frac{(6 + 3\Delta)}{(6 - 7\Delta)} \qquad (III-3)$$

where:

n = refractive index of air;

N = number density of air molecules;

Δ = depolarization factor.

The refractive index of air, a function of wavelength, temperature and pressure, is found from Allen (1963) to be:

$$(n-1) = 8.92 \times 10^{-8} P \left\{ 1 + \frac{3.14\lambda^2}{\lambda^2 - 68.5} + \frac{9.68 \times 10^{-2}\lambda^2}{\lambda^2 - 244} \right\}$$

$$\left\{ \frac{1 + (1.05 + 1.57 \times 10^{-2} T)\ 10^{-6} P}{1 + 3.66 \times 10^{-3} T} \right\} \qquad (III-4)$$

15

where:

T   =   temperature in degrees Kelvin;

P   =   pressure in mmHg;

λ =   wavelength in $\overset{\circ}{A}$.

The depolarization factor, accounting for the asymmetry of the air molecules, has an average value of 0.035 for our atmosphere (see, e.g., Goody, 1964).

From expressions (III-3) and (III-4) and the perfect gas law, after neglecting a pressure dependent term unimportant for our altitudes (above 50 km), we find:

$$\sigma(\lambda) = 2.24 \times 10^{-13} \left\{ \frac{1}{\lambda^2} + \frac{3.14}{\lambda^2 - 6.85 \times 10^5} + \frac{0.0968}{\lambda^2 - 2.44 \times 10^6} \right\}^2$$

(III-5)

where:

σ =   Rayleigh scattering cross-section in cm^2;

λ =   wavelength in $\overset{\circ}{A}$.

The phase function (Goody, 1964) is:

$$P(\theta) = \frac{3}{2(2+\Delta)} \left\{ 1 + \Delta + (1 - \Delta) \cos^2\theta \right\}$$

(III-6)

Since the wavelength dependence of the cross-section is negligible in an interval of the order of the resolution of our instruments ($\sim 5\overset{\circ}{A}$), $\sigma(\lambda')$ can be taken outside the integral in Eqn. (III-2):

16

$$\pi R(\lambda) = 10^{-9} \eta \sec\chi \, P(\theta) \, \sigma(\lambda) \, \pi \mathcal{F}_s(\lambda) \qquad (III-7)$$

where $\pi \mathcal{F}_s(\lambda)$ is the result of the convolution of the solar flux with the normalized slit function:

$$\pi \mathcal{F}_s(\lambda) = \int_{\lambda-\Delta\lambda}^{\lambda+\Delta\lambda} \pi \mathcal{F}(\lambda') \, S(\lambda-\lambda') \, d\lambda' \qquad (III-8)$$

The evaluation of $\pi \mathcal{F}_s(\lambda)$ was carried out numerically: the solar flux in 0.2 Å intervals was taken from Brinkmann et al., (1966), and the theoretical triangular slit function was adopted with a half-width equal to the instrumental resolution (see Chapter II). The solar flux is shown in Fig. **E-1.** before and after convolution with the slit function.

The above expressions for the flux of Rayleigh scattered radiation (III-2 and III-7) assume single scattering in an optically thin atmosphere. This latter assumption is also important in the interpretation of the nitric oxide fluorescence scattering in Chapter IV. In order to verify it, the optical depth is computed for solar radiation in the 2025 to 2175 Å range for a height of 60 km and a solar zenith angle of 65°. The extinction processes considered are absorption by ozone, absorption by molecular oxygen, and Rayleigh scattering by air. The calculations are approximate and conservative, in the sense that the maximum cross-section is chosen within the wavelength interval of interest. Also, the calculations refer to extinction of solar

17

radiation before scattering. Extinction in the path between the scattering point and the instrument will always be even smaller for an upward looking instrument.

The optical depth for solar radiation is:

$$\tau = \sum_{i=1}^{3} \sigma_i \, \eta_i \, \sec \chi \qquad \text{(III-9)}$$

where:

χ = solar zenith angle;

σ_i = extinction cross-section, and

η_i = vertical column density of the ith constituent above the height being considered.

The cross-section for Rayleigh scattering in our wavelength interval is, from Eqn. (III-5), $5.0 \times 10^{-25} \, cm^2$. Absorption by ozone in the Hartley region takes place with a cross-section smaller than about $1.5 \times 10^{-18} \, cm^2$ (see, e.g., Craig, 1965). Molecular oxygen absorbs in the weak Herzberg continuum, where laboratory measurements are difficult to extrapolate to upper atmospheric pressures. We conclude, however, from the works of Ditchburn and Young (1962), and Blake et al., (1966), that the molecular oxygen absorption cross-section is smaller than $1.0 \times 10^{-23} \, cm^2$.

18

The column densities at 60 km can be taken from the rocket grenade experiments on the days of our flights to be 4.3×10^{21} cm^{-2} for air, and 9.0×10^{20} cm^{-2} for molecular oxygen; for ozone, we shall adopt 3.1×10^{16} cm^{-2} from the photochemical calculations of Park and London (1970) (see Appendix E). Actual measurements of ozone densities for twilight conditions indicate that the adopted value might be as much as a factor of 10 too high (Weeks and Smith, 1968).

The resulting optical depths are, at 60 km and for a solar zenith angle of 65°:

Ozone absorption	$\tau \leqq 0.1$
Molecular oxygen absorption	$\tau < 2 \times 10^{-2}$
Rayleigh scattering	$\tau \leqq 5 \times 10^{-3}$

It can be seen from these figures that the assumption of single scattering is perfectly justified, at least for Rayleigh scattering. That the same is true for the fluorescence scattering in the nitric oxide gamma bands is shown in Chapter IV.

The assumption of an optically thin atmosphere, however, does not hold too well at 60 km, due to ozone absorption. We shall return to this point in Chapter IV.

The Rayleigh scattering mechanism polarizes radiation. If the detecting instrument is sensitive to polarization, the resulting dependence of the received signal upon the geometry of the scattering can be taken into account by multiplying the right-hand side of

19

Eqns. (III-2) and (III-7) by f, a function of the relative positions of the sun and the instrument. Appendix C shows the derivation which results in:

$$f = 1 + p \frac{(1-\Delta) \sin^2\theta}{[1+\Delta + (1-\Delta) \cos^2\theta]} \cos 2(\gamma - \delta) \quad \text{(III-10)}$$

where p, a number in the interval $[0,1]$, is the degree of polarization of the instrument. If V_M is the response of the instrument to linearly polarized light in the plane of maximum acceptance, and V_m the response to the same signal in a plane $90°$ from the first, then $p = (V_M - V_m)/(V_M + V_m)$. γ is the angle between the plane defined by the sun and the optical axis of the instrument, and the vector perpendicular to the optical axis, transverse to the entrance slit. δ is the angle between this last vector and the plane of minimum acceptance of the instrument. These angles and vectors are shown in Fig. C-1.

Equation (III-7) can be re-written, after multiplication by f:

$$\pi R(\lambda) = 10^{-9} \eta \sec\chi \, P(\theta) \, \sigma(\lambda) \, \pi \mathcal{F}_s(\lambda) \left\{ 1 + p \frac{(1-\Delta) \sin^2\theta \cos 2(\gamma-\delta)}{1+\Delta + (1-\Delta) \cos^2\theta} \right\}$$

$$\text{(III-11)}$$

The polarization of the instruments was not determined before the flights in the laboratory. Since the payloads were not recovered,

we had to use a statistical approach and evaluate p from the Rayleigh

scattering contribution to the flight data.

Division of both sides of Eqn. (III-11) by $10^{-9} \sigma \pi \mathcal{F}_s$ brings

it to the form:

$$\frac{\pi R}{10^{-9} \sigma \pi \mathcal{F}_s} = \eta \sec \chi \, P(\theta) \left\{ 1 + p \, \frac{(1-\Delta) \sin^2 \theta \, \cos 2(\gamma - \delta)}{1 + \Delta + (1-\Delta) \cos^2 \theta} \right\} \qquad \text{(III-12)}$$

or

$$\frac{\pi R}{10^{-9} \sigma \pi \mathcal{F}_s} = A + B \cos(2\gamma) + C \sin(2\gamma) \qquad \text{(III-13)}$$

where A, B and C are functions of θ, χ, η only. Furthermore, these

variables can be considered constant within a time interval of the

order of 0.1 sec: θ and χ are related mainly to the coning of the

rocket, which has a period of 30 sec; changes in the atmospheric

density have a scale height of the order of 5 km which, coupled with

a maximum vertical velocity of 1 km/sec, result in a time scale of

5 sec for changes of η.

A two-factor regression analysis can then be performed on

each group of 100 data points (0.1 sec), excluding the regions with

nitric oxide emission bands. The quantity on the left of Eqn. (III-13)

is the dependent variable and $\cos(2\gamma)$ and $\sin(2\gamma)$ are the inde-

pendent variables. The resulting regression coefficients correspond

essentially to experimental determinations of "constants" A, B

and C. A comparison of Eqns. (III-12) and (III-13) allows us to

relate these values to the physically meaningful quantities:

$$\eta = \frac{A}{P(\theta) \sec\chi} \qquad (III-14)$$

$$p = \frac{\sqrt{B^2 + C^2}}{A} \frac{1 + \Delta + (1-\Delta) \cos^2\theta}{(1-\Delta) \sin^2\theta} \qquad (III-15)$$

$$\delta = \begin{cases} \frac{1}{2} \arcsin\left(\frac{C}{\sqrt{B^2 + C^2}}\right), & \text{if } B > 0 \\[2em] \frac{\pi}{2} - \frac{1}{2} \arcsin\left(\frac{C}{\sqrt{B^2 + C^2}}\right), & \text{if } B < 0 \end{cases} \qquad (III-16)$$

The angle δ was found to be $0°$, meaning that the plane of

maximum acceptance of the monochromators is parallel to the great-

er dimension of the entrance slit. The polarization p was found to

be between 15 and 25 percent. Its wavelength dependence was de-

termined later.

It was found that the column density could be represented by

an exponential function of height with the atmospheric scale height,

plus a constant contribution which we interpreted as being due to a

positive average value of the noise spikes present on the data.

Spectra obtained at altitudes above 100 km showed that this residual

background has no wavelength dependence. Its magnitude was found

to be:

22

4.2×10^{-3} kR/Å for rocket 14.389;

and

5.5×10^{-3} kR/Å for rocket 14.390;

these numbers should be compared, at 60 km, with a Rayleigh scattering contribution of 0.4 kR/Å and an average of 0.1 kR/Å for the (1,0) gamma band of nitric oxide. Since the noise spikes, and consequently the residual background, are also present inside the emission bands, we decided to subtract this contribution from all the data.

The determination of η was repeated after the subtraction of the residual background, and the results are shown in Figs. III-1 and III-2 plotted against flight time. Also presented in these figures are the adopted models of atmospheric column densities, a constant factor times the determinations by the rocket grenade technique (see Appendix E). The determination of these factors is described later in this Chapter.

The degree of polarization of the instruments, known from laboratory measurements on similar monochromators to be a function of wavelength, was determined to a better accuracy by the following method.
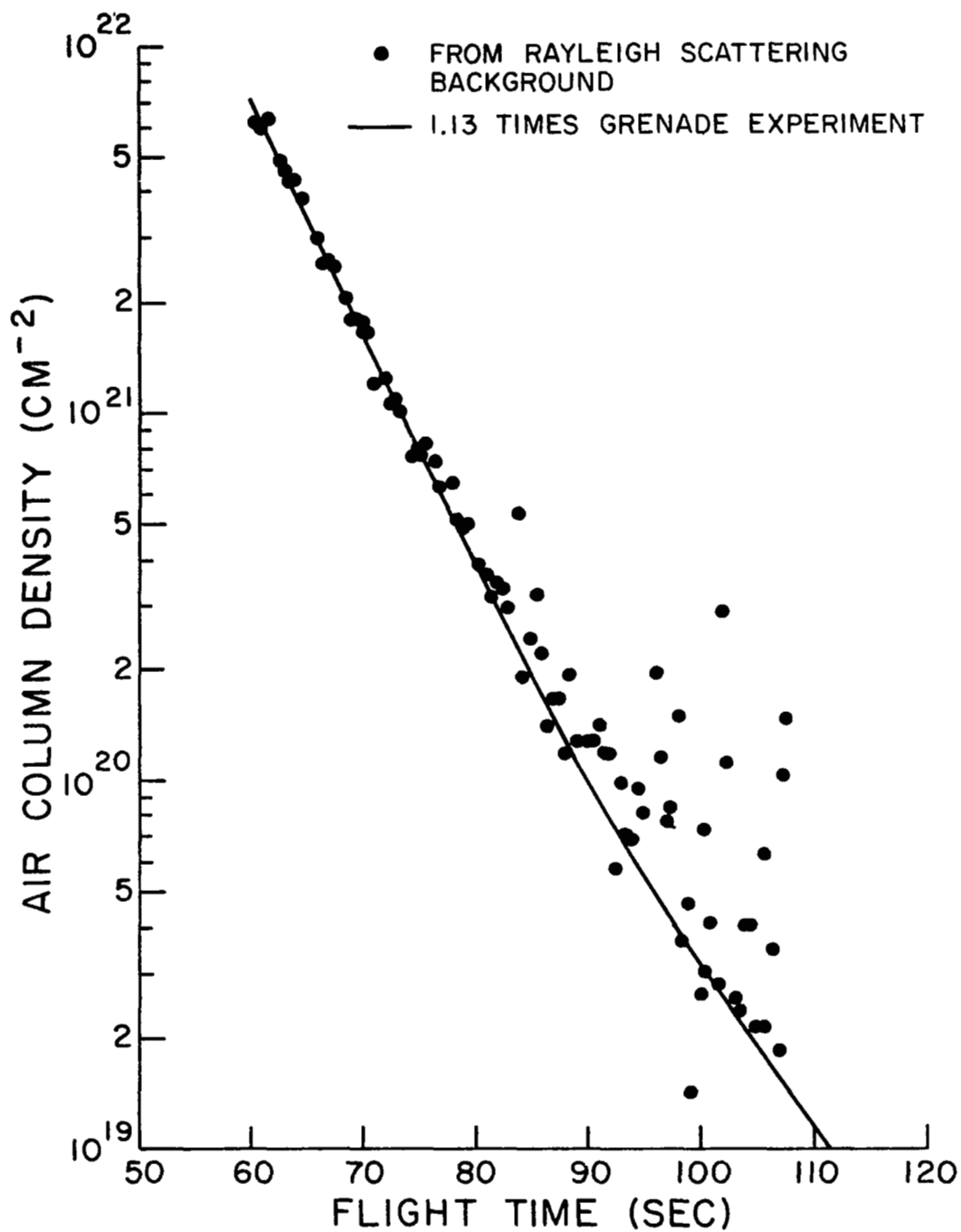
Figure III-1.   Experimental Air Column Density for Rocket 14.389.
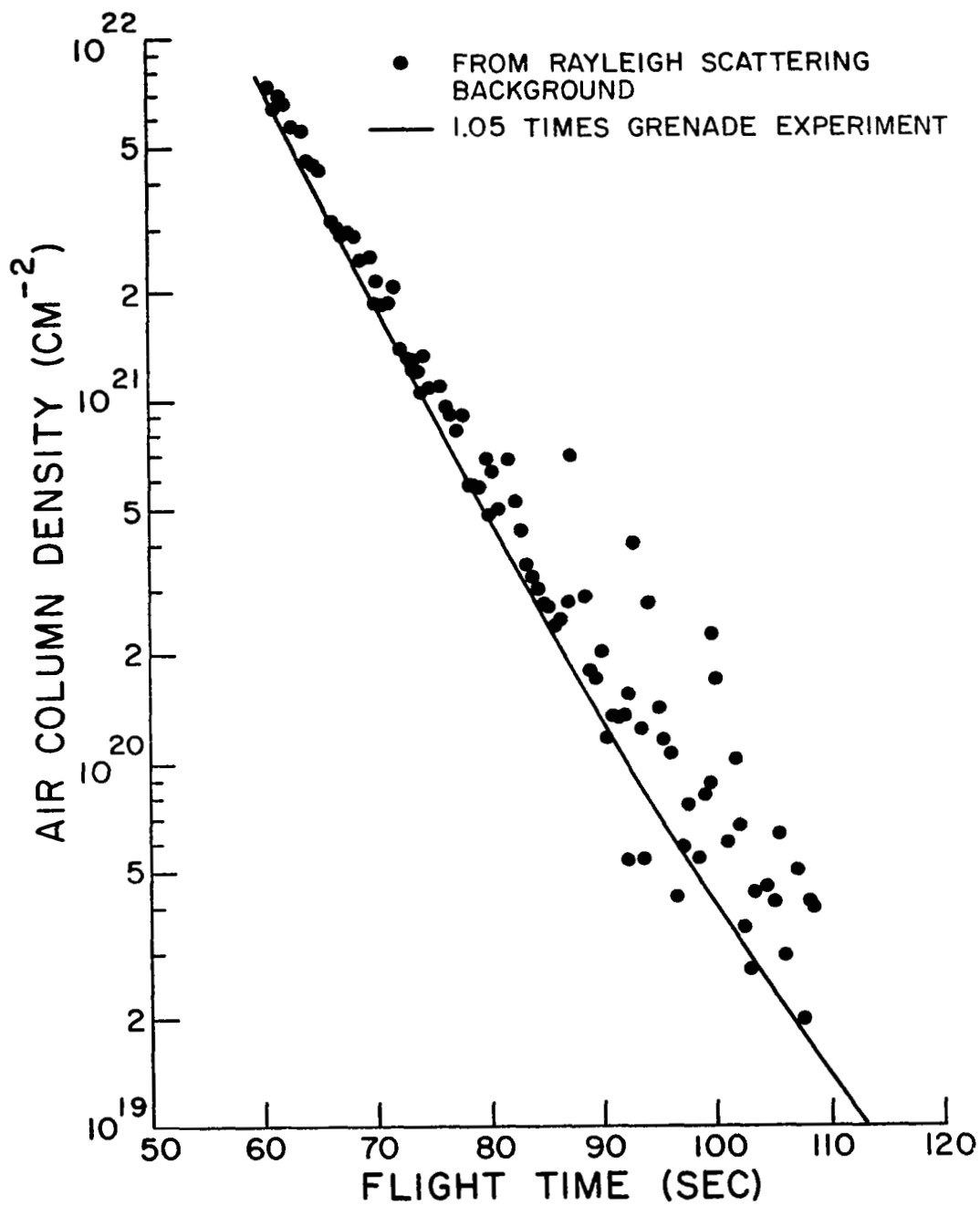
Figure III-2.   Experimental Air Column Density for Rocket 14.390.

Several values of p, in intervals of 5%, were used to calculate the theoretical Rayleigh scattering background (πR) with the help of Eqn. (III-11), using the known values of δ, and η from the grenade experiments (see Appendix E); the fine adjustment of the adopted column densities does not affect the determination of p. If p is taken too small, the data after background subtraction will be positively correlated with the roll modulation of the theoretical background; if p is taken too large, the correlation will be negative. We computed the above correlation as a function of p for several wavelength regions, using the data from the first spectral scan, where the roll modulation is most evident. The value of p for which the correlation becomes zero is taken as a polarization for that wavelength interval. Fig. III-3 shows the results, with the straight lines used to approximate the wavelength dependence of p.

It was mentioned earlier in this Chapter that the observed Rayleigh scattering background could be explained in terms of an atmospheric column density profile which was a factor (close to one) times the profile derived from the rocket grenade experiments. The final determination of this factor was accomplished by again calculating the theoretical Rayleigh background and subtracting it from the flight data, now using the polarization from Fig. III-3. The resulting data were then averaged in intervals equal to half the roll period, and the process repeated for several values of the multiplicative factor. The value was then chosen that brought the averaged

26
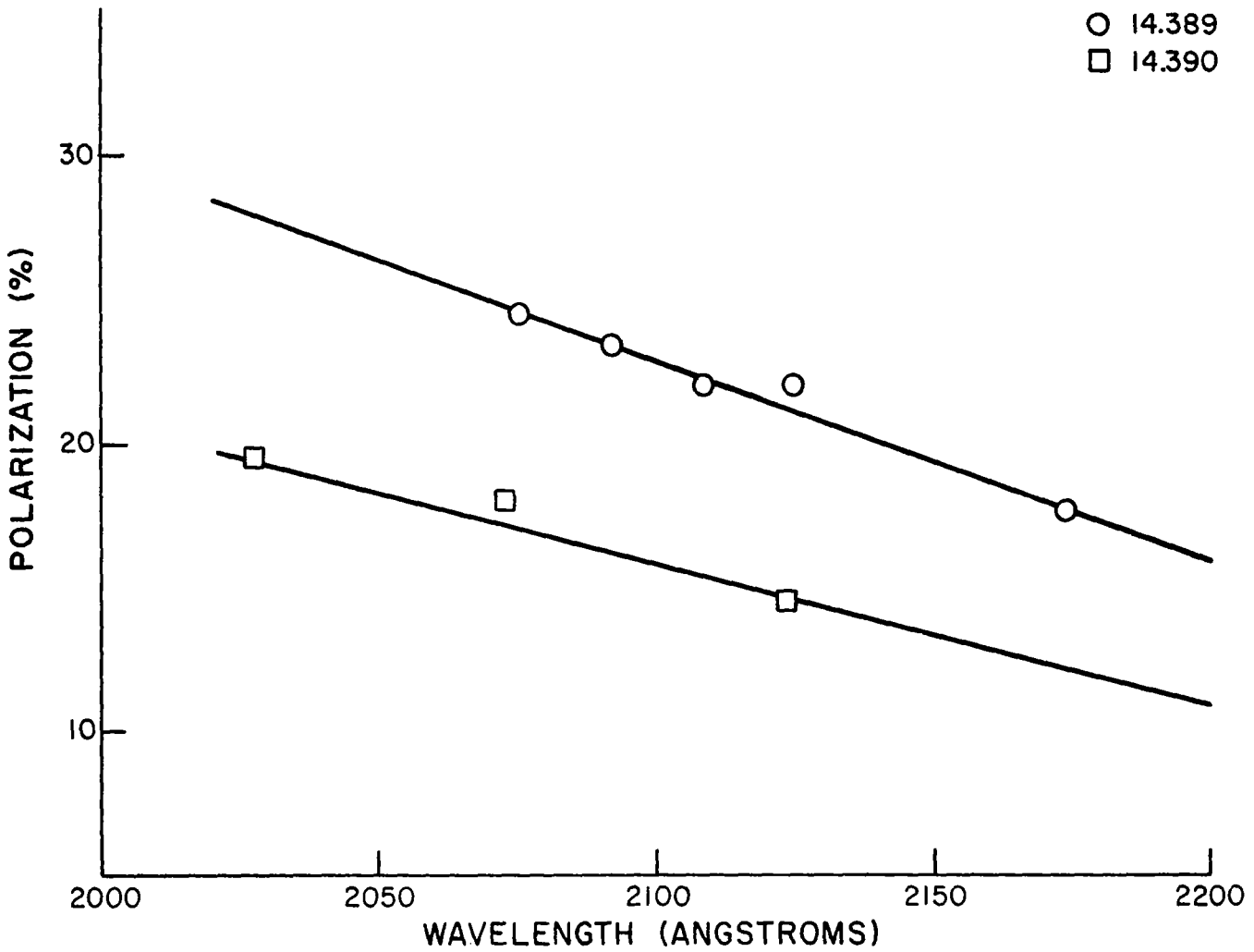
Figure III-3.   Experimental Determination of Monochromator
                 Polarization.

27

data closest to zero in the regions adjacent to the (1,0) gamma band, for the first full spectral scan after clamshell ejection:

$$\eta = 1.13 \times \eta_{grenade} \text{ for rocket 14.389,}$$

and

$$\eta = 1.05 \times \eta_{grenade} \text{ for rocket 14.390.}$$

Figs. III-4 and III-5 show examples of the averaged spectra used in this process.

With the experimentally derived values for p and δ, and the above expressions for the atmospheric column density, the theoretical Rayleigh scattering background was calculated (Eqn. III-11) and subtracted from the actual data point by point for both flights. Figs. III-6 through III-9 show the results of this procedure for the first full spectral scan of each rocket.

The subtraction of the Rayleigh scattering background is important only in the lower portion of our flights (below about 85 km). Therefore, the inaccuracy of the rocket grenade experiment in the upper end of its range is not expected to affect our results.

Finally, it must be mentioned that light scattering by dust particles was also considered as a potential source for the observed background emission, and its contribution judged to be negligible on the basis of evidence from noctilucent cloud studies (Witt, 1968)

28

NO GAMMA BANDS

(1,0)

(1,0)

(2,0)

1.05 TIMES GRENADE DENSITY

1.13 TIMES GRENADE DENSITY

INTENSITY (KR/A°)

.5

0

-.5

FLIGHT TIME (UNITS OF 1/2 ROLL PERIOD)

0   5   10   15   20   25   30   35   40
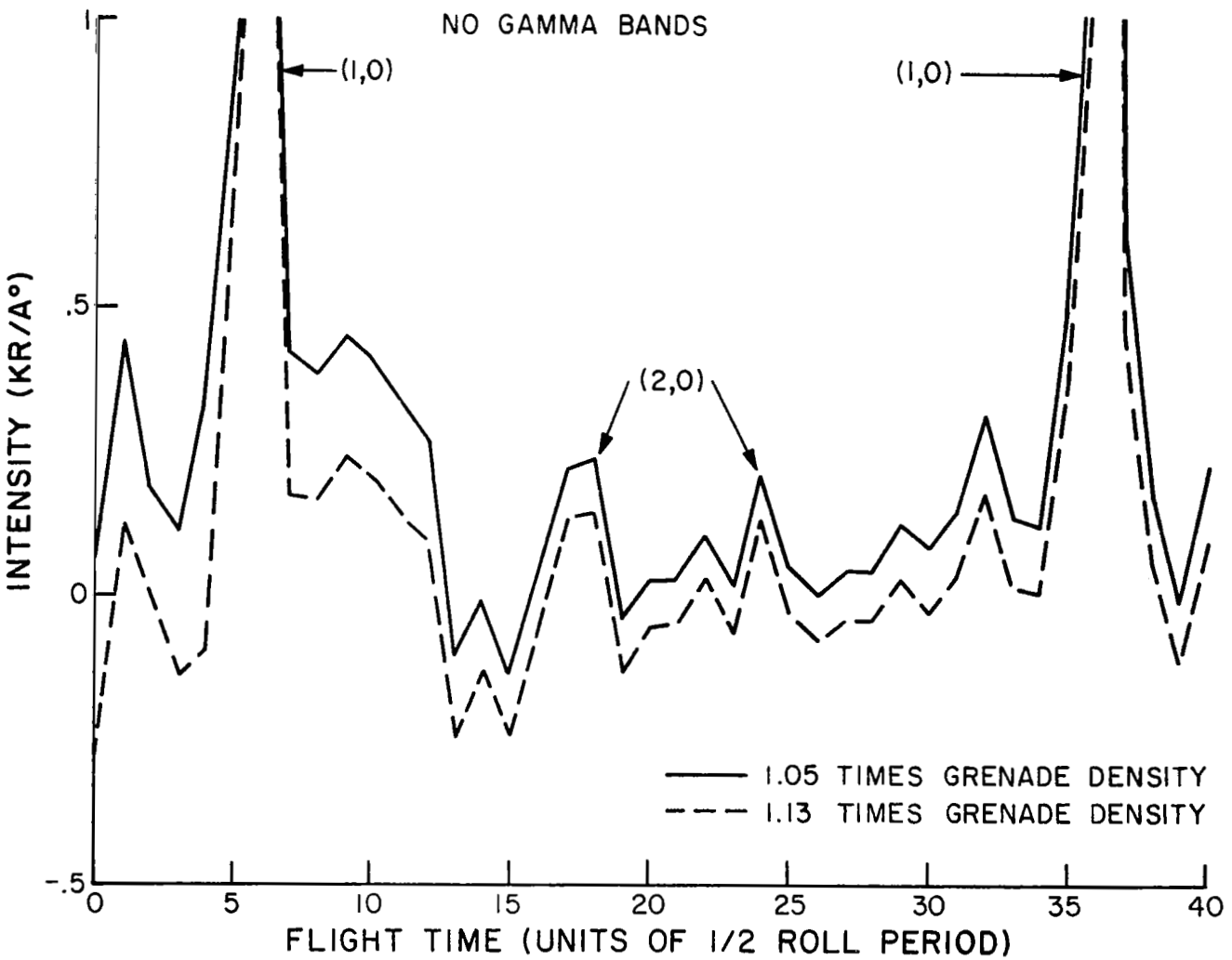
Figure III-4. Rocket 14.389; Rayleigh Background Subtraction for Different Column Density Profiles. First Full Scan After Clamshell Ejection.
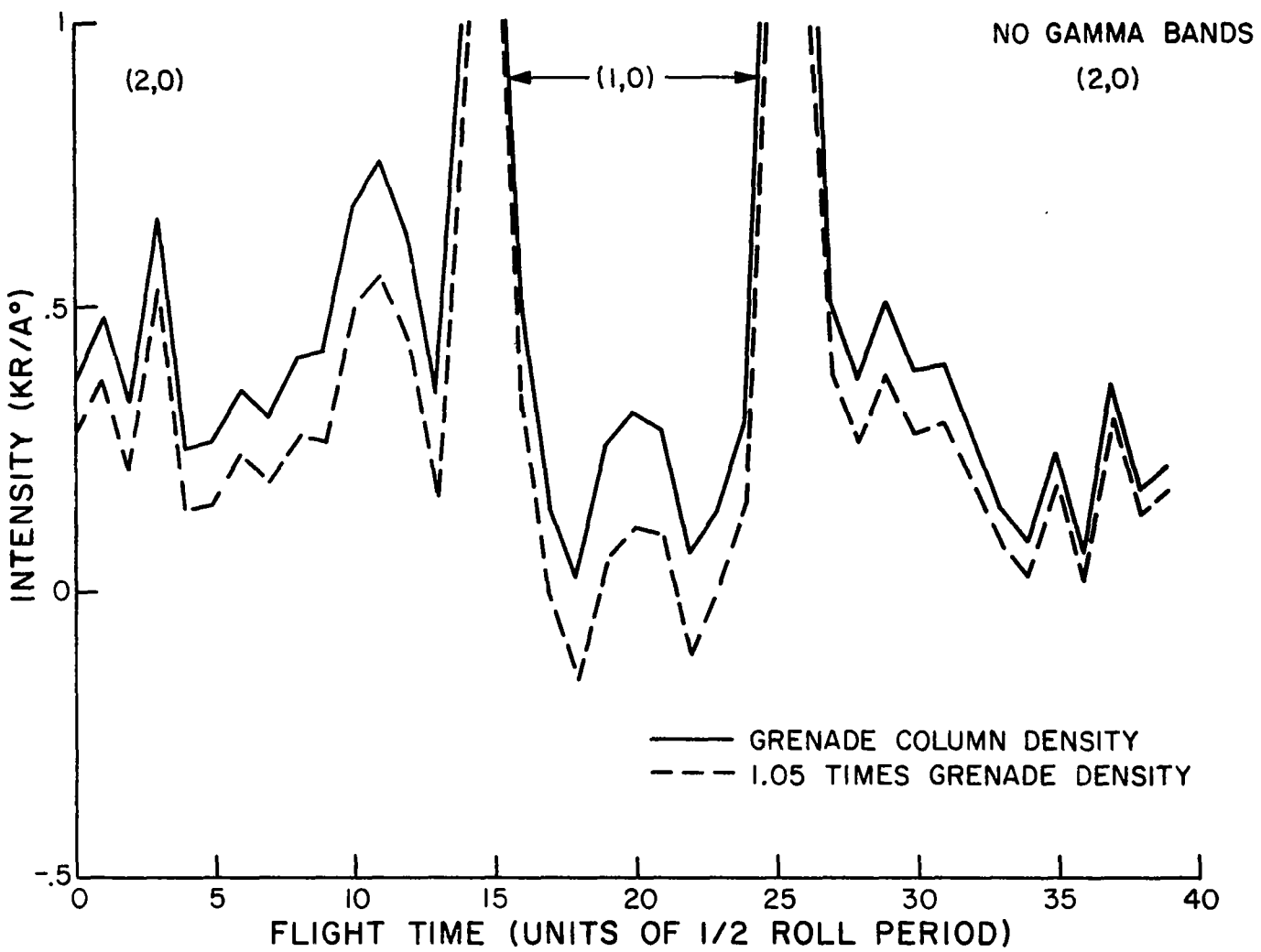
Figure III-5. Rocket 14.390: Rayleigh Background Subtraction for Different Column Density Profiles. First Full Scan After Clamshell Ejection.
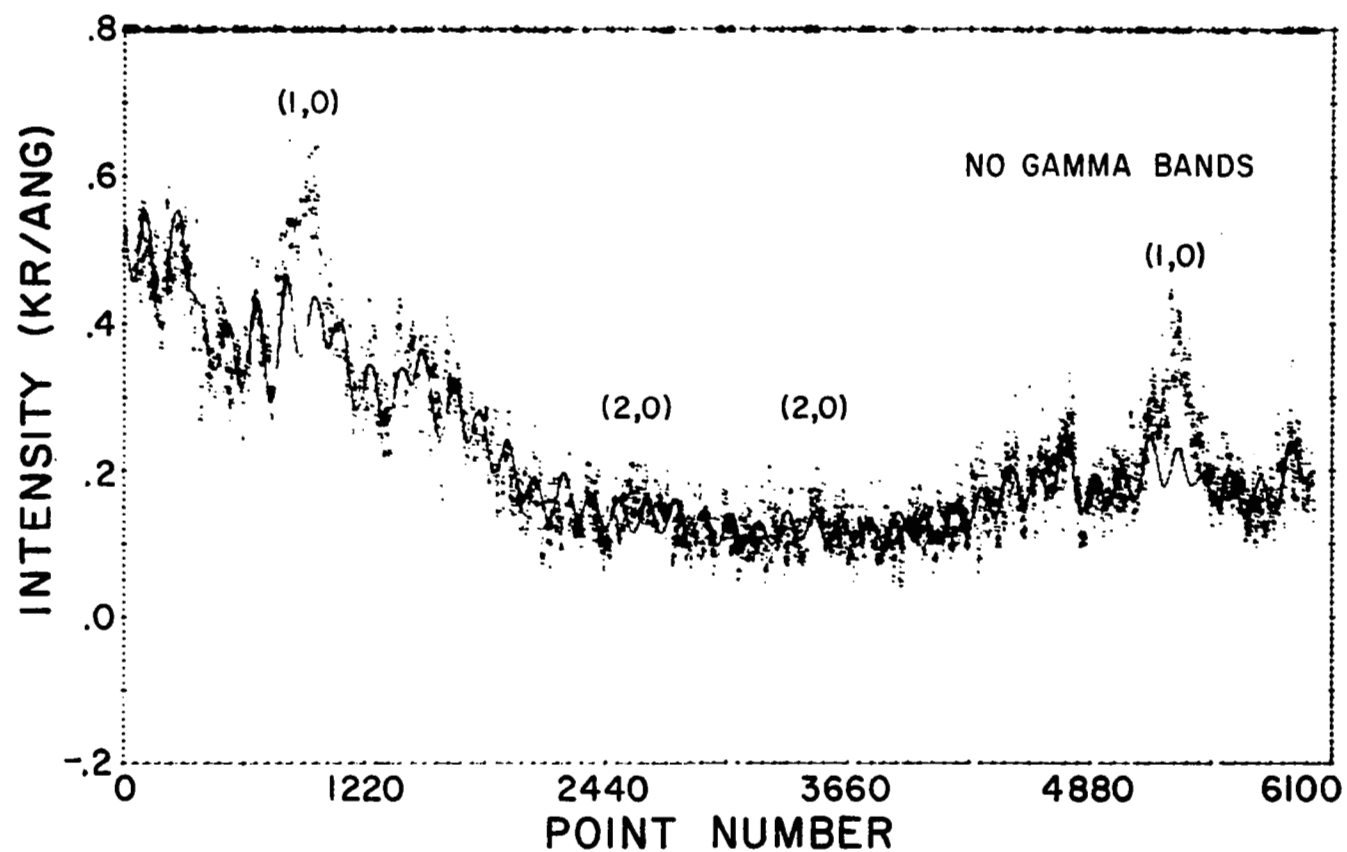
Figure III-6.   Rocket 14.389; Flight Data and Reconstructed Rayleigh
Scattering Background.
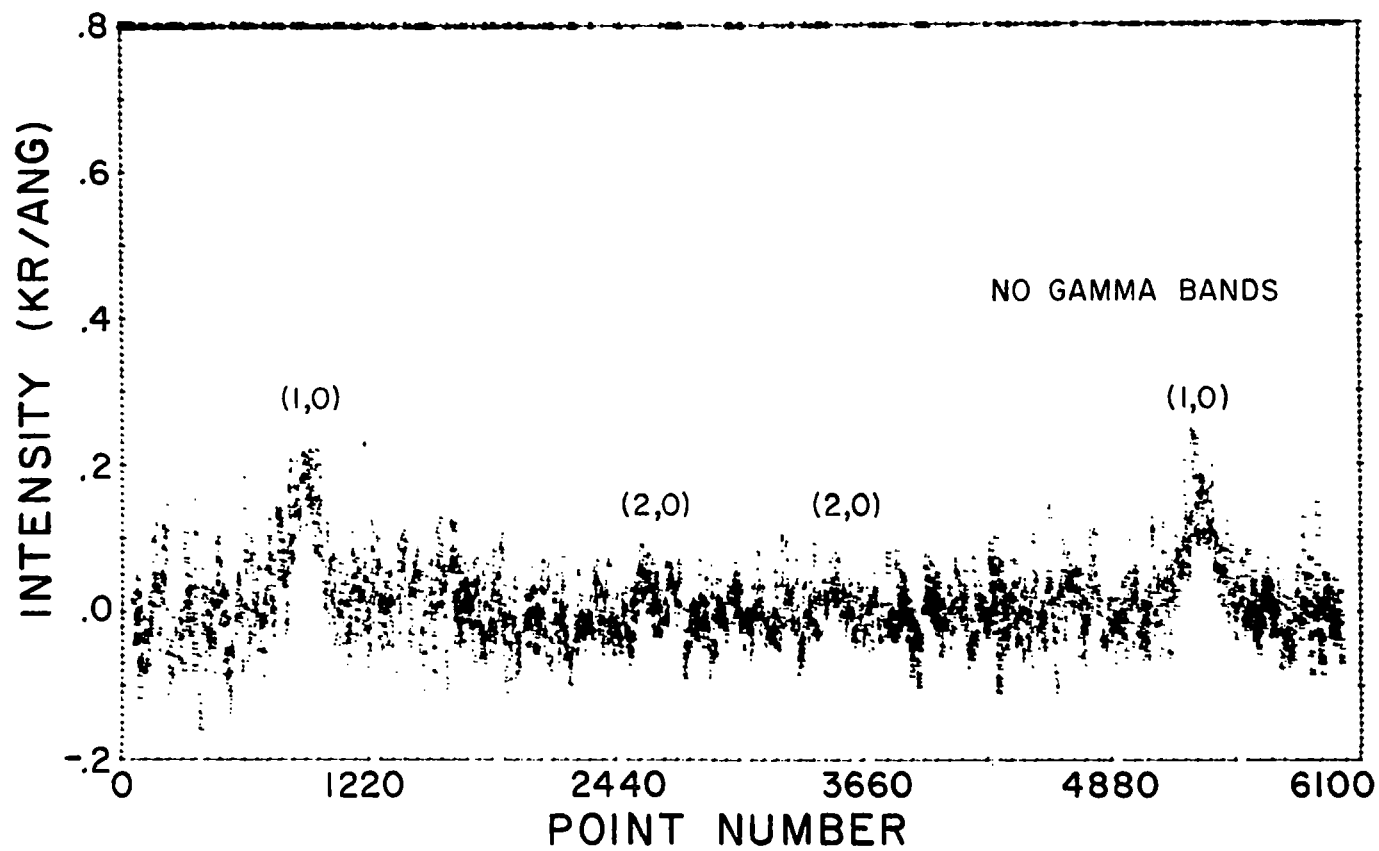
Figure III-7.   Rocket 14.389; Same Spectrum as in Preceding Figure, After Background Subtraction.
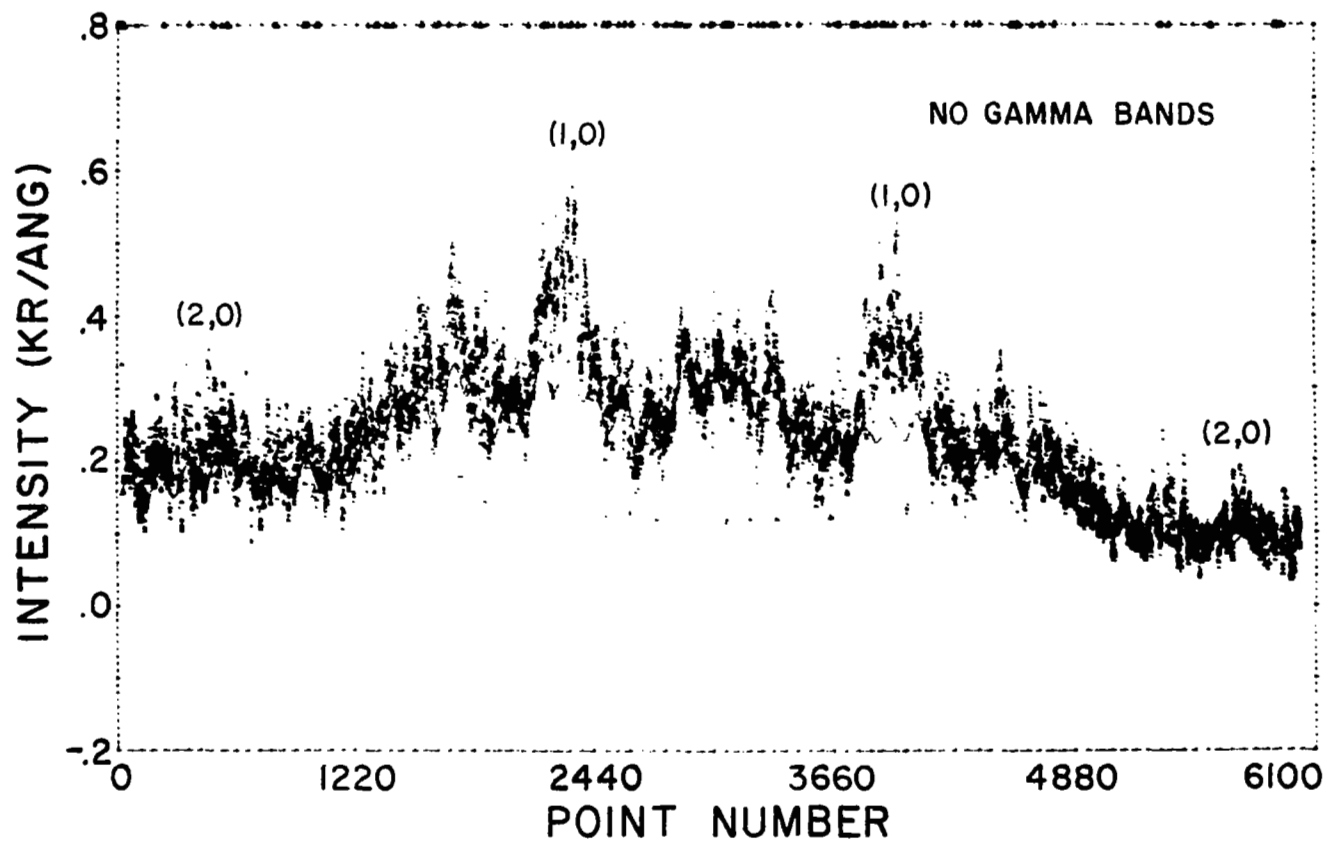
Figure III-8.   Rocket 14.390; Flight Data and Reconstructed Rayleigh
                 Scattering Background.
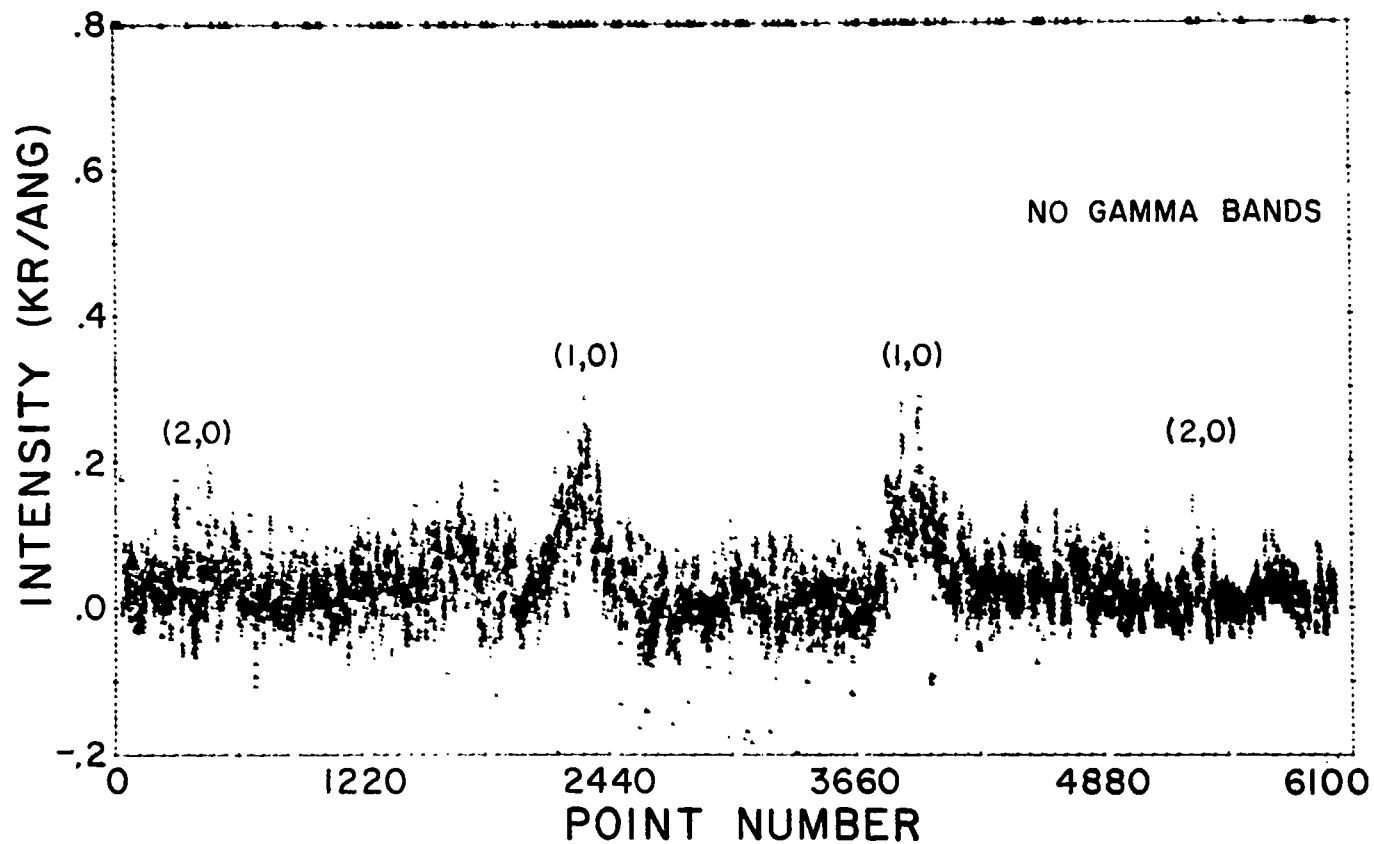
Figure III-9.   Rocket 14.390; Same Spectrum as in Preceding Figure,
After Background Subtraction.

CHAPTER IV

NITRIC OXIDE EMISSION

The nitric oxide gamma bands seen in the dayglow are due
to resonance fluorescence (Barth, 1964): ground state molecules
$(X^2\Pi)$ are excited by sunlight into the $(A^2\Sigma^+)$ state from where they return
with the spontaneous emission of photons. The apparent emission
rate is, for an instrument looking upward and an optically thin at-
mosphere:

$$4\pi\mathfrak{I} = 10^{-9} \eta \, g \, \sec\chi \qquad\qquad \text{(IV-1)}$$

where:

g   =   emission rate factor (photons/sec);

η =   vertical column density of the fluorescing substance
(cm^{-2});

χ =   angle between the vertical and the optical axis of the
instrument.

The emission rate factors have been calculated by Barth (1964)
and more recently revised by Pearce (1969c) for the (1,0) and (2,0)
gamma bands of nitric oxide. Pearce also showed that the tempera-
ture effect on the intensity of the bands is insignificant and quench-
ing negligible above 35 km. The factors applicable to this work are:

35

$$g_{1,0} = 3.93 \times 10^{-6} \text{ photons/sec;}$$

$$g_{2,0} = 9.62 \times 10^{-7} \text{ photons/sec.}$$

Our instruments were not able to resolve the rotational structure of the bands. However, an average was found of all spectra, after background subtraction (Fig. IV-1) which shows a degradation to the violet, as expected (see, e.g., Pearce, 1969c).

The emission rates in the (1,0) and (2,0) gamma bands of nitric oxide were found as a function of altitude from our experimental data, after the subtraction of the Rayleigh scattering background (see Chapter III), by integrating under the bands in each spectral scan, with the limits:

2134 to 2160 Å for the (1,0) band,

and

2034 to 2056 Å for the (2,0) band.

Before the integration, the data were interpolated to fill in the gaps left by the removal of the noise spikes (see Appendix B).

The resulting emission rate profiles for the (1,0) band are shown in Figs. IV-2 and IV-3, after correction to zenith intensity.
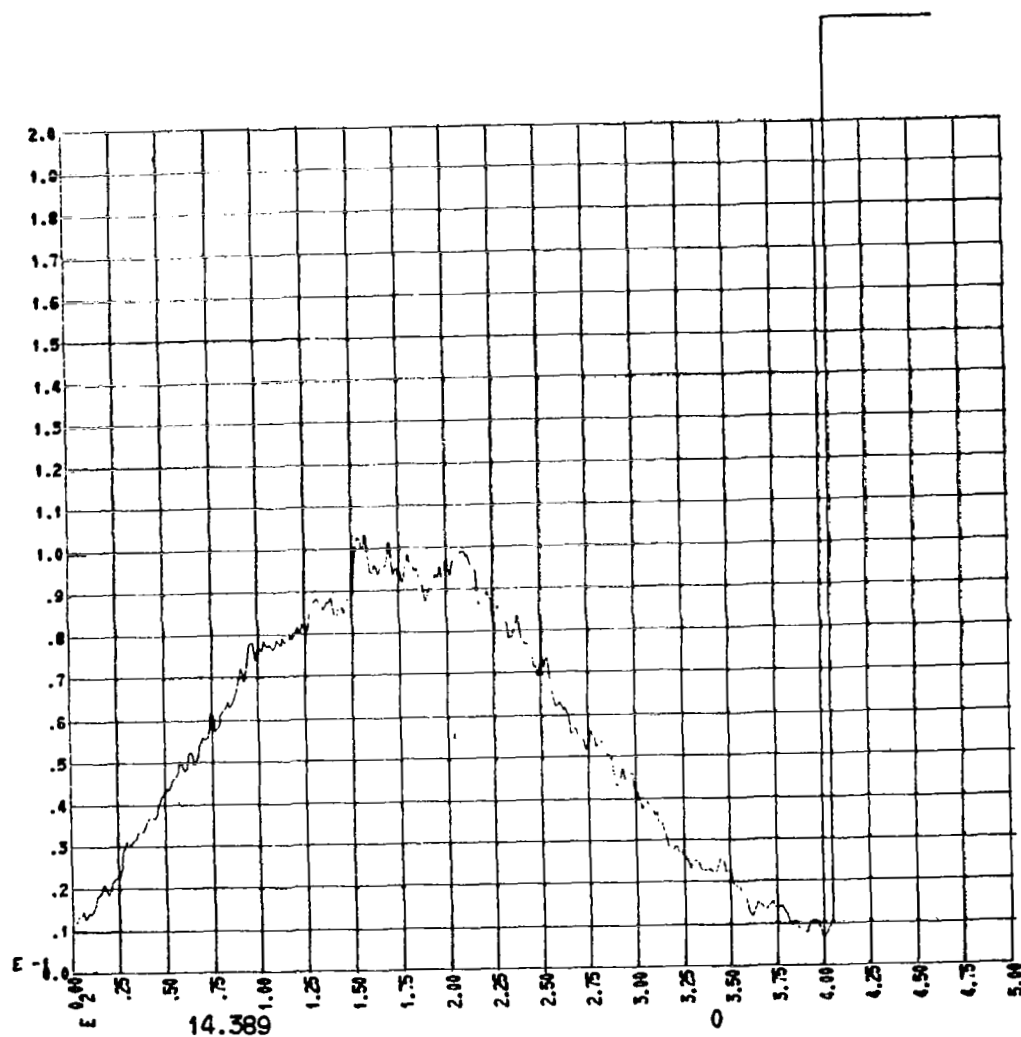
Figure IV-1. Average of all (1,0) Bands for Flight 14.389. Horizontal Scale is Arbitrary, Wavelength Increases to the Left.
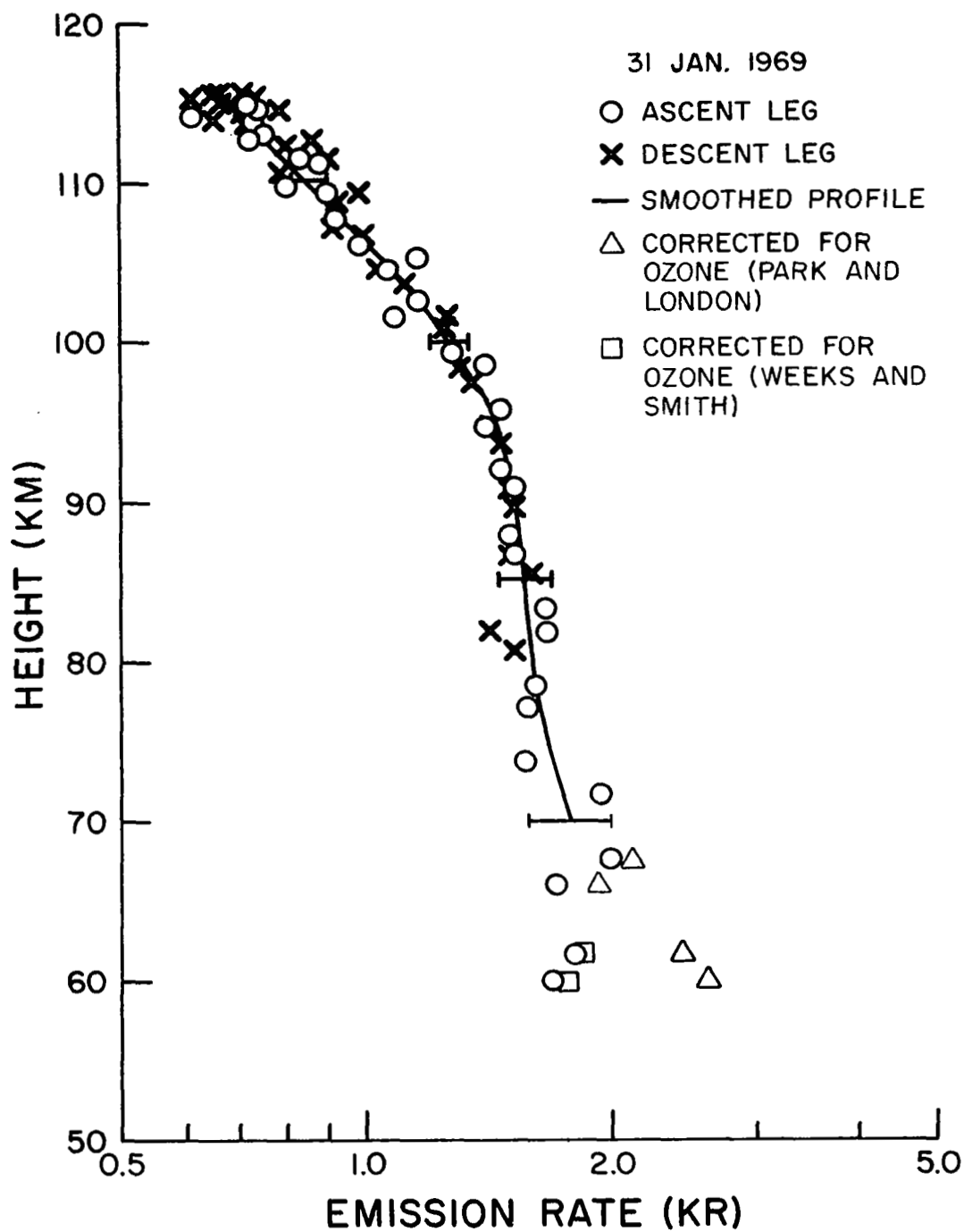
Figure IV-2. Emission Rate Profile for Rocket 14.389;
(1,0) Gamma Band of NO.
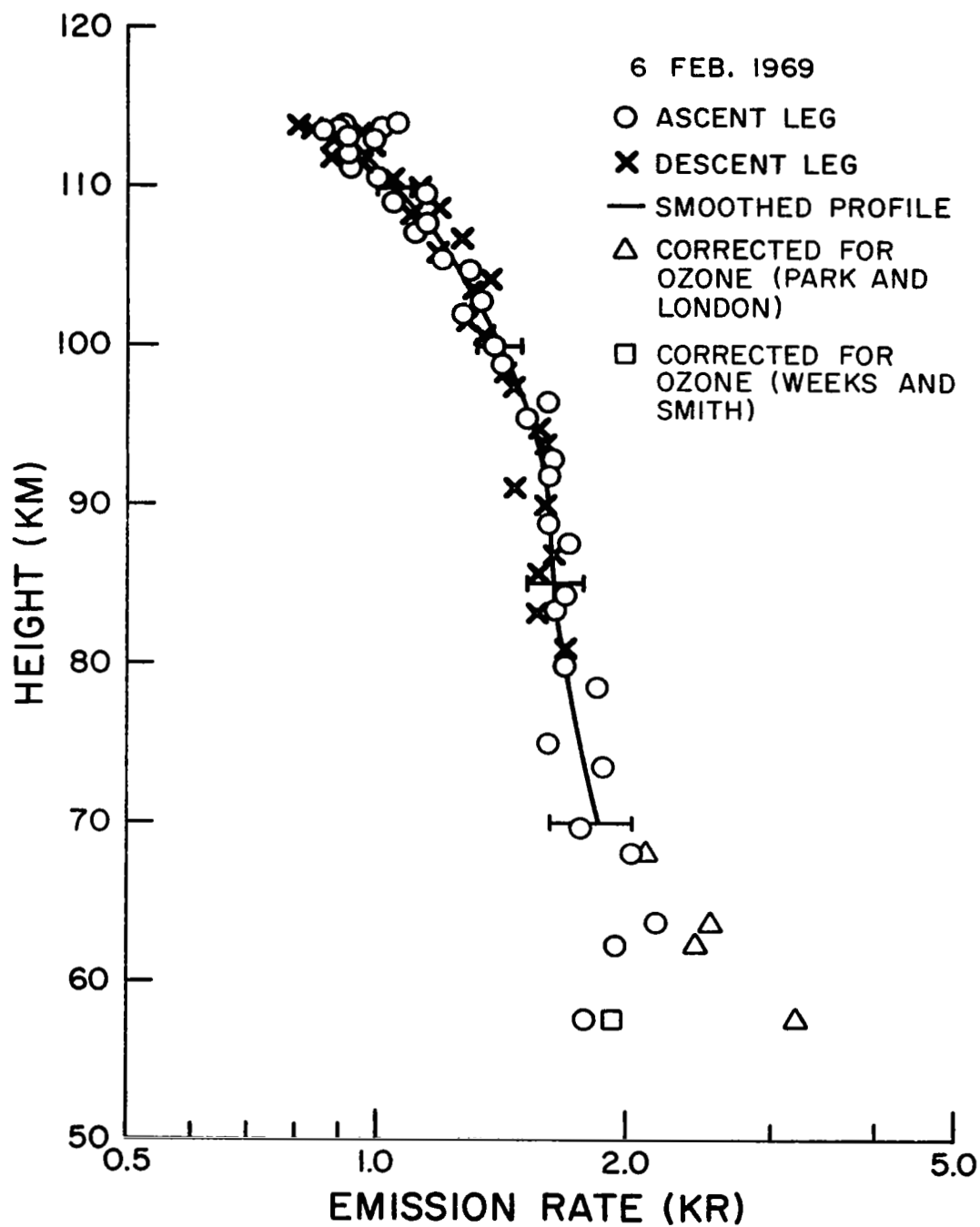
Figure IV-3. Emission Rate Profile for Rocket 14.390; (1,0) Gamma Band of NO.

It was concluded in Chapter III that although the atmosphere is relatively thin in the wavelength range of our instruments, absorption by ozone might be noticeable at the lowest altitudes (around 60 km). Since no attenuation of the solar flux was considered in computing the Rayleigh scattering background to be subtracted from the flight data, the presence of ozone absorption will result in an underestimation of the nitric oxide emission rate not only by the factor $e^{-\tau O_3}$, but mainly by causing an overestimation of the Rayleigh background. This effect can be easily understood in the treatment we will now adopt for the ozone absorption problem.

We shall neglect extinction by molecular oxygen absorption and Rayleigh scattering, in favor of ozone absorption (see Chapter III). Also, we consider only the extinction of the radiation between the sun and the scattering region, and not in the path from the scatterer to the instrument.

Let us define the emission rates of nitric oxide in the $(1,0)$ gamma band:

$4\pi\mathfrak{I}_C$ = correct emission rate taking into account ozone absorption and the Rayleigh scattering background;

$4\pi\mathfrak{I}_R$ = emission rate derived by taking into account the Rayleigh background but assuming no ozone absorption;

$4\pi\mathfrak{I}_N$ = emission rate derived by neglecting completely both the Rayleigh background and ozone absorption.

40

Let us define the nondimensional ratio r such that

$$\vartheta_R = \vartheta_N/r \qquad\qquad (\text{IV-2})$$

In other words the effect of the Rayleigh scattering background can be taken into account by dividing the raw emission rates by r. The value of r is 1 at high altitudes and increases to about 7 at 60 km. The important point is that we have experimental values for r, corresponding to each data point in the emission profile (two for each spectral scan). The values were obtained by actually computing $4\pi\vartheta_N$ and $4\pi\vartheta_R$ independently and finding their ratio.

Considering that ozone absorption decreases the solar flux available for both Rayleigh and fluorescence scattering, it can be shown that the quantities defined above are related by

$$4\pi\vartheta_C = 4\pi\vartheta_R [1 + r(e^\tau - 1] \qquad\qquad (\text{IV-3})$$

where τ is the optical depth for ozone absoprtion:

$$\tau = \sigma_{O_3}\, \eta_{O_3}\, \sec\chi \qquad\qquad (\text{IV-4})$$

where:

σ_{O_3} = ozone absorption cross-section, 1.2×10^{-18} cm^2 at 2149 Å (see, e.g., Craig, 1965);

χ = solar zenith angle, 63° and 64° for rockets 14.389 and 14.390 respectively;

η_{O_3} = vertical overhead column density of ozone, in cm^{-2}.

Ozone concentrations are poorly known in the mesosphere; observations by spectroscopic methods are difficult to perform due to the low densities; photochemical calculations on the other hand

can be helpful, since photochemical equilibrium is thought to pre-

vail for ozone in the height range of interest.

We decided to adopt as examples two ozone profiles: the

theoretical model of Park and London (1970) and the experimental

determination of Weeks and Smith (1968). Equations (IV-3) and

(IV-4) were then used to obtain the 'correct' emission rate $4\pi\vartheta_c$.

The calculations are presented in Tables IV-1 and IV-2, and the

resulting emission rates are indicated in Figs. IV-2 and IV-3.

It can be seen from these results that even small optical

depths of ozone can cause appreciable differences in the derived

emission rate of nitric oxide, because of the large factor r in Eqn.

(IV-3); also, significant differences are seen to arise from the choice

of one or another ozone profile. Rocket measurements of ozone on

both days of our flights (Krueger, 1969) at altitudes of up to 48 km

seem to suggest by extrapolation that the actual ozone concentrations

are somewhere in the middle between the two profiles used in the

caculations.

The solid lines in Figs. IV-2 and IV-3 represent the smoothed

emission profiles actually used for differentiation. They were drawn

by hand, and in doing so we smoothed out features of a size smaller

than the atmospheric scale height (about 6 km in that region). The

relative error bars drawn reflect instrumental noise above 85 km;

below that level, the Rayleigh scattering background complicates

42

TABLE IV-1

CORRECTION OF THE NITRIC OXIDE EMISSION RATE PROFILE FOR
OZONE ABSORPTION, ROCKET 14.389

Height	r	$4\pi \vartheta_R$ (kR)	Park and London		Weeks and Smith	
			τ	$4\pi \vartheta_C$ (kR)	τ	$4\pi \vartheta_C$ (kR)
60.0	7.35	1.68×10^{-1}	.071	2.60×10^{-1}	.0061	1.76×10^{-1}
61.7	5.83	1.80×10^{-1}	.058	2.43×10^{-1}	.0045	1.85×10^{-1}
66.0	3.59	1.71×10^{-1}	.032	1.92×10^{-1}	.0018	1.72×10^{-1}
67.6	2.74	1.97×10^{-1}	.025	2.11×10^{-1}	.0012	1.98×10^{-1}
71.7	1.90	1.94×10^{-1}	.012	1.98×10^{-1}	.00045	1.94×10^{-1}
73.2	1.86	1.56×10^{-1}	.0048	1.58×10^{-1}	.00015	1.56×10^{-1}

TABLE IV-2

CORRECTION OF THE NITRIC OXIDE EMISSION RATE PROFILE FOR OZONE ABSORPTION, ROCKET 14.390

Height (km)	r	$4\pi \mathcal{I}_R$ (kR)	Park and London		Weeks and Smith	
			τ	$4\pi \mathcal{I}_C$ (kR)	τ	$4\pi \mathcal{I}_C$ (kR)
57.8	8.16	1.80×10^{-1}	.093	3.24×10^{-1}	.0090	1.93×10^{-1}
62.2	4.53	1.96×10^{-1}	.055	2.46×10^{-1}	.0041	1.99×10^{-1}
63.8	3.46	2.19×10^{-1}	.047	2.56×10^{-1}	.0030	2.21×10^{-1}
68.0	2.45	2.00×10^{-1}	.025	2.12×10^{-1}	.0012	2.00×10^{-1}
69.6	2.34	1.77×10^{-1}	.019	1.85×10^{-1}	.00079	1.77×10^{-1}
73.4	1.63	1.88×10^{-1}	.0047	1.89×10^{-1}	.00015	1.88×10^{-1}

matters as there is an additional uncertainty associated with the atmospheric column density. The error bars drawn assume a 5% accuracy in the background amplitude, which seems reasonable in view of the results in Figures III-4 and III-5. Finally, the lowermost points in the emission rate profile are also uncertain because of ozone absorption. We feel that the uncertainty associated with the points below 70 km is so large that no attempt was made to derive local emission rates and nitric oxide densities in that region.

The apparent emission rates were also found for the (2,0) band (Fig. IV-4). These data were used only for verification, due to their lower signal to noise ratio.

Equation (IV-1) was then used to find the vertical column density of nitric oxide from the (1,0) band emission rate profile (solid line in Figs. IV-2 and IV-3); numerical differentiation every 2.5 km led to the local densities presented in Figs. IV-5 and IV-6.

The error bars shown in these figures reflect the relative accuracy of the emission rate profiles. The height corresponding to each data point was considered to be known with a negligible error. As for absolute errors, which would appear as a displacement of the whole density profile, we can point to the fact that the atmospheric density data used for the Rayleigh scattering background were multiplied by the factors 1.13 and 1.05 for flights 14.389 and 14.390 respectively. These factors actually provide us with an in
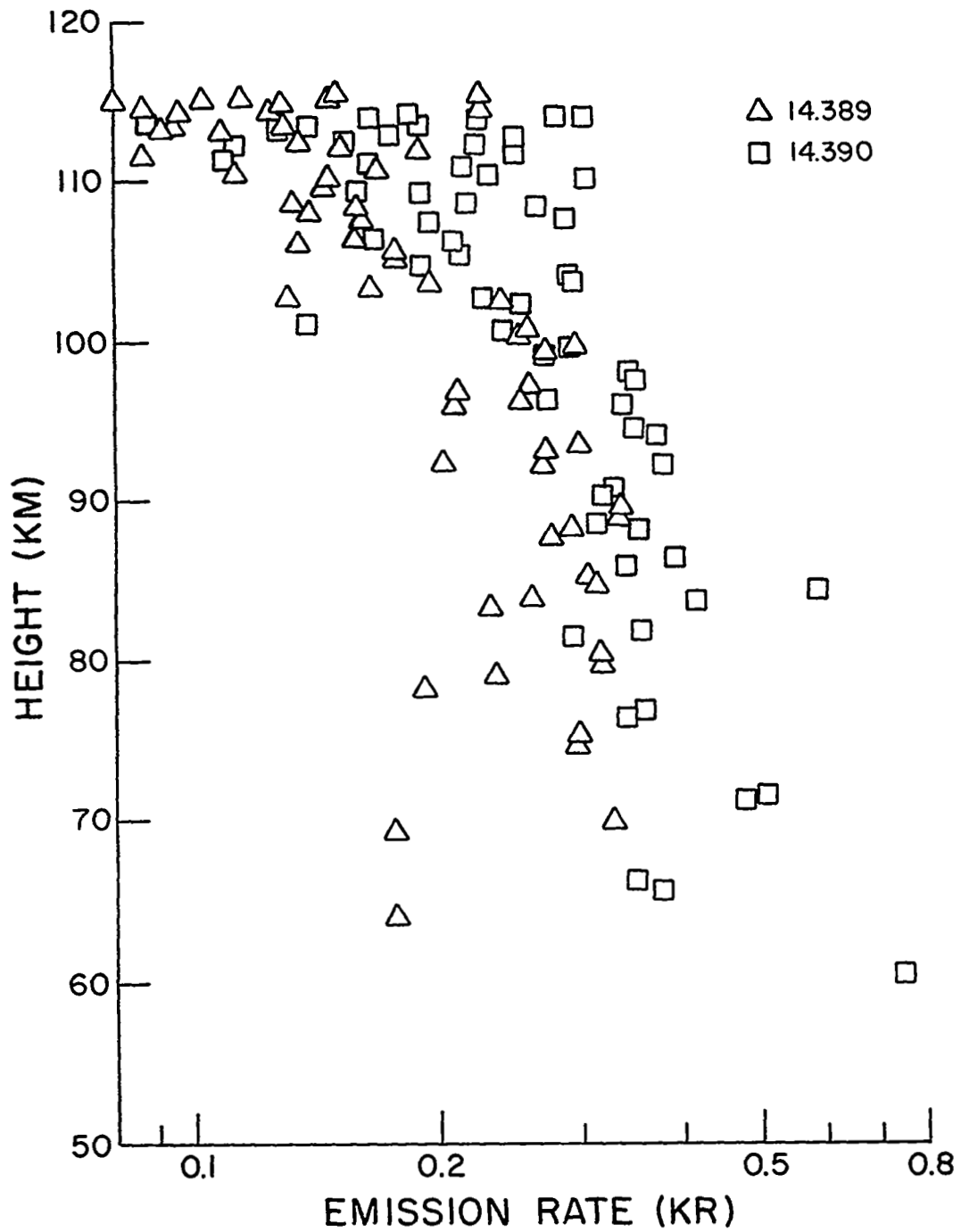
Figure IV-4. Emission rate of (2,0) Gamma Band for Both
Flights. Ascent and Descent Leg Data Are
Included, With No Distinction.
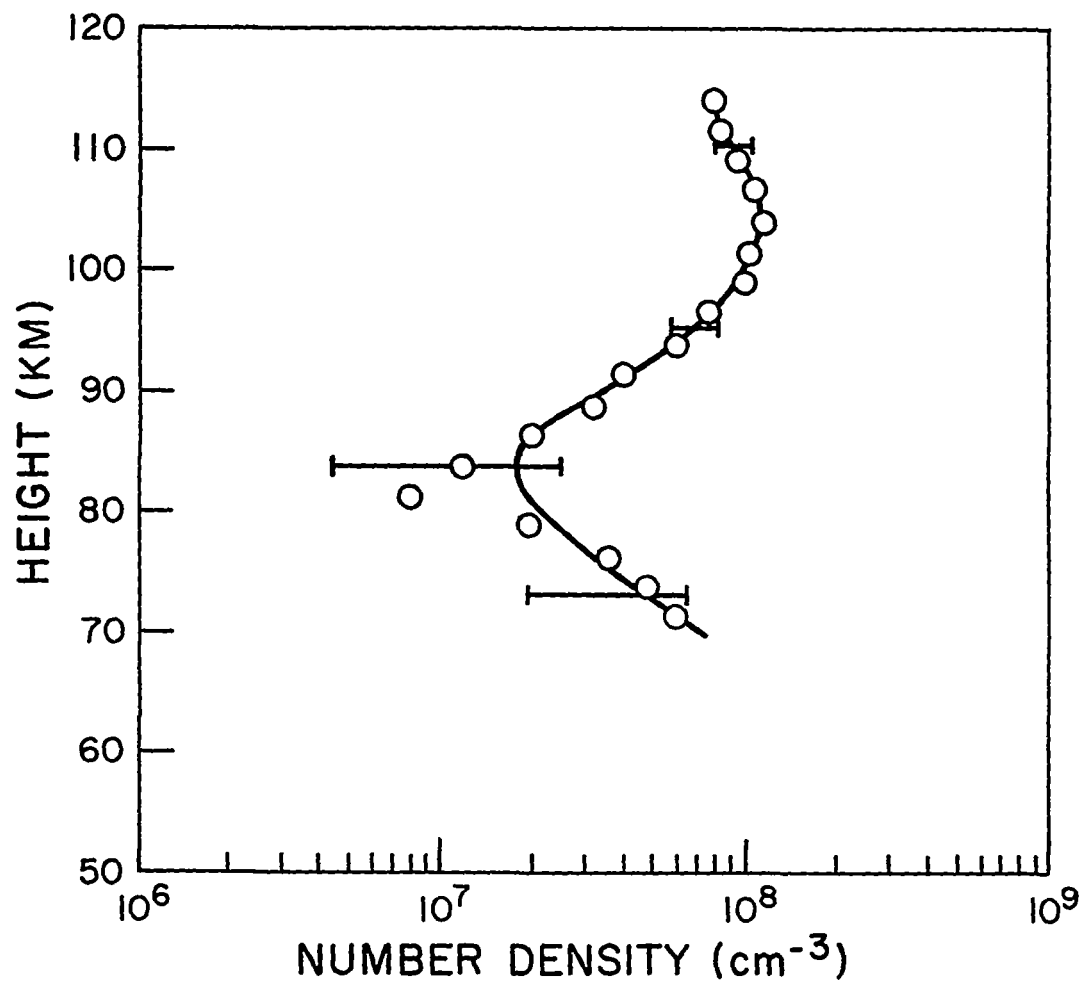
Figure IV-5.   Experimental Nitric Oxide Density Profile for
Rocket 14.389; 31 January 1969.
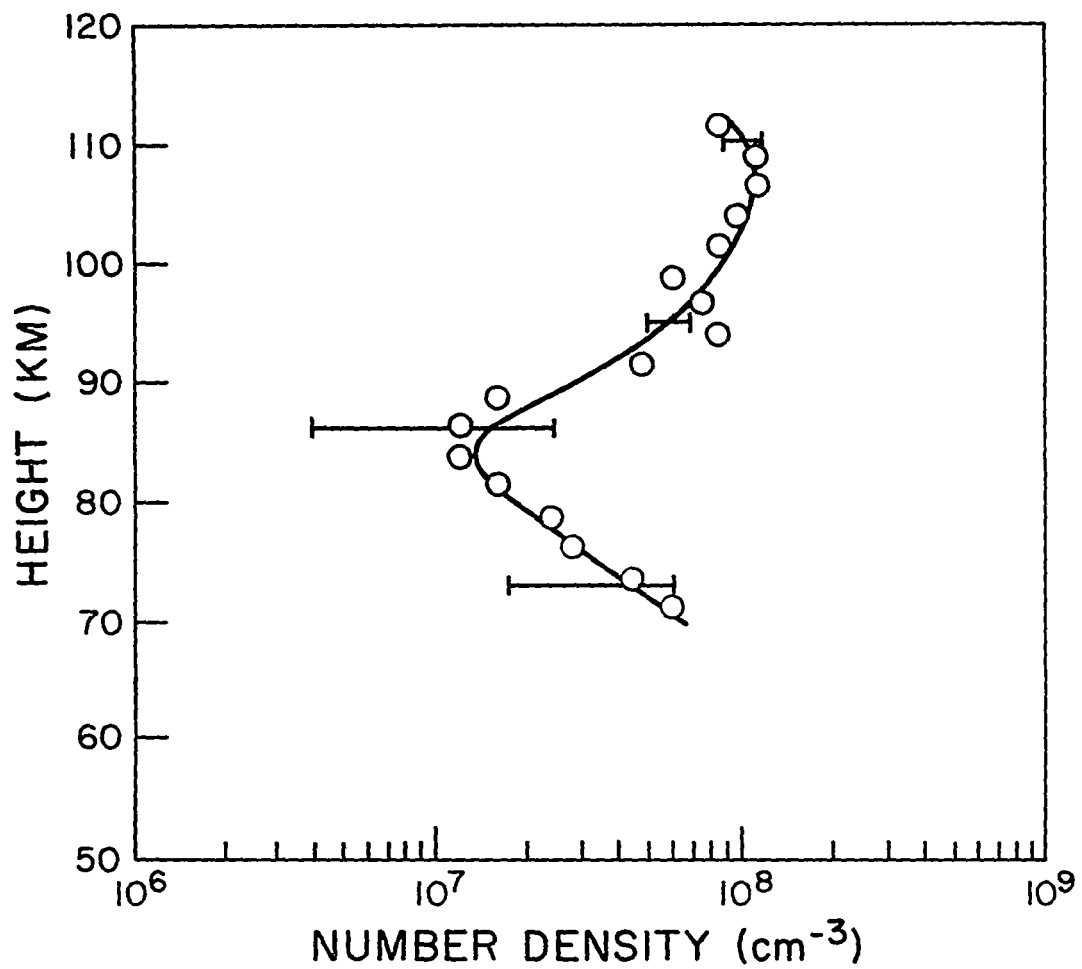
Figure IV-6.   Experimental Nitric Oxide Density Profile for
Rocket 14.390; 6 February 1969.

48

situ calibration of the instruments in terms of the air density. Therefore, we can say that the mixing ratio of nitric oxide is known better than its absolute density. The results in terms of mixing ratios are presented in Fig. IV-7, where the total atmospheric density was taken from the rocket grenade experiments (Appendix E).

It was shown in Chapter III that the assumption of single scattering is valid for Rayleigh scattering. For the fluorescence scattering in the nitric oxide gamma bands, we shall invert the procedure and compute the vertical column density of NO necessary to make the optical depth equal to 1, for a 65° solar zenith angle.

The absorption cross-section of nitric oxide in the gamma bands can be found from

$$\sigma_{0,v'} = \frac{\pi e^2}{mc^2} \frac{\lambda_{0,v'}^2}{\Delta\lambda} f_{0,v'} \qquad \text{(IV-5)}$$

where:

v' = upper vibrational quantum number, 1 and 2 for the (1,0) and (2,0) bands respectively;

$\lambda_{0,v'}$ = wavelength of the $(v',0)$ band, 2149 and 2047 $\overset{\circ}{A}$ for the (1,0) and (2,0) bands respectively;

$f_{0,v'}$ = band oscillator strength; we adopted the values from Marr (1964): $f_{0,1} = 7.8 \times 10^{-4}$ and $f_{0,2} = 6.8 \times 10^{-4}$;

$\Delta\lambda$ = effective width of the bands, $\sim 10 \overset{\circ}{A}$ for both cases.

These values result in the cross-sections
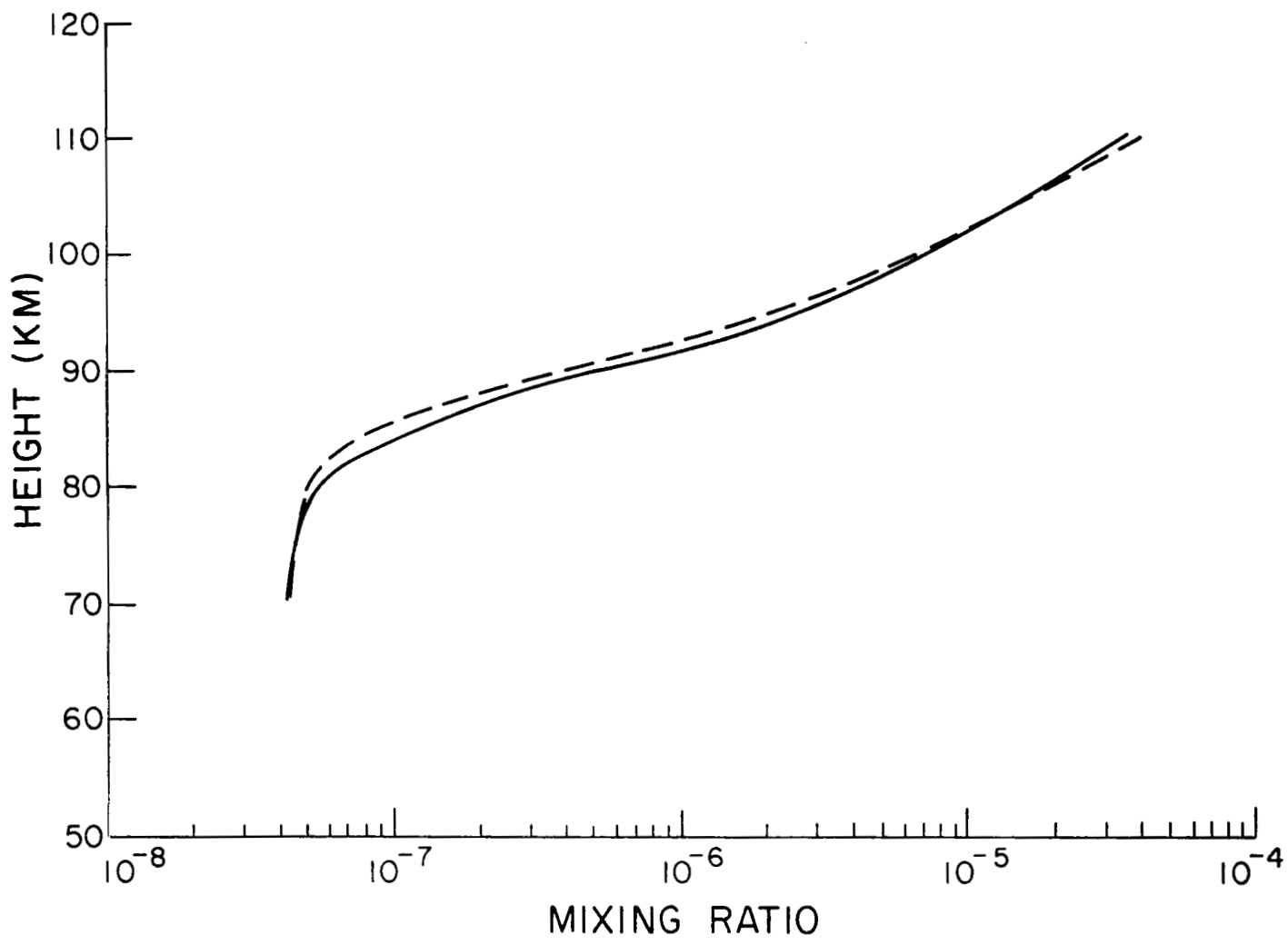
Figure IV-7. Experimental Mixing Ratios of Nitric Oxide.

$$\sigma_{0,1} = 3.2 \times 10^{-18} \, cm^2$$

and

$$\sigma_{0,2} = 2.5 \times 10^{-18} \, cm^2.$$

The vertical column densities can now be computed that would result in a unity optical depth for the gamma bands:

$$\eta = 1.3 \times 10^{17} \, cm^{-2} \text{ for the } (1,0) \text{ band},$$

and

$$\eta = 1.7 \times 10^{17} \, cm^{-2} \text{ for the } (2,0) \text{ band}.$$

The column densities of nitric oxide actually observed are at least two orders of magnitude below these values, implying that the atmosphere is optically thin with respect to absorption in those bands, in the height range considered.

We must also describe the unsuccessful attempt to reduce the scattering of the data points in the emission rate profile by taking into account the polarization of the nitric oxide dayglow emission. Rusch (1969) showed that within certain approximations the resonance scattered radiation in the gamma bands should be about 20% polarized, with equal contribution from all branches. For our instruments, the resolution was small enough that not all branches are seen at the same time and the actual polarization would

be expected to be greater than that number. We tried to detect this effect by a statistical method similar to that employed for Rayleigh scattering, both for the spectral intensity and the integrated band emission. The noise associated with the data precluded any significant result beyond placing an upper limit of 30% on the polarization of the emission, above the predicted value.

There have been other experimental determinations of upper atmospheric nitric oxide densities in the past. In order to place the present measurement in context, Fig. IV-8 presents the results obtained by Barth (1966) and Pearce (1969d).

An upper limit of 10^8 molecules/cm^3 placed by Jursa et al., was derived from their failure to detect nitric oxide by absorption in the delta bands in a twilight experiment. Our results are consistent with their limit.

Barth's determination is lower than ours by a factor of two at 100 km. We suggest this difference is real and reflects a change in nitric oxide density between the times of the two measurements. The two lowest points where Barth measured the column emission rate were 76 and 85 km. At 76 km, he placed a large error bar in the measurement due to Rayleigh scattering. We suggest that the increase of the solar flux, and therefore of the Rayleigh scattering background, underneath the (1,0) gamma band (see Fig. E-1) may have caused the emission rate to be overestimated at that height. The effect of lowering the emission rate to the lower limit of the error
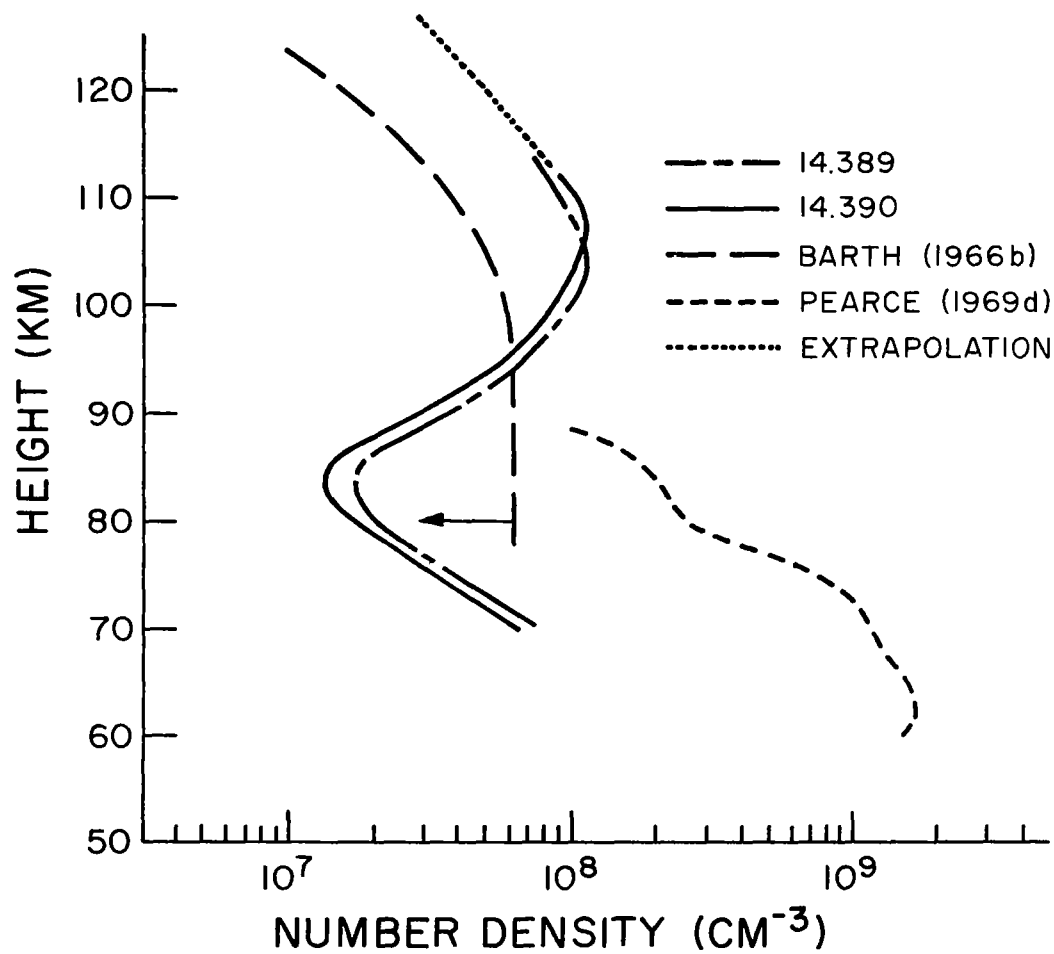
Figure IV-8.   Comparison of Nitric Oxide Measurements.

bar (which is about the same factor by which our emission rates were reduced by background subtraction at that height) is to lower the local density between 76 and 85 km by a factor of two. This possibility is shown by the arrow in Fig. IV-8; it implies that the general shape of Barth's profile is probably not different from ours. Actually, we can use his results to make an estimate of nitric oxide densities above 115 km in the following way.

The overhead column densities of NO above 115 km were found to be:

$$\eta \ = \ 1.75 \times 10^{14} \, cm^{-2} \text{ for } 14.389$$

$$\eta \ = \ 2.45 \times 10^{14} \, cm^{-2} \text{ for } 14.390$$

Using this information and the local densities at 115 km, the profiles were extended upward following the shape of Barth's data (Fig. IV-8).

We suggest Pearce's high values for the nitric oxide density are due to contamination of his emission rate profile by Rayleigh scattering. In the first publication of his results (Pearce, 1968), the author states that the background subtracted from the emission was determined by a linear interpolation between the average signal in the spectral regions (2067 and 2078 Å) and (2382 and 2400 Å). This procedure leaves a significant background unaccounted for in the region of the (1,0) band, as can be seen in Fig. IV-9. This
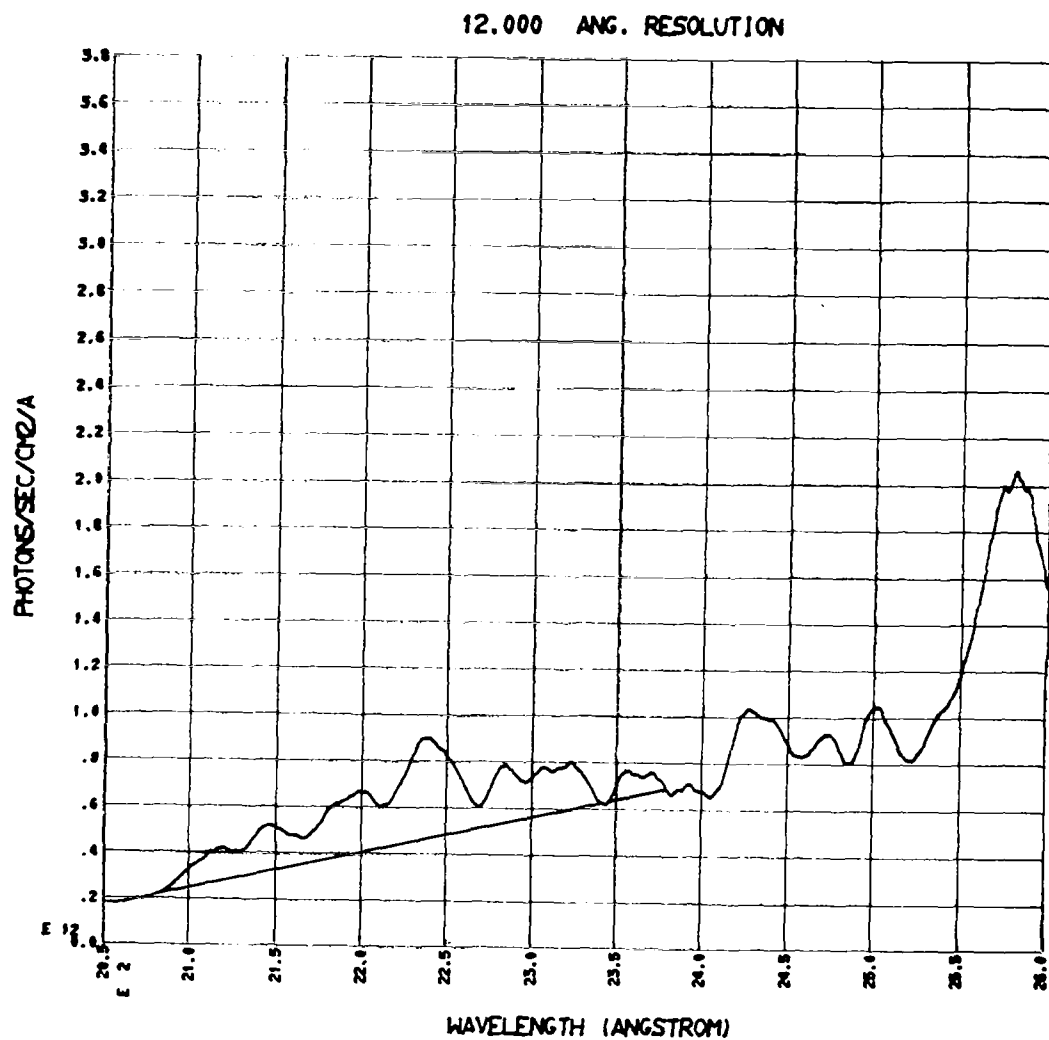
Figure IV-9.   The Solar Ultraviolet Flux (Brinkmann et al., 1965)
for a 12 Å Resolution Instrument, and Approximation
Used by Pearce.

suggestion has the effect of invalidating his conclusion that nitric

oxide is mixed with the atmosphere in the 75 to 96 km region, since

it is based on nitric oxide following the atmospheric distribution and

this in turn can only be considered a fortuitous coincidence, for the

reasons explained above.

CHAPTER V

THE CHEMISTRY OF NITRIC OXIDE

Theoretical considerations of the nitric oxide chemistry

(Barth, 1961; Nicolet, 1965b) have led to the conclusion that NO is

formed from nitrogen atoms, which in turn are a result of ionospheric

reactions in the lower thermosphere. The lifetime of nitric oxide has

been thought to be long enough at mesospheric heights for eddy mix-

ing to dominate its distribution. In the upper stratosphere, equilib-

rium would be reached with nitrogen dioxide, which is produced by

and regenerates nitric oxide in a closed cycle.

According to this reasoning, one would expect to be able to

explain the observed nitric oxide densities on the basis of photo-

chemical theory in the region where photochemical equilibrium pre-

vails (above 90 km, according to Barth, 1961). Actual observations

of nitric oxide (Barth, 1964, and 1966) revealed densities much

higher than those predicted by the simple mechanism for production

and loss of nitric oxide:

$$N + O_2 \rightarrow NO + O \qquad \qquad (V-1)$$

$$N + NO \rightarrow N_2 + O \qquad\qquad (V-2)$$

where the nitrogen atoms are in their ground state.

Hunten and McElroy (1968) suggested that the high concentrations of $O_2(^1\Delta)$ observed by Evans et al. (1968) could explain the NO densities of Barth if the rate of the reaction

$$N(^4S) + O_2(^1\Delta) \rightarrow NO + O \qquad\qquad (V-3)$$
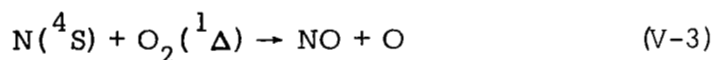
was at least 3×10^{-13} cm^3 sec^{-1}. A recent measurement of this rate coefficient by Clark and Wayne (1969) (also, Wayne, 1969), eliminates that possibility by implying a production rate of nitric oxide two orders of magnitude lower than necessary.

Another possibility for increasing the production rate of nitric oxide is that the nitrogen atoms which react with molecular oxygen (reaction V-1) are in the excited (^2D) state (Norton, 1967). Recently, Norton and Barth (1970) have considered in more detail the photochemistry of nitric oxide and nitrogen (in the (^4S) and (^2D) states) in the region from 90 to 160 km. Their conclusion is that nitric oxide densities of the same order as those measured by Barth (1966) can be explained in terms of production by excited atomic nitrogen, provided dissociative recombination of NO^+ is very efficient in producing nitrogen atoms in the (^2D) state.

58

In order to compare our measurements with theoretical nitric oxide densities, we shall consider a simplified version of the reaction scheme used by Norton and Barth. The densities of excited nitrogen, ground state nitrogen, and nitric oxide, are computed from the atmospheric data presented in Appendix E, with the assumption of photochemical equilibrium, for the 70 to 130 km region. The unknown fraction of nitrogen atoms from dissociative recombination of NO^+ which are in the excited (^2D) state is chosen so that the model will fit the experimental nitric oxide density at 105 km, since photochemical equilibrium is believed to prevail at this height. The comparison involves data from 31 January (flight 14.389) only since there are no significant differences from the second experiment.

Excited (^2D) nitrogen atoms are formed and destroyed by the reactions

$$NO^+ + e \xrightarrow{\alpha^*} N(^2D) + O \tag{V-4}$$

$$N(^2D) + O_2 \xrightarrow{k_1} NO + O \tag{V-5}$$
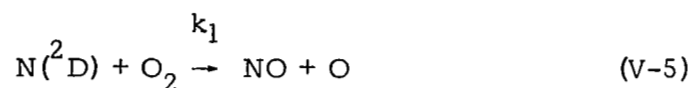
The rate coefficient for the dissociative recombination of NO^+ resulting in $N(^2D)$ has not been measured; following Norton and Barth, we shall say it is a constant fraction of the total dissociative recombination rate α_T:

$$\alpha^* = r\,\alpha_T \qquad \text{(V-6)}$$

where α_T has a value of $4.5 \times 10^{-7}\,(300/T)\,cm^3\,sec^{-1}$ (T is the temperature in degrees Kelvin), according to the review by Biondi (1968), and r is an adjustable parameter (see below).

Norton and Barth also found that deactivation of $N(^2D)$ is negligible, and that a better agreement with the experimental nitric oxide densities of Barth (1966) is obtained if the reaction

$$N_2^+ + O \rightarrow NO^+ + N \qquad \text{(V-7)}$$

does not produce excited nitrogen very efficiently. Accordingly, we shall neglect both processes.

The rate coefficient for reaction (V-5) has been measured to be $k_1 = 5 \times 10^{-12}\,cm^3\,sec^{-1}$ (Lin and Kaufman, 1969).

Ground state nitrogen (^4S) is generated and destroyed mainly by

$$NO^+ + e \xrightarrow{\alpha} N(^4S) + O \qquad \text{(V-8)}$$

and

$$N(^4S) + NO \xrightarrow{k_2} N_2 + O \qquad \text{(V-9)}$$
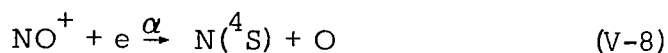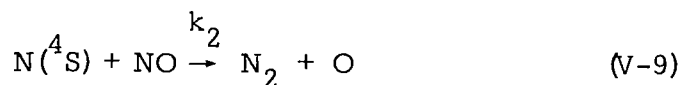
with the rate coefficients $\alpha = (1-r)\,\alpha_T$ (see above), and $k_2 = 2.2 \times 10^{-11}$ (Phillips and Schiff, 1962).

60

We shall neglect the production of ground state nitrogen by the reactions

$$O^+ + N_2 \rightarrow NO^+ + N \qquad\qquad (V-10)$$

and

$$N_2^+ + O \rightarrow NO^+ + N \qquad\qquad (V-11)$$

Norton (1967) showed these to be relatively unimportant sources of nitrogen above 100 km. That the same is true in the region from 70 to 100 km is shown in Appendix D. Photodissociation of molecular nitrogen and nitric oxide can also be neglected as sources of atomic nitrogen in a first approximation (Hudson and Carter, 1969).

Nitric oxide itself is produced and destroyed mainly by the reactions

$$N(^2D) + O_2 \xrightarrow{k_1} NO + O \qquad\qquad (V-12)$$

$$N(^4S) + NO \xrightarrow{k_2} N_2 + O \qquad\qquad (V-13)$$

$$O_2^+ + NO \xrightarrow{\gamma_1} NO^+ + O_2 \qquad\qquad (V-14)$$
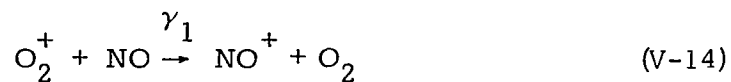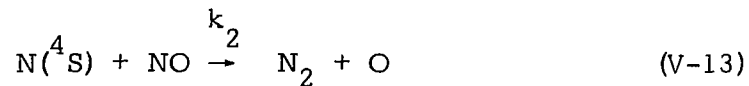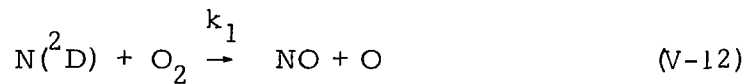
according to the scheme of Norton and Barth (1970).

In photochemical equilibrium, the density of excited nitrogen can be written, from reactions (V-4) and (V-5):

$$[N(^2D)] = \frac{\alpha^*[NO^+]n_e}{k_1[O_2]} \qquad (V-15)$$

where a symbol inside square brackets denotes the number density of that constituent, and n_e is the electron density.

For ground state nitrogen, we have from (V-8) and (V-9):

$$[N(^4S)] = \frac{\alpha[NO^+]n_e}{k_2[NO]} \qquad (V-16)$$

Finally, from Eqns. (V-12) through (V-14), the nitric oxide density is

$$[NO] = \frac{k_1[O_2][N(^2D)]}{k_2[N(^4S)] + \gamma_1[O_2^+]} \qquad (V-17)$$

After rearranging, the number densities of the three unknown constituents can be written explicitly in terms of the factor r and the known atmospheric parameters from Appendix E :

$$[N(^2D)] = \frac{r\,\alpha_T[NO^+]n_e}{k_1[O_2]} \qquad (V-18)$$

$$[N(^4S)] = \frac{(1-r)\,\gamma_1\,[O_2^+]}{(2r-1)\,k_2} \qquad\qquad (V\text{-}19)$$

$$[NO] = \frac{(2r-1)\,\alpha_T\,[NO^+]\,n_e}{\gamma_1\,[O_2^+]} \qquad\qquad (V\text{-}20)$$

At 105 km, the experimental nitric oxide density is about $1 \times 10^8\,cm^{-3}$. From Eqn. (V-20), it is found that r must be equal to 0.87 (87% of the nitrogen atoms from dissociative recombination of NO^+ are in the excited state) for the theoretical nitric oxide density to have the same value as in the experiment. Using this value of r in Eqns. (V-18) through (V-20), the densities of excited and ground state atomic nitrogen and nitric oxide, are computed for the interval from 70 to 130 km. The results of the calculations are presented in Fig. V-1, together with the experimental nitric oxide profile.

The computed NO densities agree with the measured values in the region around 105 km, since the unknown fraction of excited nitrogen atoms from dissociative recombination of NO^+ was chosen with this objective. The gradual decrease of the theoretical densities above that height is also consistent with our measurements and Barth's data (Figure IV-8).
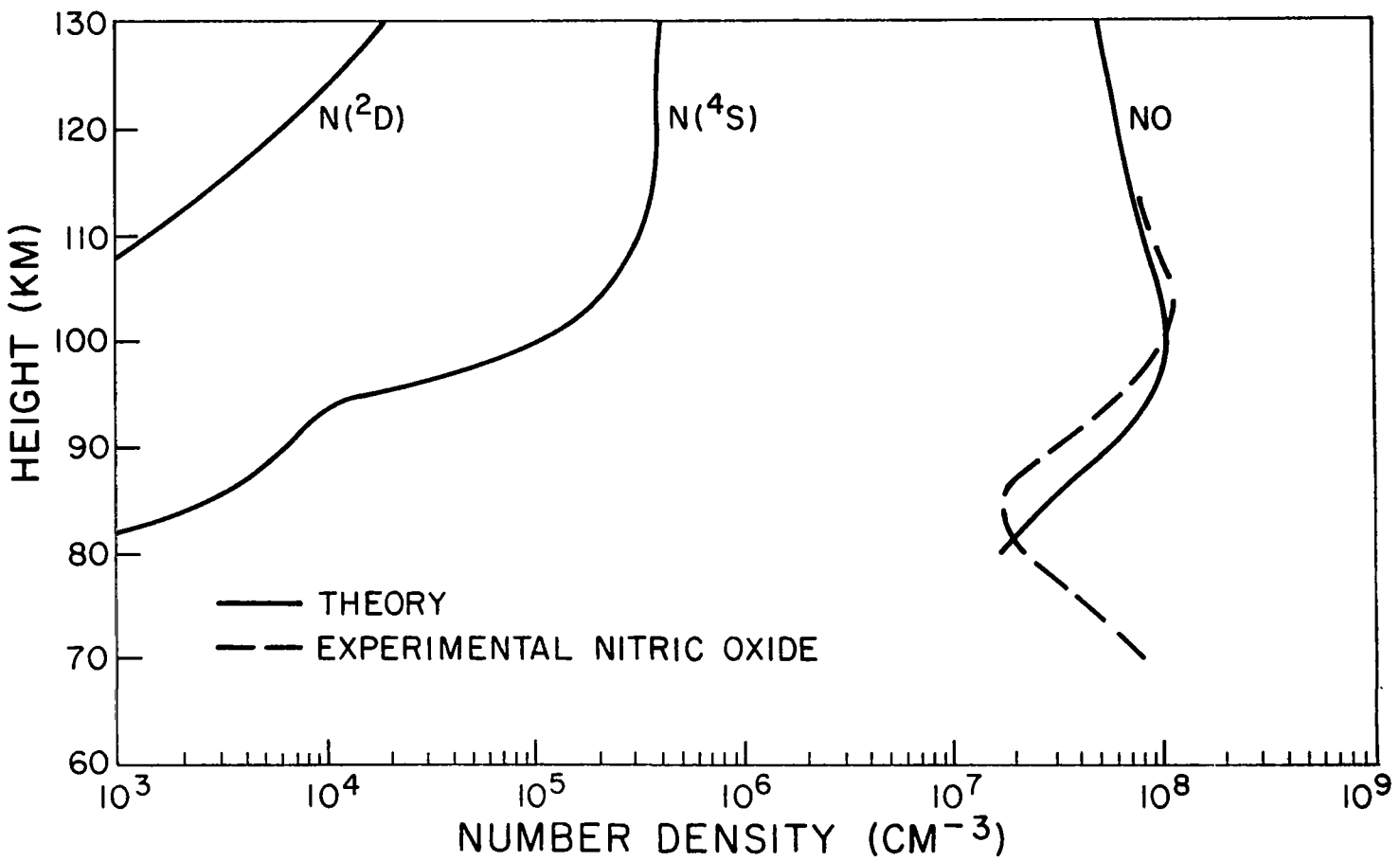
Figure V-1. Photochemical Equilibrium Density Profiles for NO, N(^{4}S) and N(^{2}D). Experimental NO Profile from Flight 14.389.

We conclude that the $N(^2D)$ mechanism (normalized to the experimental data at 105 km) is able to explain the decrease in nitric oxide density from 100 down to 90 km. The agreement must be considered good, given the uncertainties in the model.

Norton and Barth (1970) also found that below 94 km the time constant for eddy mixing becomes shorter than the time scale for chemical destruction of nitric oxide. This result is consistent with the observed increase of nitric oxide densities in the lower portion of the experimental profile. Notice that the conclusion that eddy mixing dominates the nitric oxide distribution below a certain height is independent of the source invoked to explain the nitric oxide densities in the region from 100 to 110 km.

Although Norton and Barth stopped their calculations at 90 km, the time scale for chemical destruction of nitric oxide by atomic nitrogen is expected to be longer than the mixing time scale even below that height, since the atomic nitrogen density decreases even further below 90 km, according to Eqn. (V-16) and the observed decrease in electron density.

We then expect that in the lowest portion of our height range the distribution of nitric oxide will be dominated by eddy mixing down to a point where oxidation by ozone transforms it into NO_2 in substantial amounts. In order to find out where this point is, let us consider the group of reactions

$$O_3 + NO \xrightarrow{k_3} NO_2 + O_2 \qquad (V\text{-}21)$$

$$O + NO + M \xrightarrow{k_4} NO_2 + M \qquad (V\text{-}22)$$

$$O + NO \xrightarrow{k_5} NO_2 + h\nu \qquad (V\text{-}23)$$

$$NO_2 + h\nu \xrightarrow{J} NO + O \qquad (V\text{-}24)$$

$$O + NO_2 \xrightarrow{k_6} NO + O_2 \qquad (V\text{-}25)$$
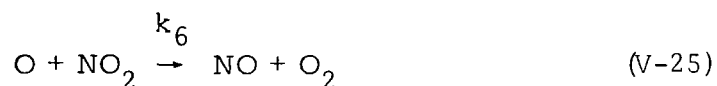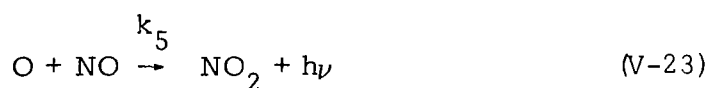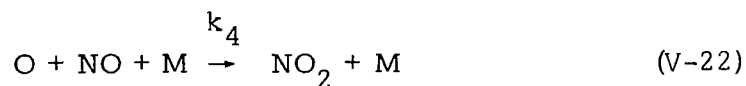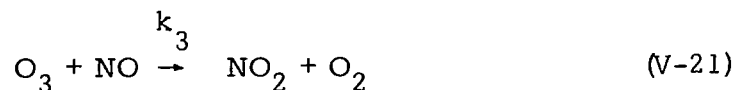
These are the main reactions responsible for the transformation of NO

into NO_2 and vice-versa. Notice that all reactions leading into NO_2

consume a NO molecule, and all losses of NO_2 lead back to nitric

oxide. It is therefore proper to consider the continuity equation for

the sum of the NO and NO_2 densities. Since there are virtually no

loss terms, the lifetime against chemical destruction is very long

and a constant mixing ratio should prevail for these two elements

below the mesopause. Which fraction of the odd nitrogen atoms is

in the form of NO and which in the form of NO_2 can be found by com-

puting the ratio $[NO_2]/[NO]$. The reaction rates for reactions $(V\text{-}21)$

through $(V\text{-}25)$ are respectively:

66

$$k_3 = 9.25 \times 10^{-13} e^{-1300/T} cm^3 sec^{-1} \text{ (review by Schiff, 1969),}$$

$$k_4 = 1 \times 10^{-31} (300/T)^{2.5} cm^6 sec^{-1} \text{ (review by Schiff, 1969)}$$

$$k_5 = 6.2 \times 10^{-17} cm^3 sec^{-1} \text{ (Fontijn et al., 1964),}$$

$$J = 5 \times 10^{-3} sec^{-1} \text{ (Leighton, 1961),}$$

$$k_6 = 2.8 \times 10^{-11} e^{-550/T} cm^3 sec^{-1} \text{ (Phillips and Schiff, 1962).}$$

By equating the production and loss of NO_2 to the loss and production of NO respectively, we find the following values for the ratio:

Height (km)	$[NO_2]/[NO]$
50	2.0×10^{-3}
60	9.0×10^{-4}
70	2.6×10^{-4}
80	8.9×10^{-5}

in general agreement with the results of Nicolet (1965a). The conclusion is that throughout this height range the transformation of nitric oxide into nitrogen dioxide cannot significantly decrease the density of the former constituent, under daytime conditions.

As a final remark, one must notice that the transition between the region where nitric oxide is in photochemical equilibrium and the region where its distribution is dominated by eddy mixing is a gradual one, and diurnal changes in the nitric oxide density associated with changes in the ionospheric E region should be expected above roughly 90 km.

CHAPTER VI

NITRIC OXIDE AND THE D REGION OF THE IONOSPHERE

As explained in Chapter I, photoionization of nitric oxide by solar Lyman-alpha is a potentially important source of ions in the D region of the ionosphere. This constitutes the main motivation for interest in mesospheric nitric oxide.

We shall therefore consider in this Chapter the implications to the lower ionosphere of the nitric oxide profiles deduced from our experiments. Since there are no marked differences between the results for 31 January and those for 6 February, we shall consider the former day in all calculations.

There are essentially three aspects of the ionic chemistry in the D region upon which the nitric oxide measurements have a direct bearing: the total ion-pair budget, the production of NO^+, and the loss mechanism for NO^+. Also, at 85 km and above, where most of the O_2^+ ions are converted into NO^+, some conclusions can be drawn about the chemistry of O_2^+.

The ion production rate from the photoionization reaction:

$$NO + h\nu \rightarrow NO^+ + e \qquad (VI-1)$$

was computed as a function of height using the experimental nitric oxide profile and the vertical column density of molecular oxygen derived from the University of Illinois – G.C.A. Lyman-alpha experiment; the Lyman-alpha flux outside the atmosphere was assumed to be 5.5 erg/cm^2/sec (see Appendix E). The ionization cross section of NO at 1216 Å (Lyman-alpha) is 2 x 10^{-18} cm^2 (Watanabe, 1954). The results are shown in Fig. VI-1, together with the O$_2^+$ production rate from

$$O_2(^1\Delta) + h\nu \rightarrow O_2^+ + e \qquad (VI-2)$$
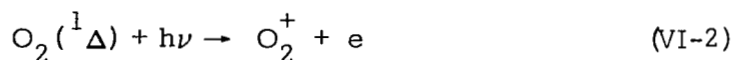
These values were taken from Hunten and McElroy (1968) and multiplied by 1.3 to correct for a calibration revision (see Hunten, 1969); their calculation was for a zenith angle of 60°, which is sufficiently close to the 63° of our fight. The photoionization cross-section of O$_2(^1\Delta)$ has recently been determined in the laboratory (Wayne, 1969) and found to be of the order of magnitude of the value adopted by Hunten and McElroy (3 x 10^{-18} cm^2), but possible larger by a factor less than two.

Also included in Fig. VI-1 is the ion pair production rate of O$_2^+$ from X-rays and Lyman-beta, inferred from the loss rate of this ion (see below).

It can be seen from Fig. VI-1 that photoionization of nitric oxide by solar Lyman-alpha is indeed the main source of ions in the
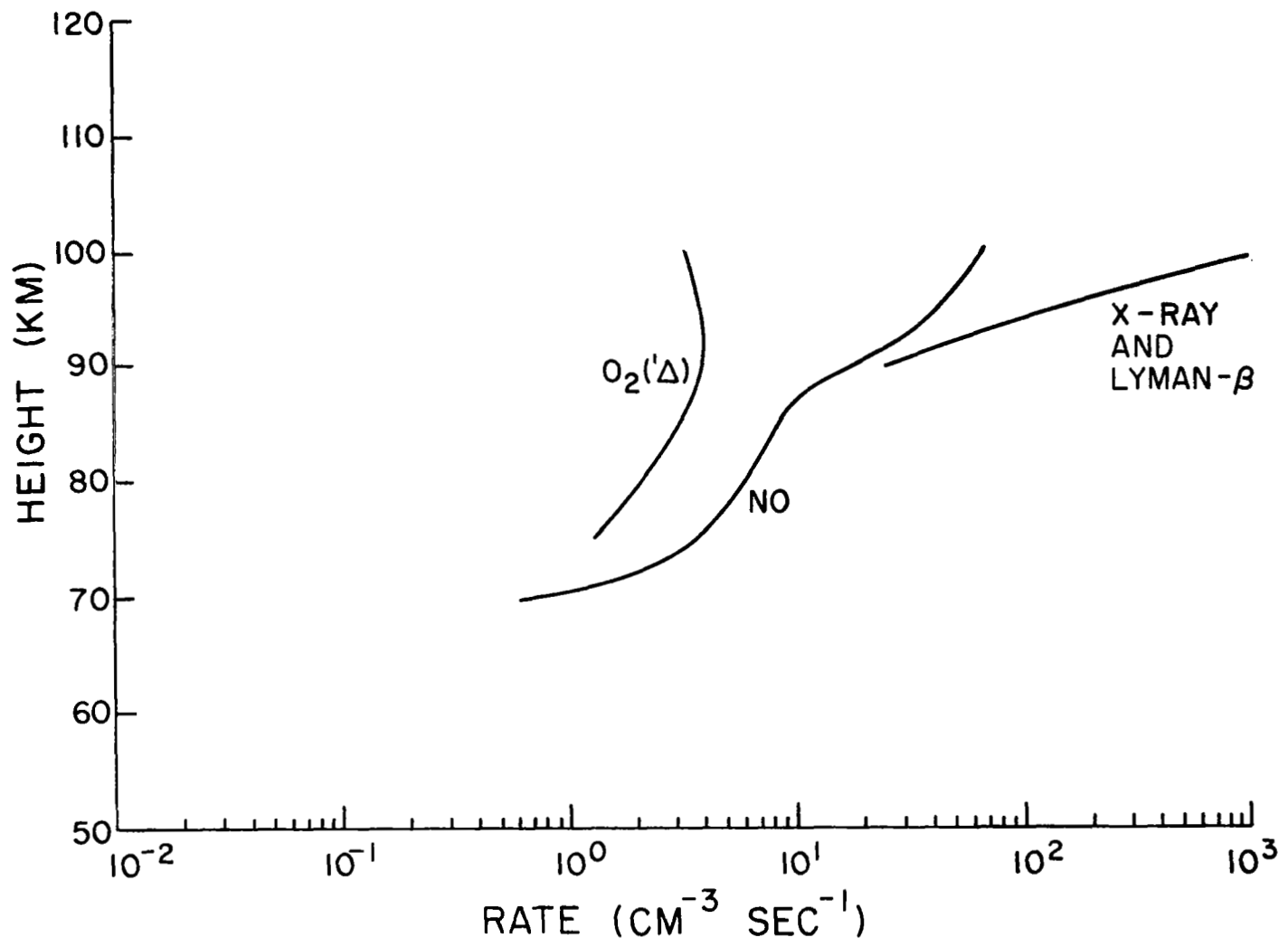
Figure VI-1.   Total Ion-Pair Production.

middle D region for conditions of the experiment. This result is derived from actual measurements of the nitric oxide density.

Let us now consider the problem of the origin of NO^+ ions. Photoionization of NO is its obvious source, but charge transfer from O_2^+ also plays a role:

$$O_2^+ + NO \xrightarrow{\gamma} NO^+ + O_2 \qquad\qquad (VI-3)$$
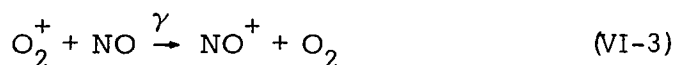
with $\gamma = 8 \times 10^{-10} cm^3 sec^{-1}$ (Ferguson et al., 1965). Figure VI-2 shows the production rates of NO^+ from these two sources. O_2^+ densities were taken from the electron density profile and relative current ratio in the mass spectrometer (see Appendix E). A third curve is included corresponding to the reaction suggested by Nicolet (1965b):

$$O_2^+ + N_2 \rightarrow NO^+ + NO \qquad\qquad (VI-4)$$
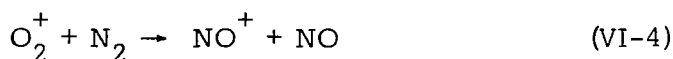
Ferguson et al. (1965) determined an upper limit of $10^{-15} cm^3 sec^{-1}$ for this rate coefficient in the laboratory. This value was used in the calculation for illustrative purposes. Donahue (1966) suggested that the actual value should not be greater than $10^{-16} cm^3 sec^{-1}$. His conclusion, however, was based on dissociative recombination being the loss mechanism for NO^+ below 85 km, which does not seem
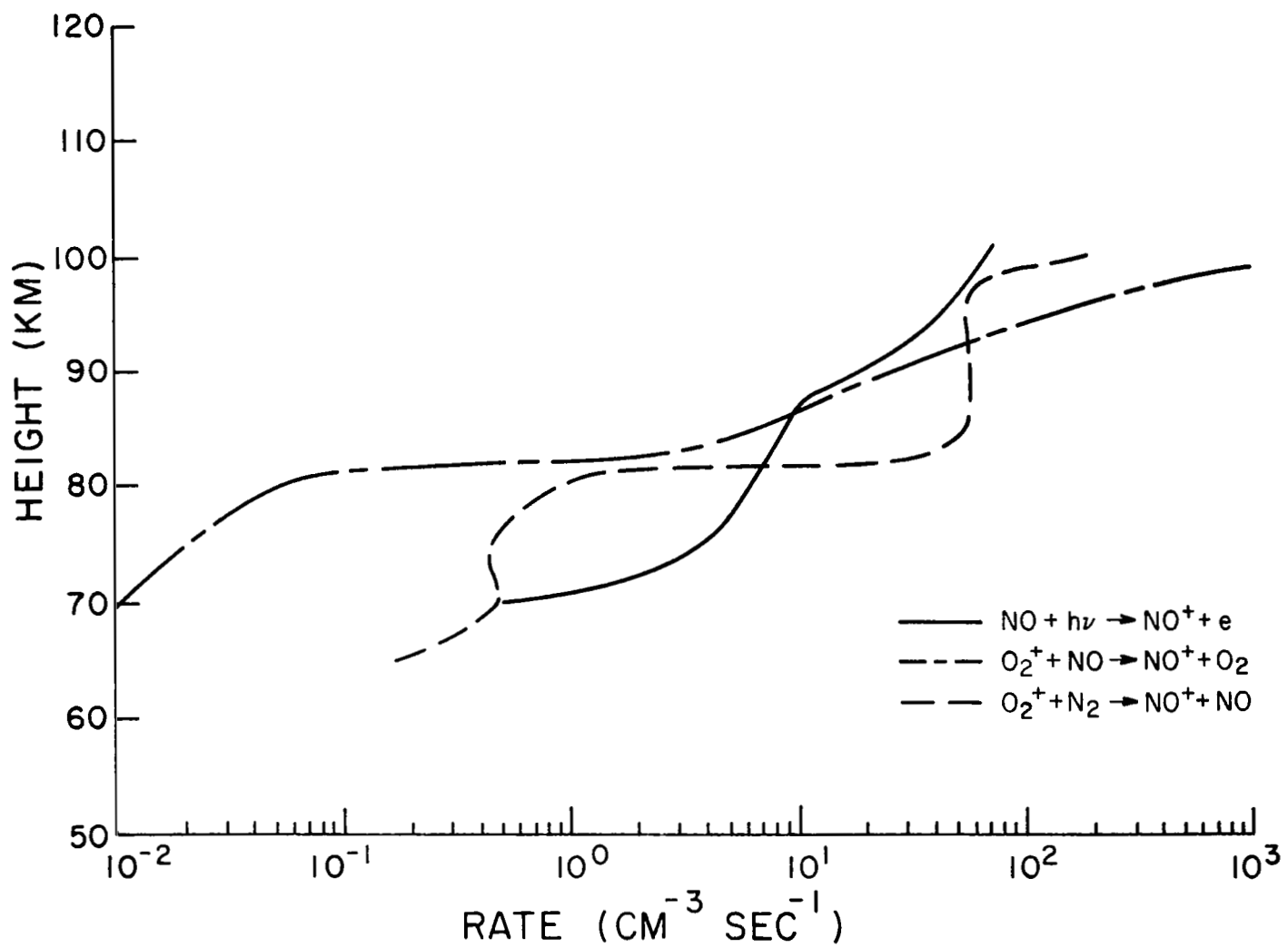
Figure VI-2.   Production Rate of NO$^+$.

Legend:

NO + hν → NO$^+$ + e

O$_2^+$ + NO → NO$^+$ + O$_2$

O$_2^+$ + N$_2$ → NO$^+$ + NO

HEIGHT (KM)

RATE (CM^{-3} SEC^{-1})

to be true (Fehsenfeld et al., 1969, Reid, 1970). We reached

essentially the same conclusion from a different approach.

Since we have a nearly simultaneous measurement of O_2^+

densities and its loss rate (by reaction with nitric oxide, VI-3

and with molecular nitrogen, VI-4), we can state that in equilibrium

the sum of the losses is equal to the production rate; in the region

above 87 km, this production must be due to X-rays and Lyman-beta.

Inclusion of the $O_2^+ + N_2$ reaction (VI-4) with a rate coefficient of

10^{-15} cm^3 sec^{-1} (see Fig. VI-2) implies a production profile from

X-rays and Lyman-beta with a plateau in it (since it is the sum of

the curves for the reactions of O_2^+ with NO and N_2). However, a

smooth profile is expected for the ion production profile from X-rays

and Lyman-beta (Bourdeau et al., 1966). Photoionization of

$O_2(^1\Delta)$ could produce a plateau in the same height range, but the

ion production rate would have to be ten times larger than it is

presently thought to be. Our conclusion is therefore that the rate

coefficient for reaction (VI-4) must be smaller than 10^{-16} cm^3 sec^{-1}

and accordingly we neglected it as a source of NO^+. The production

rate of O_2^+ is also plotted in Fig. VI-1 as the total X-ray and Lyman-

beta contribution to electron production, since the N_2^+ ions produced

are rapidly transformed into O_2^+.

Returning to the NO^+ problem, we conclude from Fig. VI-2

that photoionization of NO completely dominates the production of

NO^+ below 82 km. Charge transfer from O_2^+ becomes equally as effective at 86 km, and dominates increasingly upward.

We next investigated the mechanisms for loss of NO^+ that might be consistent with the observed densities of this ion and the production rates presented earlier. Thus, above 85 km we find that for a dissociative recombination mechanism, a rate coefficient of 7×10^{-7} cm^3 sec^{-1} is implied, in good agreement with laboratory determinations. This is the same result obtained by Reid (1970). For the region below 82 km, dissociative recombination is too slow a process. Chemical reactions involving water vapor have been suggested as possible means of providing for a faster loss of NO^+ (Fehsenfeld and Ferguson, 1969, and Reid, 1970). Another alternative is that negative ions are actually important for the neutralization of NO^+. The knowledge of either mechanism is not sufficient at this time for a decision to be made. The important point here, however, is that the available data does require a faster mechanism than dissociative recombination for the loss of NO^+ below 82 km.

CHAPTER VII

SUMMARY

Two sets of observations were made of the nitric oxide
fluorescence dayglow in the (1,0) gamma band by means of scanning
ultraviolet spectrometers aboard Nike-Apache rockets. Careful con-
sideration of the Rayleigh scattering contribution to the dayglow per-
mitted the determination of nitric oxide densities to be significantly
improved over previous experiments.

From the measured nitric oxide densities, it is concluded
that photochemical equilibrium is prevalent above about 90 km, while
mixing dominates below that altitude. Quantitative consideration is
given to a model for the nitric oxide chemistry in which excited ni-
trogen (^2D) is responsible for its formation. This model can explain
the significant observed features of the nitric oxide profile, provided
the recombination of nitric oxide ions produces excited nitrogen atoms
more efficiently than ground state atoms.

The contribution of nitric oxide ionization by Lyman-alpha
to the ionospheric total ion production is found to be dominant in
the middle D region. Dissociative recombination is concluded to be
an adequate loss mechanism for nitric oxide ions above 85 km,
while a faster mechanism is required below 82 km.

REFERENCES

Allen, C.W., Astrophysical Quantities, The Athlone Press, London, 1963.

Anderson, J.G., and L.G. Meira, Jr., "Polarization of Rayleigh Scattered Radiation," L.A.S.P. Memorandum to Dr. C.A. Barth 1969.

Barth, C.A., "Nitrogen and Oxygen Atomic Reactions in the Chemosphere," in Chemical Reactions in the Lower and Upper Atmosphere, J. Wiley & Sons, New York, 1961.

Barth, C.A., "Rocket Measurement of the Nitric Oxide Dayglow," J. Geophys. Res., 69, 3301, 1964.

Barth, C.A., "Nitric Oxide in the Upper Atmosphere," Ann. Geophysique, 22, 198, 1966.

Biondi, M.A., "Atmospheric Electron-Ion and Ion-Ion Recombination Processes," Can. J. Chemistry, 47, 1711, 1969.

Blake, A.J., J.H. Carver, and G.N. Haddad, "Photo-Absorption Cross Sections of Molecular Oxygen between 1250 and 2350 Å," J. Quant. Spectrosc. Radiat. Transfer, 6, 451, 1966.

Bourdeau, R.E., A.C. Aikin, and J.L. Donley, "Lower Ionosphere at Solar Minimum," J. Geophys. Res., 71, 727, 1966.

Bowhill, S.A., "D-Region Morphology and Processes," in Meteorological and Chemical Factors in D-Region Aeronomy - Record of the Third Aeronomy Conference, University of Illinois, April, 1969.

Brinkmann, R.T., A.E.S. Green, and C.A. Barth, "A Digitalized Solar Ultraviolet Spectrum," Jet Propulsion Laboratory Tech. Report No. 32-951, 1966.

Clark, I.D., and R.P. Wayne, "The Reaction of $O_2(^1\Delta)$ with Atomic Oxygen and with Atomic Nitrogen," Chem. Phys. Letters, 3, 405, 1969.

Colegrove, F.D., F.S. Johnson, and W.B. Hanson, "Atmospheric Composition in the Lower Thermosphere," J. Geophys. Res., 71, 2227, 1965.

Craig, R.A., The Upper Atmosphere, Meteorology and Physics, Academic Press, New York, 1965.

Ditchburn, R.W., and P.A. Young, "The Absorption of Molecular Oxygen between 1850 and 2500 Å," J. Atmos. Terr. Phys., 24, 127, 1962.

Donahue, T.M., "On the Ionospheric Conditions in the D Region and Lower E Region," J. Geophys. Res., 71, 2237, 1966.

ESSA Solar-Geophysical Data (Prompt Report), October, 1969.

Evans, W.F.J., D.M. Hunten, E.J. Llewellyn, and A. Vallance Jones, "Altitude Profile of the Infrared Atmospheric System of Oxygen in the Dayglow," J. Geophys. Res., 73, 2885, 1968.

Fehsenfeld, F.C., and E.E. Ferguson, "Origin of Water Cluster Ions in the D Region," J. Geophys. Res., 74, 2217, 1969

Ferguson, E.E., F.C. Fehsenfeld, P.D. Goldan, A.L. Schmeltekopf, and H.I. Schiff, "Laboratory Measurement of the Rate of the Reaction $N_2^+ + O \rightarrow NO^+ + N$ at Thermal Energy," Planet. Space Sci., 13, 823, 1965 .

Fite, W.L., "Positive Ion Reactions," Can. J. Chemistry, 47, 1797, 1969.

Fontijn, A., C.B. Meyer, and H.I. Schiff, "Absolute Quantum Yield Measurements of the NO-O Reaction and Its Use as a Standard for Chemiluminescent Reactions," J. Chem. Phys., 40, 64, 1964.

Goody, R.M., Atmospheric Radiation, I - Theoretical Basis, Oxford University Press, London, 1964.

Hudson, R.D., and V.L. Carter, "Atmospheric Implications of Predissociation in N_2," J. Geophys. Res., 74, 393, 1969.

78

Hunten, D.M., and M.B. McElroy, "Metastable $O_2(^1\Delta)$ as a Major Source of Ions in the D Region," J. Geophys. Res., $\underline{73}$, 2421, 1968.

Hunten, D.M., "Metastable Species as Ionizable Constituents," in Meteorological and Chemical Factors in D Region Aeronomy – Record of the Third Aeronomy Conference, University of Illinois, April, 1969.

Jursa, A.S., Y. Tanaka, and F. LeBlanc, "Nitric Oxide and Molecular Oxygen in the Earth's Upper Atmosphere," Planet. Space Sci., $\underline{1}$, 161, 1959.

Knapp, R.A., and A.M. Smith, "Fatigue Effects in the Luminescent Yield of Sodium Salicylate, App. Optics, $\underline{3}$, 637, 1964.

Krueger, A.J., Private communication, 1969.

Leighton, P.A., Photochemistry of Air Pollution, Academic Press, New York, 1961.

Lin, S.C., and F. Kaufman, Private communication, 1969.

Marchand, F.E., "Angles Measured on MARS Platform," Philco Corporation Intra-Company Communication (GC0967) – Aeronutronics Div., February, 1964.

Marr, G.V., "Electronic Transition Moments and Their Effects on the Band Strengths and Absorption Oscillator Strengths of the NO Beta and Gamma Systems," Proc. Phys. Soc., $\underline{83}$, 293, 1964.

Mechtly, E.A., "Lower Ionosphere Electron Concentration and Collision Frequency from Rocket Measurements of Faraday Rotation, Differential Absorption and Probe Current," J. Geophys. Res., $\underline{72}$, 5239, 1967.

Mechtly, E.A., to be published, 1970.

Narcisi, R.S., and A.D. Bailey, "Mass Spectrometric Measurements of Positive Ions at Altitudes from 64 to 112 Kilometers," J. Geophys. Res., $\underline{70}$, 3687, 1965.

Narcisi, R.S., Private communication, 1969.

Nicolet, M., "Contribution a l'Etude de la Structure de l'Ionosphere," Inst. Roy. Meteorol. Belg. Mem., $\underline{19}$, 162, 1945.

Nicolet, M., and A.C. Aikin, "The Formation of the D Region of the Ionosphere," J. Geophys. Res., 65, 1469, 1960.

Nicolet, M., "Nitrogen Oxides in the Chemosphere," J. Geophys. Res., 70, 679, 1965a.

Nicolet, M., "Ionospheric Processes and Nitric Oxide," J. Geophys. Res., 70, 691, 1965b.

Norton, R.B., "The Ionized Constituents in the 100 to 300 Kilometer Region of the Earth's Upper Atmosphere," Ph.D. Thesis, University of Colorado, 1967.

Norton, R.B., and C.A. Barth, to be published, 1970.

Park, J., and J. London, to be published, 1970.

Pearce, J.B., "Rocket Measurement of Nitric Oxide in the Earth's Atmosphere between 60 and 96 km," Ph.D. Thesis, University of Colorado, 1968.

Pearce, J.B., Private communication, 1969a.

Pearce, J.B., "GATHER Analog to Digital Conversion Program for the LASP PDP-8," LASP Memo, February, 1969b.

Pearce, J.B., "Nitric Oxide Gamma Band Emission Rate Factor," J. Quant. Spectrosc. Radiat. Transfer, 9, 1593, 1969c.

Pearce, J.B., "Rocket Measurement of Nitric Oxide between 60 and 96 Kilometers," J. Geophys. Res., 74, 853, 1969d.

Phillips, L.F., and H.I. Schiff, "Reactions of Hydrogen Atoms with Nitrogen Dioxide and with Ozone," J. Chem. Phys., 37, 1233, 1962.

Ratcliffe, J.A., and K. Weekes, "The Ionosphere," in Physics of the Upper Atmosphere, Ed. by J.A. Ratcliffe, Academic Press, New York, 1960.

Reid, G., to be published, 1970.

Rusch, D.W., Private communication, 1969.

Schiff, H.I., "Neutral Reactions Involving Oxygen and Nitrogen," Can. J. Chemistry, 47, 1903, 1969.

Smith, L.G., Private communication, 1969.

Smith W.S., Private communication, 1969.

Tousey, R., "The Extreme Ultraviolet Spectrum of the Sun,"
   Space Sci. Rev., $\underline{2}$, 3, 1963.

U.S. Standard Atmosphere Supplements, 1966.

Watanabe, K., "Photoionization and Total Absorption Cross Section
   of Gases, I. Ionization Potential of Several Molecules, Cross
   Sections of NH_3 and NO," J. Chem. Phys., $\underline{22}$, 1564, 1954.

Wayne, R.P., Private communication, 1969.

Weeks. L.H., "Lyman-alpha Emission from the Sun near Solar
   Minimum," Ap. J., $\underline{147}$, 1203, 1967.

Weeks, L.H., and L.G. Smith, "A Rocket Measurement of Ozone
   Near Sunrise," Planet. Space Sci., $\underline{16}$, 1189, 1968.

Whitten, R.C., and I.G. Poppoff, Physics of the Lower Ionosphere,
   Prentice Hall, New Jersey, 1965.

Witt, G. "Optical Characteristics of Mesopheric Aerosol Distri-
      butions in Relation to Noctilucent Clouds," Tellus, $\underline{20}$,
      98, 1968.

APPENDIX A

LABORATORY CALIBRATION OF THE INSTRUMENTS

The photometric calibration of the spectrometers was performed in three steps:

1. Spectral transmission of optics in monochromator.

2. Spectral response of detector head.

3. Absolute calibration of instrument.

This Appendix describes each one of the steps briefly, as well as the overall calibration.

Spectral Transmission of Optics in Monochromator

For this measurement a cadmium hollow cathode lamp was used in conjunction with a 1/2 meter focal length bench monochromator. Several emission features of the lamp were selected in the 2000 to 2800 $\overset{\circ}{\text{A}}$ interval, based on the constancy of their intensities. For each one of these features, the signal was measured at the exit slit of the 1/2 meter monochromator and then at the exit slit of the flight unit with both instruments in tandem, using the same photomultiplier tube. The measurement was then repeated at the exit slit of the 1/2 meter instrument. The entire process for each emission line did not take more than five minutes, thus avoiding errors that

might be introduced by fluctuations in any of the components of the system. As a further precaution, the current applied to the source was monitored with a digital voltmeter and never allowed to vary by more than 1%.

The transmission of the optics in the flight unit was then taken as the ratio of the signal measured with the monochromators in tandem to that measured through the bench instrument only. The results are shown in Fig. A-1.

Spectral Response of the Detector Head

The same source and bench monochromator were used as in the optics transmission measurement. The detector head was mounted at the exit slit and the region 1950 to 2850 Å scanned in about 40 minutes. The data were recorded on a strip chart. Next, the same region was scanned using as a detector a 541A photomultiplier tube behind a sodium salycilate covered suprasil plate. Sodium salycilate fluoresces in the presence of UV radiation, emitting in the visible region with a constant quantum efficiency (Knapp and Smith, 1964). The layer was thick enough to avoid passage of direct light, but the photomultiplier tube was chosen to be insensitive to the ultraviolet as a precaution.

For selected spectral features, we then found the ratio of the detector head response to that of the other photomultiplier tube. The results are shown in Fig. A-2.
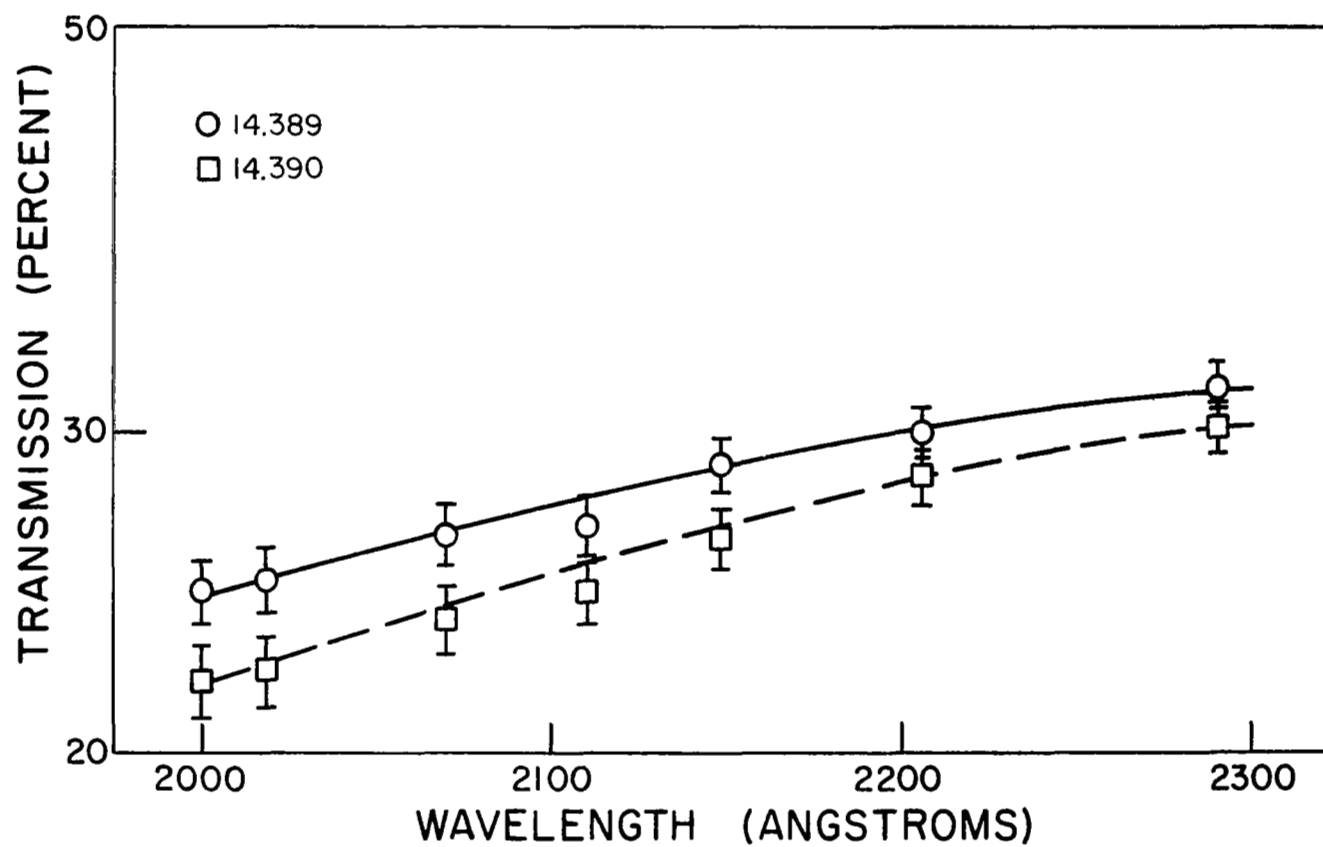
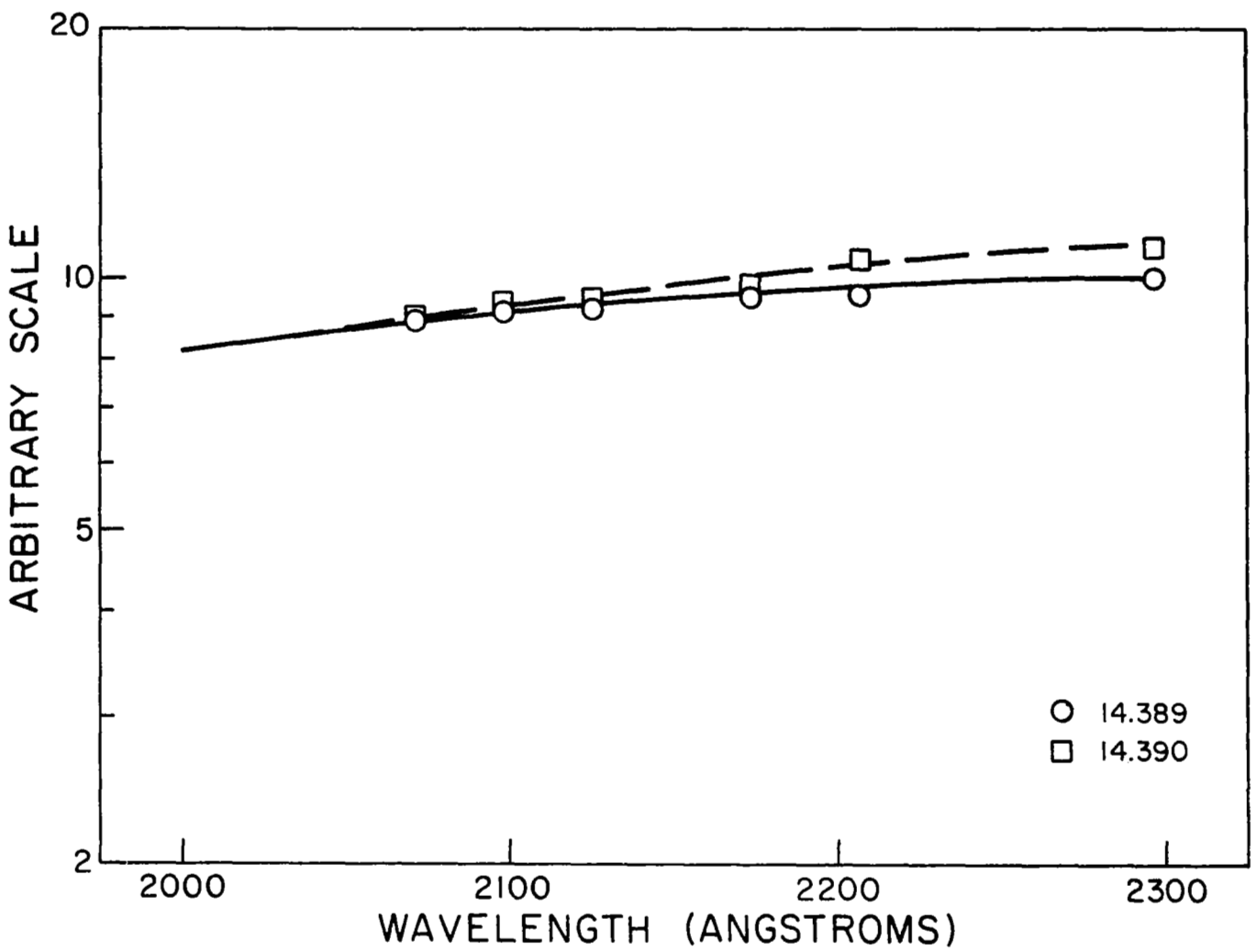Figure A-1.   Transmission of Monochromator Optics.

Figure A-2. Relative Spectral Response of Detector Heads.

Absolute Calibration of the Instrument

The experimental arrangement is shown in Fig. A-3. The source is an EPUV-1097 tungsten lamp, operated at 35 amperes from an Edgarton, Germenhauser & Grier (EG&G) power supply, model 590-11a. The brightness temperature of the lamp was determined to be 2341°K by measurements with an optical pyrometer and comparison with a National Bureau of Standards secondary standard (Pearce, 1969a).

The resulting spectral radiance was multiplied by the transmission of the 2660 Å interference filter in 10 Å intervals from 2500 to 2890 Å and the resulting product integrated numerically with a second degree interpolation using three points. This procedure yielded a radiance of $B = 1.29 \times 10^{13}$ photons/sec/sterad/cm^2.

From the geometry of Fig. A-3, we see that S, the number of photons reaching the detector head per second is:

$$S = B \, T_{qw} \, T_{ql} \, A_s \, A_h \, D^2 / d_1^2 \, d_2^2 \qquad (A-1)$$

where:

T_{qw} = transmission of the quartz window; equal to one, since it was included in the measurement of B;

T_{ql} = 0.900, transmission of the quartz lens;

A_s = 0.120 cm^2, area of the slits;

A_h = 0.0606 cm^2, area of the plate hole;
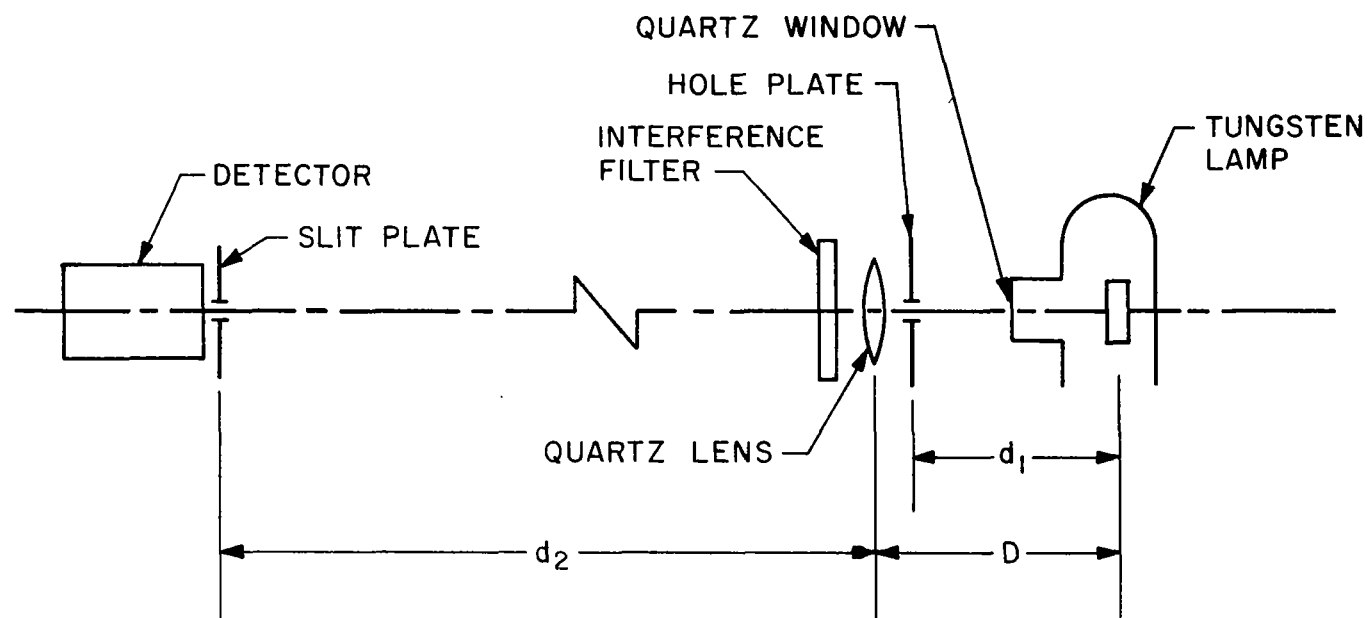
Figure A-3.   Arrangement for Absolute Calibration.

D   =   15.6 cm, distance from the tungsten filament to quartz lens;

d_1 =   16.8 cm, distance from the filament to the hole plate;

d_2 =   507 cm, distance from the quartz lens to the slit plate.

The result is $S = 3.61 \times 10^5$ photons/sec, at 2660 Å.

     This input of light produced certain measured voltages on the low gain output of the electrometers, which were corrected by the relative response of the detector heads at 2660 and 2149 Å, to yield the calibration figures at 2149 Å:

      1.79×10^5 photons/sec/volt for rocket 14.389;

      2.13×10^5 photons/sec/volt for rocket 14.390.

Overall Calibration

     Given an emission intensity (in kiloRayleighs) from an extended source in front of the monochromator chamber, the number of photons per second passing through the exit slit is:

$$ S = 10^9 \, 4\pi I \, \frac{A_g A_s}{f^2} \, T \cos \theta_i \qquad \text{(A-2)} $$

where:

$4\pi I$ =   intensity in kR at input;

A_g =   area of grating, 40.4 cm^2;

A_s =   area of the entrance slit, 0.120 cm^2;

f   =   focal length of instrument, 25.0 cm;

T   =   transmission of optics (grating and mirror), 28.8% for 14.389, and 26.8% for 14.390.

The overall result is then the calibration at 2149 Å:

1.03 kR/volt for rocket 14.389;

1.57 kR/volt for rocket 14.390.

APPENDIX B

DATA REDUCTION

This Appendix describes the data reduction process in terms
of the computer programs used in each phase of it. Figures B-1
and B-2 show flow-graphs for the reduction of the spectrometer and
attitude data, respectively. Notice that some of the programs are
common to both groups.

For the spectrometer data (Fig. B-1), the programs are:

GATHER: as a first step in the processing of the telemetered
data, this program was used with the LASP Digital Equipment Corpora-
tion PDP-8 computer and associated equipment to perform an analog-
to-digital conversion (Pearce, 1969b). A four channel option was
used to digitize three telemetry data channels; the fourth one was
grounded to provide an easily identifiable reference. A digitization
rate of 1000 samples/sec. was used; the triggering signal was ob-
tained by dividing the 100 kHz reference on the telemetry tape by
100. A constant correspondence between the time scale associated
with the data and the count number was thus assured.

Data were written on a digital tape (D-1) compatible with the
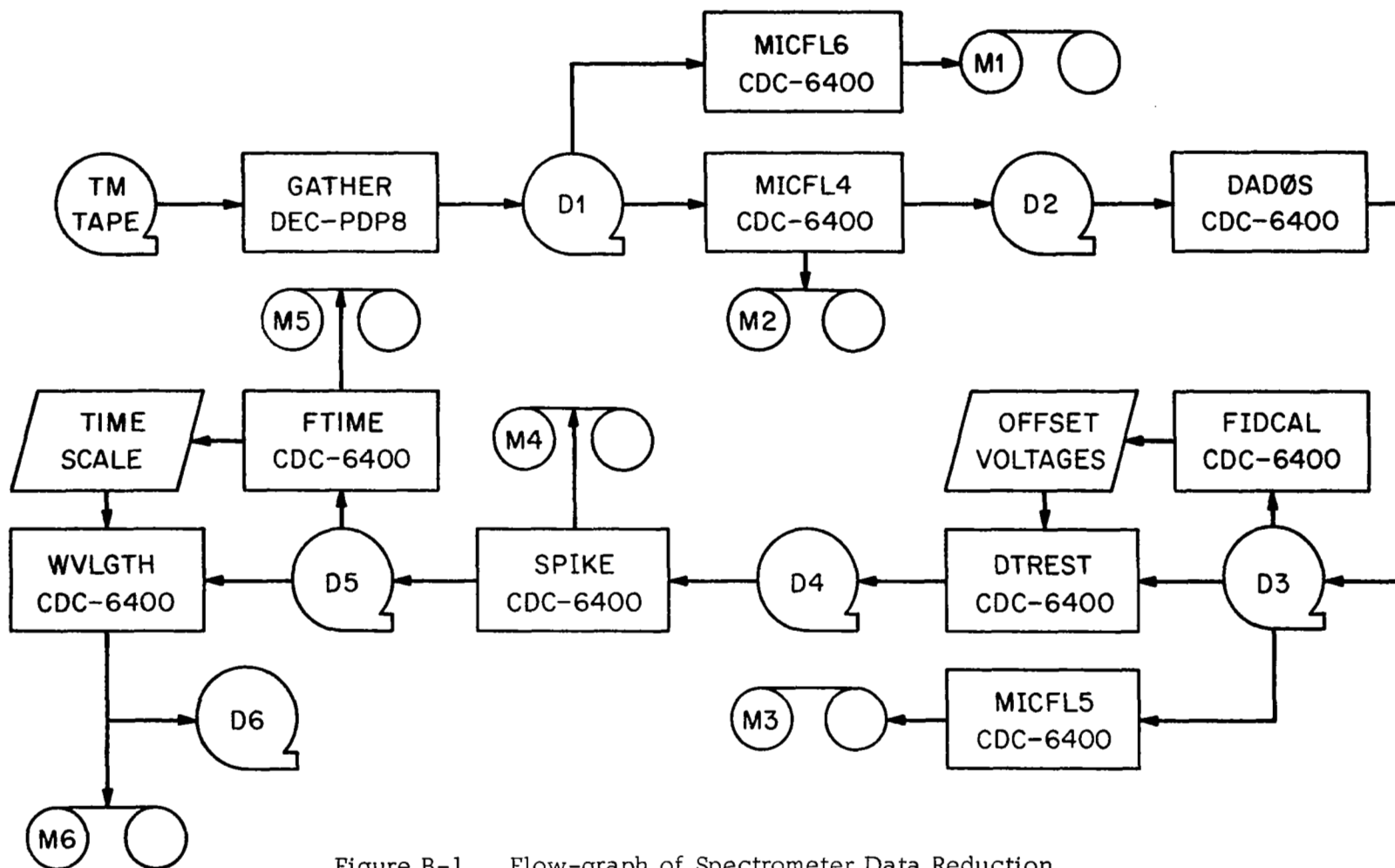University of Colorado's CDC 6400 computer, where the rest of the

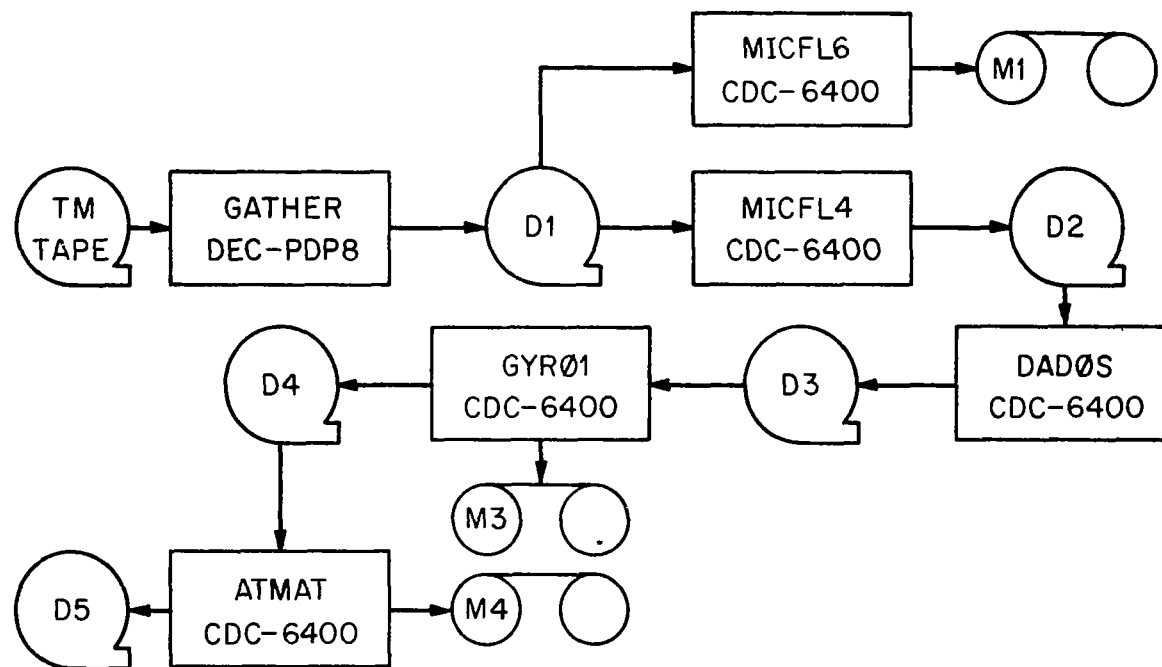Figure B-1.   Flow-graph of Spectrometer Data Reduction.

Figure B-2. Flow-graph of Attitude Data Reduction.

data processing was done. Each data word is an integer from 0 to 4095 (7777 octal), corresponding roughly to the interval -0.5 to 5.5 V in the telemetry signal.

The three channels chosen from the telemetry tape were:

1.   High gain data (output of X10 amplifier);

2.   Low gain data (output of electrometer);

3.   400 cps monitor.

MICFL6: this program read in data from tape D-1 and converted the 12-bit integer words into the 60-bit floating point format of the CDC-6400 in a 0 to 5 scale. A small portion of the data were plotted on microfilm with an expanded time scale, so that the width of fiducial marks, transients, and calibration cycles could be measured. An example is shown in Figure B-3.

MICFL4: data are read from tape D-1 and, as in the preceding program, converted to a 0-5 scale. The (grounded) fourth channel is searched for and used as a reference for identification of the other channels. A search is then made for fiducial marks on the 400 cps monitor channel. If one is found, a further check is performed on the high gain channel to prevent the possibility of a noise impulse being mistaken for a fiducial. The identification is made on the basis of supplied values for upper and lower bounds on the width and height of the fiducial marks. The trailing edge of each mark is taken as the beginning of a new spectral scan and the data is grouped in blocks, approximately 6000 points long, corresponding to
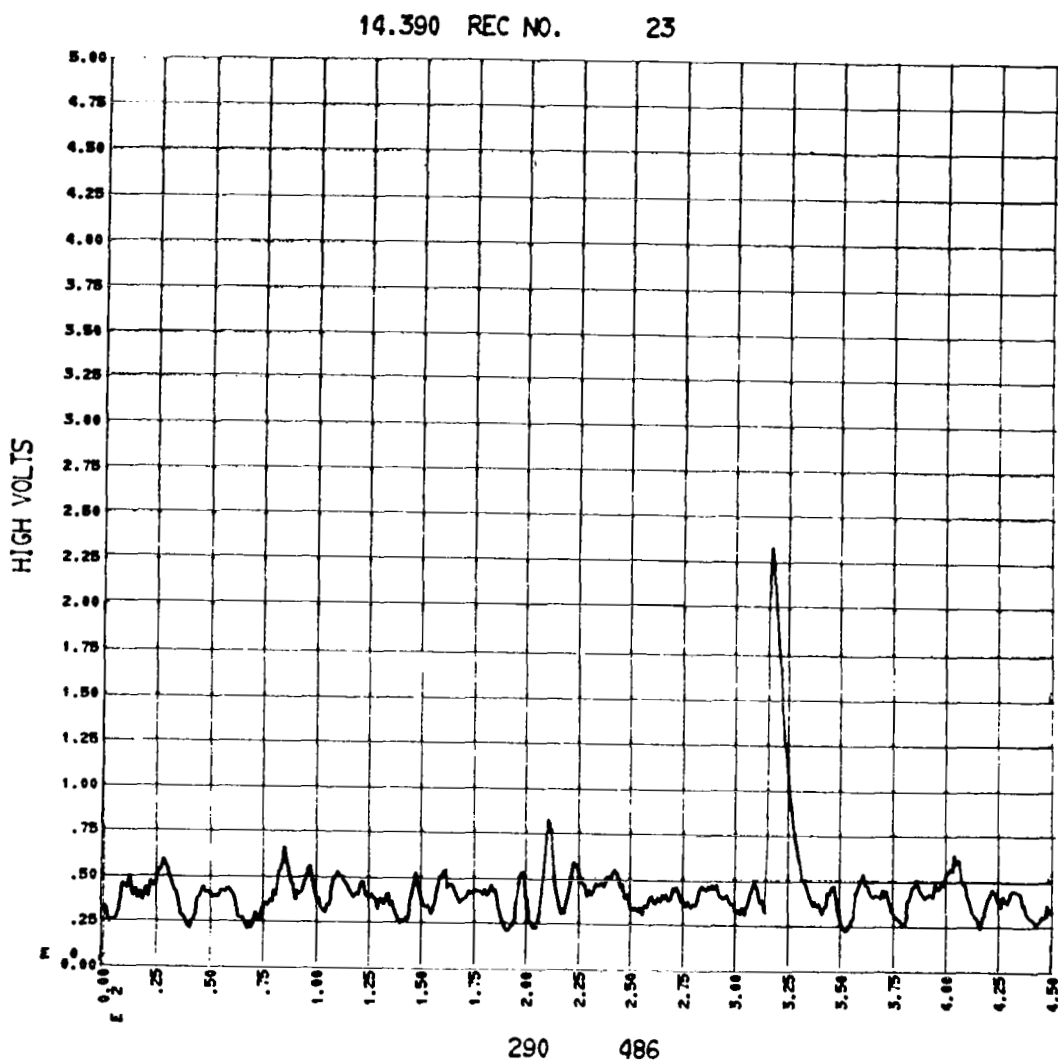
94

Figure B-3.   Frame of Digitized Data Showing Noise Spike.

individual spectral scans. These newly arranged data are written on tape D-2 along with information such as spectrum number, its length in number of points, and the total number of points since the beginning of the data stream before that spectrum. Also, the same data are put on microfilm for verification (see example on Fig. B-4).

DADOS: This program uses the in-flight calibration cycles to restore the signal to a 0 to 5 volts scale. Initially, a search is made for the first series of calibration steps by computing the cross-correlation between the data and a supplied model of the calibration cycle. When this correlation is above 0.6, a relative maximum is searched for; its position is taken as a tentative position for the steps. A determination is then made of the actual width of the calibration steps, and this new value is used in building an improved model for it. The up-dated model is then used in the search for all calibration cycles. Once a cycle is found, an average is taken of the points in the center of each step and a linear least square fit obtained between these averaged and the actual values (0 to 5 V, in 1 V steps). The two constants obtained for each calibration are then used for restoring the data to true voltage values by linearly interpolating between consecutive cycles (except for the ends of the data where the first and last value are used). The output data are written on Tape D-3.

MICFL5: data from tape D-3 are displayed on microfilm. An example is shown in Fig. B-5, which corresponds to the same data

96

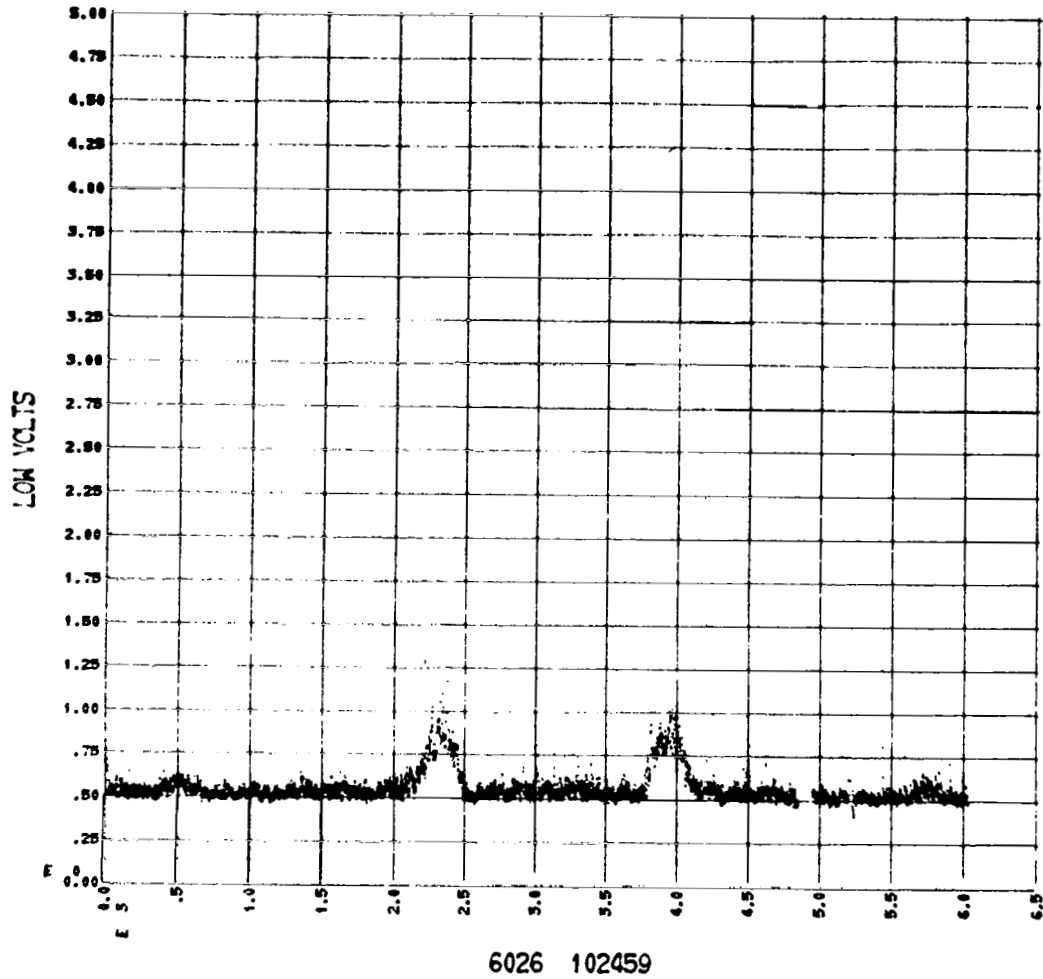Figure B-4. One Spectral Scan, Low Gain Channel; Notice Calibration Steps.
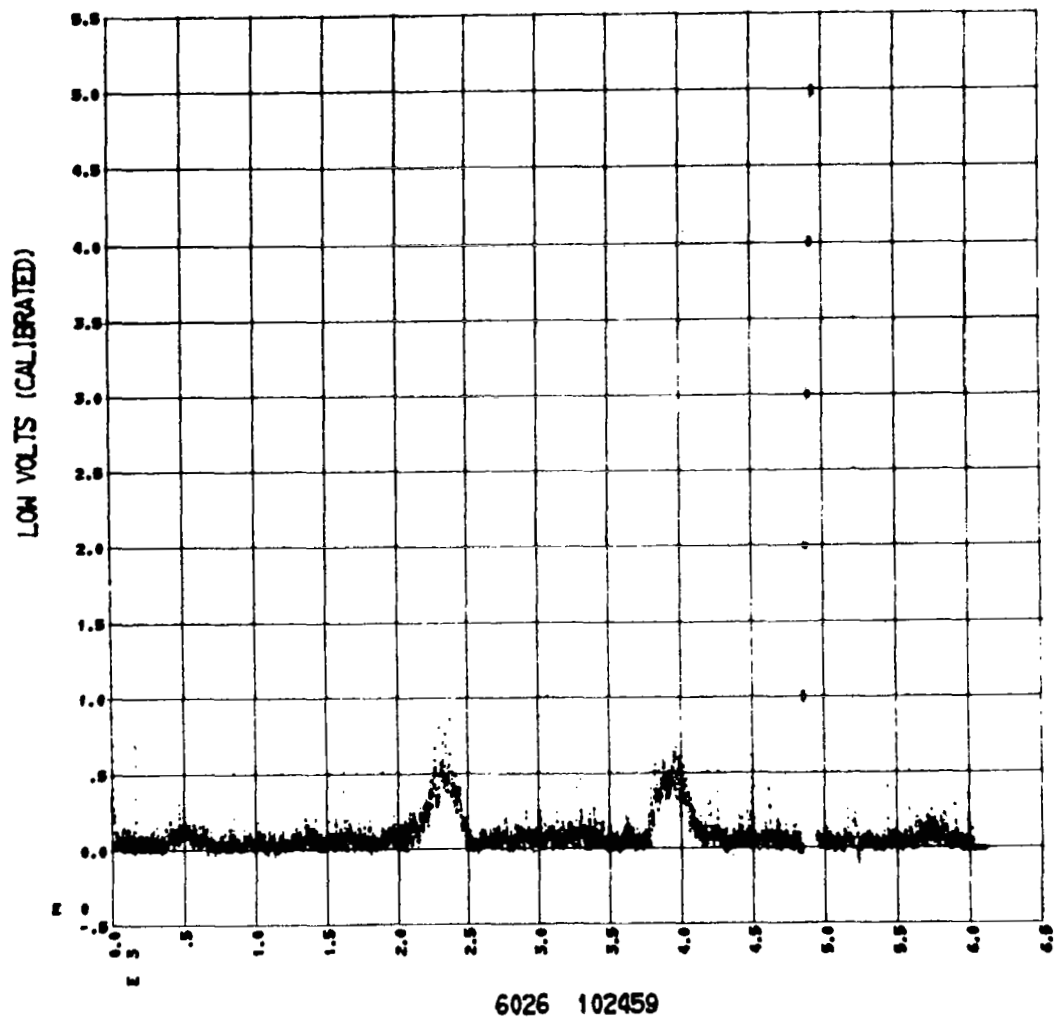
Figure B-5. Same Spectrum as in Fig. B-4, After Calibration.

98

as Fig. B-4. Notice how the steps of the calibration cycle coincide with the one-volt marks, as expected.

FIDCAL: this program determines the offset voltage of both the high and low gain channels by averaging the data in all spectra between lift-off and clamshell ejection at approximately 60 seconds. Excluded from the averaging are all points during calibrations, fiducial marks, and transients, as well as points that fall outside a certain range (a few tenths of a volt) from an eye-estimated average. This precludes noise spikes from contaminating the offset voltages.

DTREST: data from the high and low gain channels are combined, with the former being used whenever possible. The calibrated data are read from tape D-3, and all data points occuring during a fiducial on the high gain channel or its transient on the low gain channel are flagged for identification. Next, points during calibration cycles and those which are off-scale, are also flagged. A new set of data points is then generated by taking either

$$V = (V_{high} - V_{offset,high})/10 \qquad (B-1)$$

or

$$V = V_{low} - V_{offset,low} \qquad (B-2)$$

according to whether the high gain point is flagged or not. The resulting data are written on tape D-4.
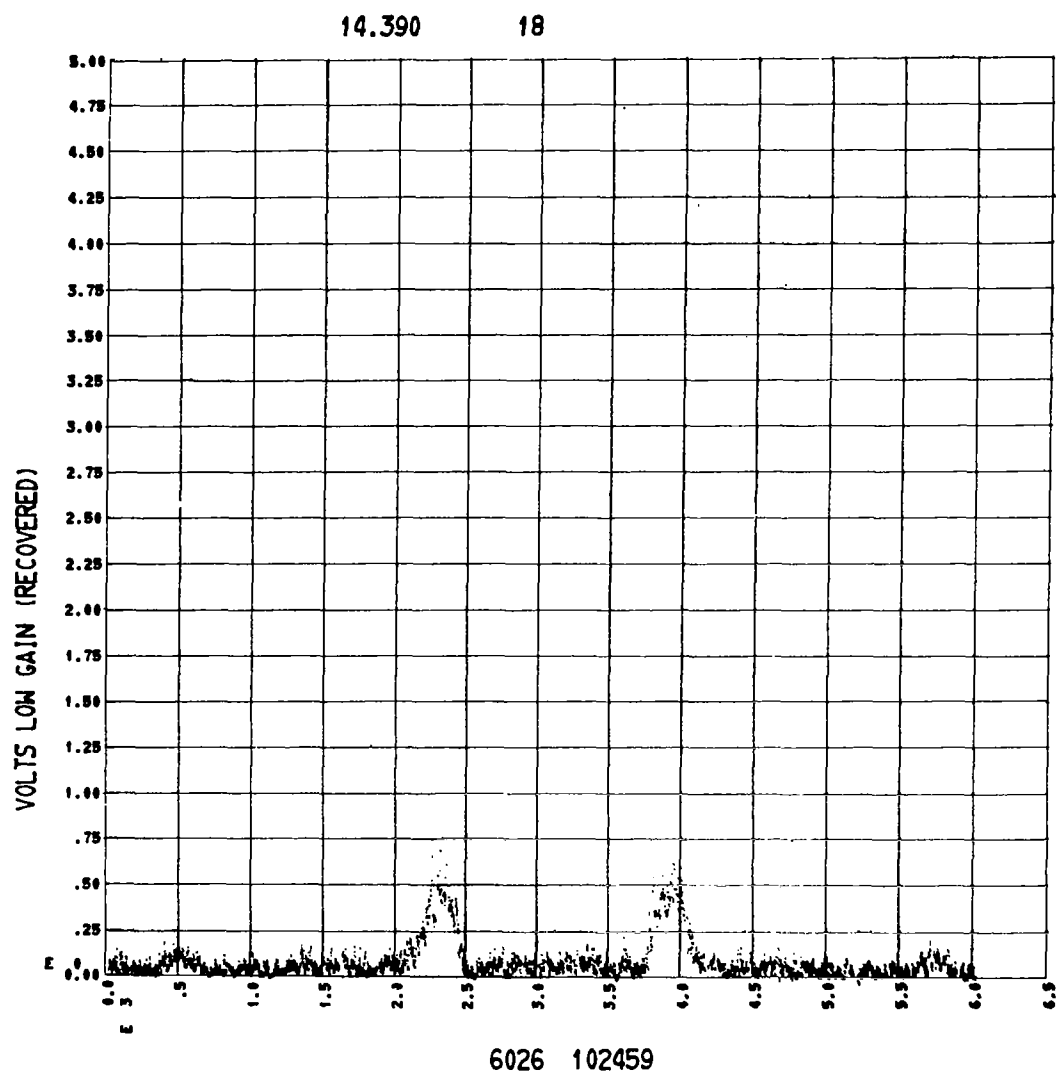
Figure B-6.   Spectrum After Noise Removal; Same Data as Two
Preceding Figures.

100

SPIKE: this program searches all recovered data from D-4 for noise spikes and flags the corresponding points. One such spike can be seen in detail in Fig. B-3. The criterion used for the recognition of a noise spike is the fact that it has a very abrupt rise and an exponential-like decay. They were therefore defined as being any sequence of points wherein the difference between two consecutive points was initially positive and greater than 0.2 V, then positive, and finally negative. The spike was considered to end where the difference became positive again. The minimum initial difference of 0.2 V for two periods 1 msec apart corresponds to a time scale of the order of a few milliseconds. Therefore, there was no danger of masking a spectral feature since for these the time scale is of the order of (resolution in $\overset{\circ}{A}$) x (scan period)/(scan range in $\overset{\circ}{A}$), or 100 msec.

The output data are written on tape D-5, and on microfilm for visual checking. Notice in Fig. B-6, portraying the same spectrum as Figs. B-4 and B-5, that the noise spikes were eliminated.

FTIME: the purpose of this program is to establish time and wavelength scales for the spectrometer data. The time of occurence of each calibration cycle was read from the paper telemetry record (which has on the edge 36-bit coded time pulses from a ground station clock). In terms of the digitized data, the position of the calibrations was determined by the program DADOS. These data were

combined to obtain a linear least square fit relating flight time in seconds to point number.

For the wavelength scale, all of the spectra showing the nitric oxide gamma bands were averaged. The second half of the averaged spectrum was then reflected on the first one. The folding point was changed until the correlation between the two halves reached a maximum. This was taken as the correct folding point; finally, it was used to add both halves of the averaged spectrum. Fig. B-7 shows the averaged spectra before and after folding for both flights. The change in the relative position of the (1,0) and (2,0) bands is due to the different orientation of the grating, as explained in Chapter II.

WVLGTH: a wavelength scale was determined by a linear correspondence between the known wavelengths of the (1,0) and (2,0) gamma bands (2149 and 2047 $\overset{\circ}{A}$, respectively), and the position of these bands determined from the microfilm plot of the averaged spectrum for each flight.

The data were then converted from volts into photometric units by means of the expression:

$$4\pi I(\lambda) \;=\; \frac{C_o \, S(n(\lambda))}{T(\lambda) \, G(\lambda) \, R(\lambda)} \tag{B-3}$$

where:

$4\pi I$ = specific flux of the signal in kR/$\overset{\circ}{A}$;

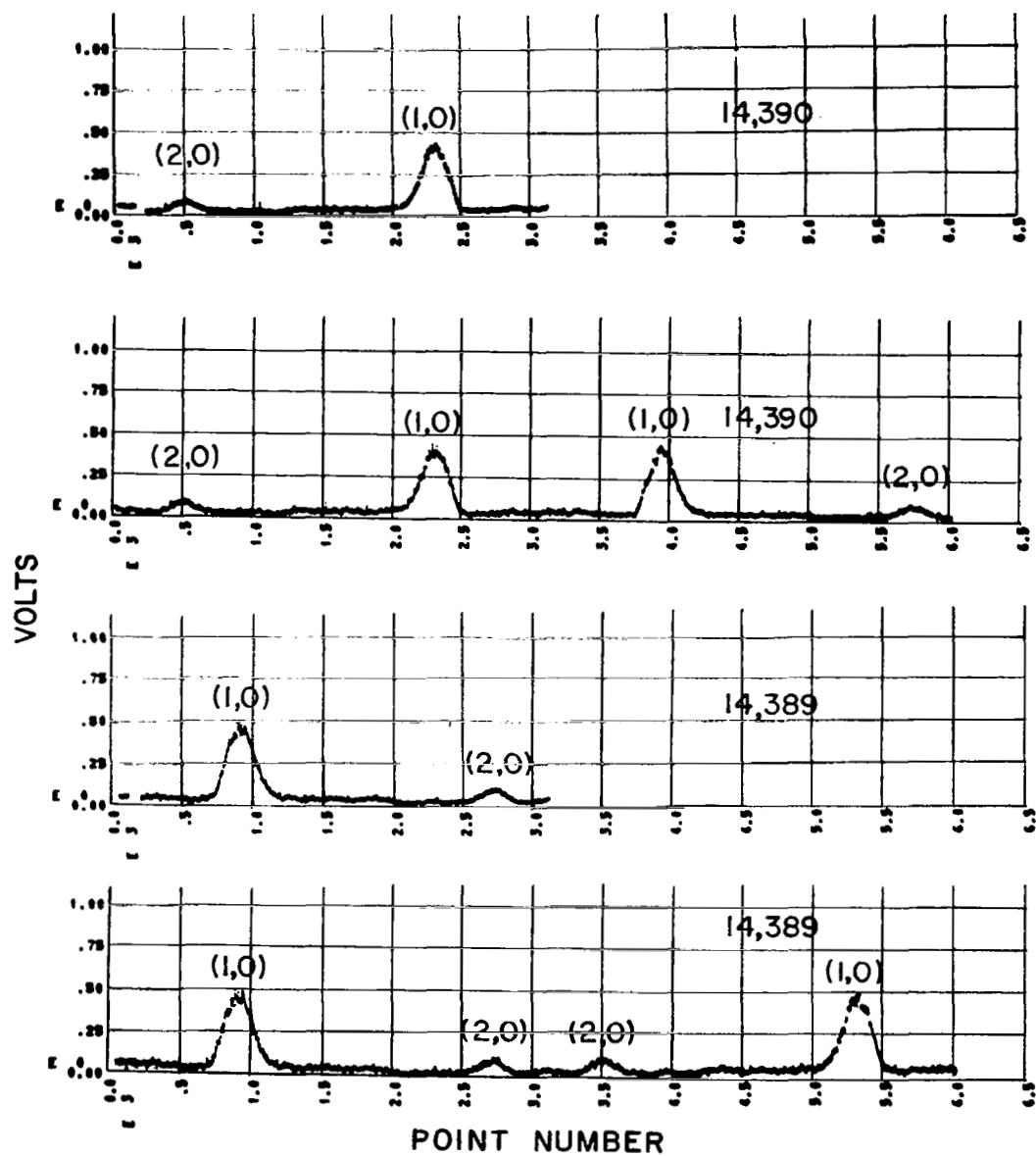λ = wavelength in $\overset{\circ}{A}$;

102

Figure B-7. Average of 34 Spectra, Two Flights. Nitric Oxide
Gamma Bands Indicated.

C_o = calibration of the instrument at the reference wavelength (2149 Å), in kR/V;

G = relative response of the detector head, unity at 2149 Å;

T = relative transmission of the monochromator chamber, unity at 2149 Å;

S = signal at the output of the electrometer (low gain channel) in V;

n = number of the data point counted from the trailing edge of the preceding fiducial;

R = resolution of the instrument in Å.

The functions $T(\lambda)$ and $G(\lambda)$ were approximated by fifth degree polynominals from the laboratory data. These are presented in Figs. A-1 and A-2.

The wavelength scale $\lambda(n)$ was initially chosen in the laboratory by exposing the instruments to a source which included the (1,0) and (2,0) gamma bands of nitric oxide and mechanically fixing the grating arm to the grating shaft so that both bands were included in the 150 Å scan range in first order. The final accurate scale was then determined in the program FTIME from the flight date.

The resolution of each instrument was computed as a function of wavelength for every data point.

The resulting data were written on tape D-6 and plotted as a function of wavelength on microfilm (see Fig. B-8).

For the attitude data, the sequence of programs went as follows (see Fig. B-2):

GATHER through MICFL5: same as for the spectrometer data, except that the three channels chosen were roll, pitch and yaw.

GYRO1: the attitude data generated by the gyroscope on board of the rocket is in the form of a voltage, with a certain scale factor for conversion into degrees (18, 9 and 12 degrees/volt, respectively, for roll, pitch and yaw). In order for the data to fit into the 0 to 5 V telemetry channel, they are stepped back to zero each time they reach 5 volts. This program inverts the procedure and brings the data back into continuous curves. The resulting data (angles in degrees) are written on tape D-4.

ATMAT: initially, this program flags the points during the calibration cycles. A time scale is found in the same manner as the spectrometer data. The data are then taken in blocks of 100 points every 0.2 sec. and a least square linear fit is found between the angles and the times corresponding to every tenth of the 100 points. This linear fit is used to compute the angle at the center of the interval. Extrapolation of the preceding points is used during the calibration cycles. The result is a set of three angles, roll,
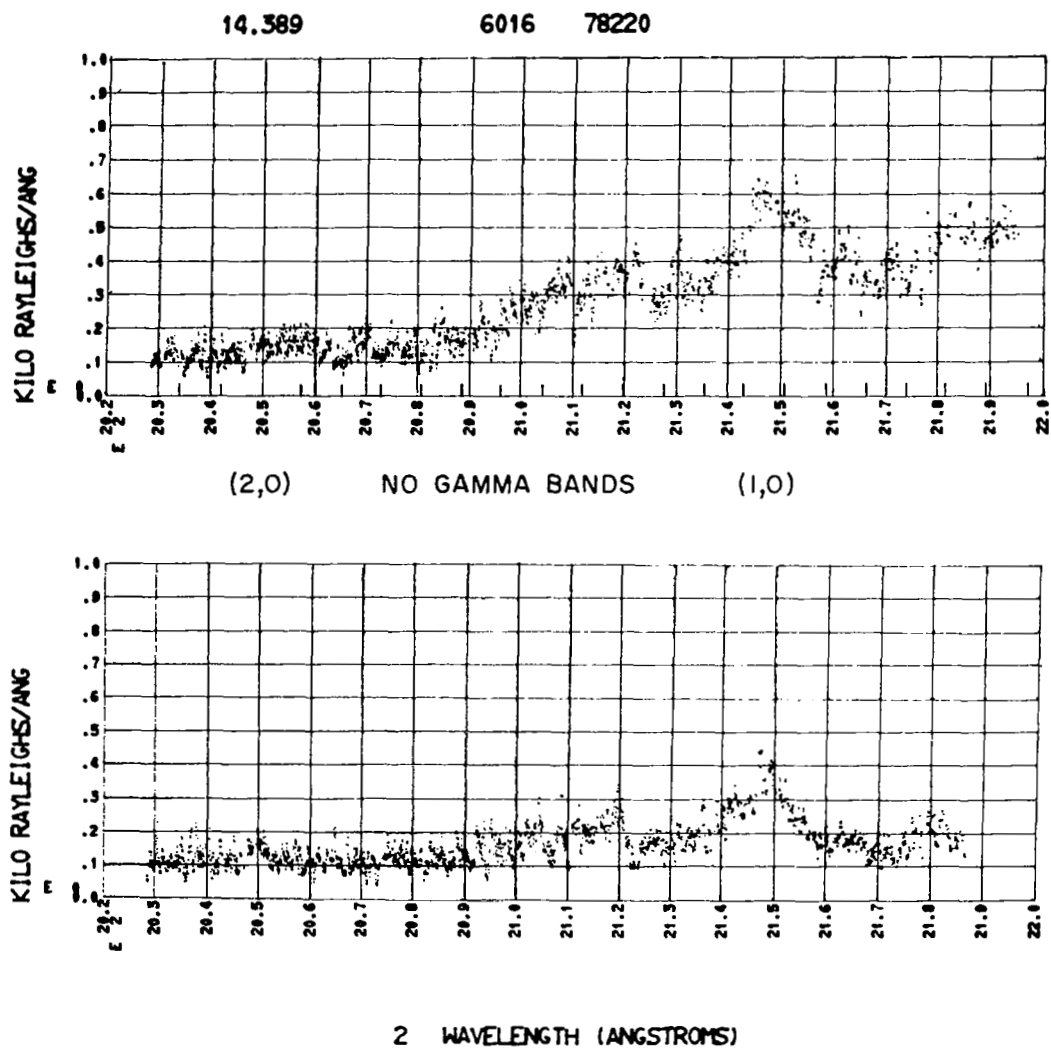
Figure B-8. Spectrum of Completely Reduced Data. Marks Added Every 1/2 Roll Period to Emphasize Modulation of Rayleigh Scattering Background.

106

pitch, yaw every 0.2 sec., starting at lift-off. Also, the roll rate is computed, since it has more meaning than the roll angle itself. The results are written on tape D-5.

The attitude data are used later in the data processing to compute the angles between the optical axis of the instrument and the radius vector to the sun or the local vertical, at any given time. Also important for the polarization of the signal is the angle that defines the rotation of the instrument, (see Appendix C).

All angles are computed by means of scalar products of vectors in a reference frame fixed with respect to the launcher at all times (reference system G_2 below). The vertical at the rocket can be expressed in the launcher frame by taking into account the horizontal range of the rocket at any given time.

The vectors fixed with respect to the spectrometer are transformed from the rocket frame to the launcher frame by means of the rotation matrices described below.

Let us define the reference systems:

R : fixed on the rocket (x, roll axis; y, pitch axis; z, yaw axis);

T_1 : fixed on the launcher at the moment of uncaging of the gyroscope, inertial from then on. Axes same as in R, before uncaging;

T_2 : has same x axis as T_1, but z is defined in the plane containing the local vertical and x;

G_1 : x, up; y, East; z, North; determined at the lanucher at the moment of uncaging, inertial afterwards;

G_2 : same as above, but the directions are from the launcher at all times.

Let $\vec{X}_A$ represent a vector in the reference frame A. We then have the sequence of rotations:

$$\vec{X}_{G_2} = (C)\vec{X}_{G_1} = (C)(T)\vec{X}_{T_2} = (C)(T)(A)\vec{X}_{T_1} = (C)(T)(A)(R)\vec{X}_R \quad (B-4)$$

where the matrices are (in what follows, s and c stand for sine and cosine functions):

$$(C) - \text{Coriolis Matrix;} \quad \vec{X}_{G_2} = (C)\vec{X}_{G_1}$$

$$(C) = \begin{pmatrix} s^2L + c^2L\,c\Omega(t-t_g) & s\Omega(t-t_g)\,cL & sL\,cL\,(1-c\Omega(t-t_g)) \\ -s\Omega(t-t_g)\,cL & c\Omega(t-t_g) & s\Omega(t-t_g)\,sL \\ sL\,cL\,(1-c\Omega(t-t_g)) & -s\Omega(t-t_g)\,sL & c^2L + s^2L\,c\Omega(t-t_g) \end{pmatrix}$$

$$(B-5)$$

where:

L = geocentric latitude of launcher;

Ω = angular velocity of the Earth;

t =   time;

t_g =   time of uncaging of the gyroscope;

$$(T) - \text{Tower Tilt Matrix;} \quad \vec{X}_{G_1} = (T)\vec{X}_{G_2}$$

$$(T) = \begin{pmatrix} sE\ell & 0 & -cE\ell \\ cE\ell \, sAz & cAz & sE\ell \, sAz \\ cE\ell \, cAz & -sAz & sE\ell \, cAz \end{pmatrix} \qquad (B-6)$$

where:

$E\ell$ =   actual elevation of launcher;

Az =   actual azimuth of launcher;

$$(A) - \text{Tower Rotation Matrix;} \quad \vec{X}_{T_2} = (A)\vec{X}_{T_1}$$

$$(A) = \begin{pmatrix} 1 & 0 & 0 \\ 0 & c\alpha & s\alpha \\ 0 & -s\alpha & c\alpha \end{pmatrix} \qquad (B-7)$$

where:

α =   angle between the yaw axis and the vertical-launcher plane,

clockwise viewed from top;

(R) – Rocket Matrix (Marchand, 1964); $\vec{X}_{T_1} = (R)\vec{X}_R$

$$(R) = \begin{pmatrix} c\theta\, c\psi & -c\theta\, s\psi\, c\varphi + s\theta\, s\varphi & c\theta\, s\psi\, s\varphi + s\theta\, c\varphi \\ s\varphi & c\psi\, c\theta & -s\psi\, s\varphi \\ -s\theta\, s\psi & s\theta\, s\psi\, c\varphi + c\theta\, s\varphi & -s\theta\, s\psi\, s\varphi + c\theta\, c\varphi \end{pmatrix}$$

(B-8)

$$\tan\theta = \cos\psi\, \tan\theta'$$
(B-9)

where:

θ = corrected pitch angle;

θ' = measured pitch angle;

φ = roll angle;

ψ = yaw angle.

For a given time, the data from tape D-5 is interpolated to find the angles θ', φ and ψ. The matrices (T) and (A) are computed only once for each flight, while (C) is up-dated every 10 sec.

The trajectory data, originally in the format of the Wallops Island GE-635 computer, was changed to a format compatible with the University of Colorado's CDC-6400. A parabolic interpolation was used to find the altitude at any given time.

APPENDIX C

POLARIZATION OF RAYLEIGH SCATTERED RADIATION

This appendix is adapted from a private communication by the author and a colleague (Anderson and Meira, 1969).

A complete description of radiation including its polarization properties can be obtained by the use of Stokes' parameters. The following presentation is taken from Goody (1964).

Let ℓ and r refer to directions forming an orthogonal set with the direction of propagation of radiation, and I_ℓ and I_r be the intensities of the polarized components with electric fields in the ℓ and r directions respectively. Also, let:

$$U = (I_\ell - I_r) \tan 2\chi \qquad \text{(C-1)}$$

$$V = (I_\ell - I_r) \tan 2\beta \, \sec 2\chi \qquad \text{(C-2)}$$

where:

$\tan\beta$ = ratio of the axes of the polarization ellipse;

χ = angle between ℓ and the major axis.

The field of radiation can then be represented by (I_ℓ, I_r, U, V), or (I^1, I^2, I^3, I^4), where the numerals are superscripts and not

exponents. The effect of Rayleigh scattering particles is to transform radiation into $(I_s^1, I_s^2, I_s^3, I_s^4)$, with

$$I_s^i = \sum_{j=1}^{4} F_{i,j} I^j \qquad (C-3)$$

and, except for a constant factor,

$$F_{i,j} = \begin{pmatrix} (2A+3B)\cos^2\theta + A - B & A-B & 0 & 0 \\ A-B & 3A+2B & 0 & 0 \\ 0 & 0 & (2A+3B)\cos\theta & 0 \\ 0 & 0 & 0 & 5B\cos\theta \end{pmatrix}$$

$$(C-4)$$

where:

A, B = functions of the elements of the polarizability tensor;

θ = scattering angle, or angle between the directions of propagation before and after the scattering.

For incident natural light (I/2, I/2, 0, 0), and $\theta = \pi/2$, the scattered radiation is, from Eqns. (C-3) and (C-4):

I/2 (2A-2B, 4A+B, 0, 0). The measureable quantity Δ, defined as I_ℓ / I_r under these conditions, is then:

$$\Delta = \frac{2A-2B}{4A+B} \qquad (C-5)$$

which can be inverted to yield

$$A/B = \frac{2+\Delta}{2-4\Delta} \qquad (C-6)$$

Equation (C-4) can now be written, except for a (different) constant factor:

$$
F_{i,j} = \begin{pmatrix}
(2-2\Delta)\cos^2\theta + \Delta & \Delta & 0 & 0 \\
\Delta & 2-\Delta & 0 & 0 \\
0 & 0 & (2-2\Delta)\cos\theta & 0 \\
0 & 0 & 0 & 2-4\Delta
\end{pmatrix}
$$

(C-7)

Finally, for incident natural light scattered at an angle θ, we have:

$$
I_\ell / I_r = \Delta + (1-\Delta)\cos^2\theta
$$

(C-8)

Let us relate the directions $\hat{\ell}$ and $\hat{r}$ to the instrument. We shall define:

$\hat{\Sigma}$ = unit vector pointing to the sun;

$\hat{s}$ = outward unit vector along the optical axis of the monochromator;

$\hat{\ell},\hat{r}$ = unit vectors such that $\hat{\ell} \times \hat{r} = \hat{s}$ and $(\hat{\ell} \times \hat{\Sigma}) \times \hat{r} = 0$

Given $\hat{\Sigma}$ and $\hat{s}$, it then follows that:

$$
\hat{r} = \frac{\hat{\Sigma} \times \hat{s}}{\hat{\Sigma} \times \hat{s}}
$$

(C-9)

$$
\hat{\ell} = \hat{r} \times \hat{s}
$$

(C-10)

113

$$\cos\theta = \hat{s} \cdot \hat{\Sigma}, \quad |\hat{\Sigma} \times \hat{s}| = |\sin\theta| \qquad \text{(C-11)}$$

The unit vector orthogonal to $\hat{s}$ and transverse to the entrance slit, pointing away from the detector head, is defined as $\hat{p}$. The set of instrument-fixed unit vectors is completed by

$$\hat{q} = \hat{s} \times \hat{p} \qquad \text{(C-12)}$$

The plane of maximum acceptance, denoted by the unit vector $\hat{M}$ in the plane of $\hat{p}$, $\hat{q}$, is rotated by an angle δ from q (clockwise looking aft). This set is completed by the unit vector defining the plane of minimum acceptance:

$$\hat{m} = \hat{M} \times \hat{s} \qquad \text{(C-13)}$$

Another useful angle for application is γ, measured clockwise from $\hat{q}$ to the scattering plane defined by $\hat{s}$ and $\hat{\Sigma}$. Figure C-1 shows the vectors and angles in the plane perpendicular to $\hat{s}$, looking from its tip. Also shown is the angle α, defined by

$$\alpha = \gamma - \delta \qquad \text{(C-14)}$$

The angles γ and δ are more precisely defined by:

$$\cos\gamma = \hat{\ell} \cdot \hat{p}$$

$$\qquad \text{(C-15)}$$

$$\sin\gamma = \hat{\ell} \cdot \hat{q}$$
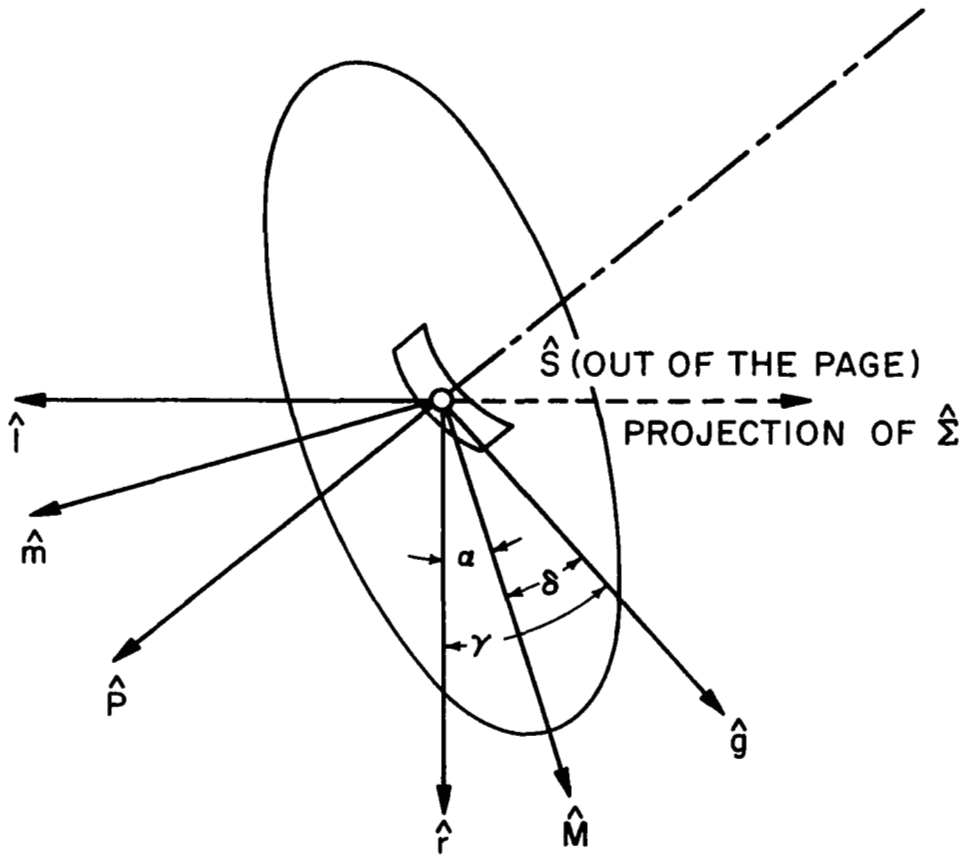
Figure C-1. Vectors in the Plane Perpendicular to Optical Axis of Instrument, and Its Acceptance Ellipse.

$$\cos \delta = \hat{m} \cdot \hat{p}$$

$$\sin \delta = \hat{m} \cdot \hat{q} \qquad \text{(C-16)}$$

From expression (C-14), we can write the equation for $\cos 2\alpha$, which will be useful later:

$$\cos 2\alpha = \cos 2\gamma \cos 2\delta + \sin 2\gamma \sin 2\delta \qquad \text{(C-17)}$$

The functions of the angles can in turn be expressed in terms of the fundamental vectors $\hat{s}$, $\hat{\Sigma}$, and $\hat{p}$. From (C-15) and (C-9) through (C-12):

$$\cos 2\gamma = 2 \cos^2 \gamma - 1 = 2 (\hat{\ell} \cdot \hat{p})^2 - 1 = 2 [\hat{r}, \hat{s}, \hat{p}]^2 - 1$$

or $\qquad \qquad \qquad \qquad \qquad \qquad \qquad \qquad \qquad \qquad \text{(C-18)}$

$$\cos 2\gamma = \frac{2 (\hat{\Sigma} \cdot \hat{p})^2 - 1}{\sin^2 \theta}$$

Also,

$$\sin 2\gamma = 2 \sin \gamma \cos \gamma = -2 (\hat{\ell} \cdot \hat{p})(\hat{\ell} \cdot \hat{q}) = 2 [\hat{r}, \hat{s}, \hat{p}] \, (\hat{r} \cdot \hat{p})$$

or $\qquad \qquad \qquad \qquad \qquad \qquad \qquad \qquad \qquad \qquad \text{(C-19)}$

$$\sin 2\gamma = - \frac{2 (\hat{\Sigma} \cdot \hat{p}) [\hat{\Sigma}, \hat{s}, \hat{p}]}{\sin^2 \theta}$$

The instrument was calibrated with unpolarized light. It is then convenient to break down the signal coming into instrument into

the linearly polarized components parallel and perpendicular to the plane of maximum acceptance (I_M and I_m respectively). In particular, if we define their ratio as

$$R = I_M / I_m \qquad \text{(C-20)}$$

then

$$I_M = \frac{R}{1+R} I$$

$$\text{(C-21)}$$

$$I_m = \frac{1}{1+R} I$$

where I is the total intensity, the sum of I_M and I_m.

The response S of the instrument is

$$S = C \left\{ (1+p) I_M + (1-p) I_m \right\} \qquad \text{(C-22)}$$

where C is the calibration of the instrument for unpolarized light and p its polarization, defined, for a linearly polarized incident intensity, as

$$p = \frac{S_M - S_m}{S_M + S_m} \qquad \text{(C-23)}$$

where S_M and S_m are the responses of the instrument when the plane of polarization of the incident radiation is respectively parallel and perpendicular to the plane of maximum acceptance of the instrument.

Combining (C-22) and (C-21), we can write:

$$S = \left\{ \frac{R(1+p)}{(1+R)} + \frac{(1-p)}{(1+R)} \right\} C.I = C.I.f \qquad (C-24)$$

thus defining the function f, which takes into account the effect of the polarization of the instrument on its response. It can be evaluated by considering Fig. C-1, from which it is seen that

$$I_M = \frac{I_r}{2}(1 + \cos 2\alpha) + \frac{I_1}{2}(1 - \cos 2\alpha)$$

and $\qquad\qquad\qquad\qquad\qquad\qquad\qquad\qquad\qquad\qquad$ (C-25)

$$I_m = \frac{I_r}{2}(1 - \cos 2\alpha) + \frac{I_1}{2}(1 + \cos 2\alpha)$$

From here on, it is a question of substituting (C-8) into (C-25) and the result into (C-20) to obtain R. The function f can then be found from (C-24):

$$f = 1 + p\left\{ \frac{[\cos(2\gamma)\cos(2\delta) + \sin(2\gamma)\sin(2\delta)]}{1 + \Delta + (1-\Delta)\cos^2\theta} \right\}(1-\Delta)\sin^2\theta$$

$$(C-26)$$

118

APPENDIX D

MOLECULAR NITROGEN AND ATOMIC

OXYGEN IONS IN THE D-REGION

In considering the photochemistry of nitric oxide the pro-
duction of nitrogen atoms is an important factor because the main
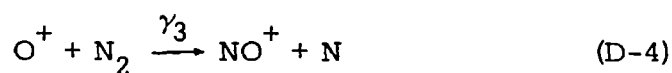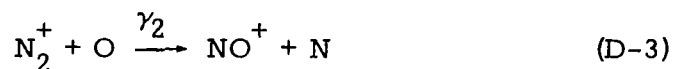loss of NO is through the reaction

$$N(^4S) + NO \xrightarrow{k_2} N_2 + O \qquad (D-1)$$
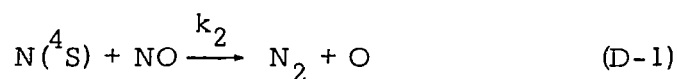
In the calculations of Chapter V we considered the dissoci-
ative recombination of NO^+

$$NO^+ + e \xrightarrow{\alpha} N + O \qquad (D-2)$$

to be the major source of N. The purpose of this Appendix is to check
the validity of that procedure in the region from 70 to 100 km.

Atomic nitrogen can also be produced by

$$N_2^+ + O \xrightarrow{\gamma_2} NO^+ + N \qquad (D-3)$$

$$O^+ + N_2 \xrightarrow{\gamma_3} NO^+ + N \qquad (D-4)$$

Densities of N_2^+ and O^+ have not been measured experimentally, however, because of their low values. These ions are primarily lost through the fast charge transfer reactions

$$N_2^+ + O_2 \xrightarrow{\gamma_4} O_2^+ + N_2 \qquad \text{(D-5)}$$

$$O^+ + O_2 \xrightarrow{\gamma_5} O_2^+ + O \qquad \text{(D-6)}$$
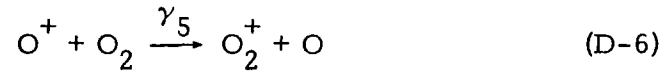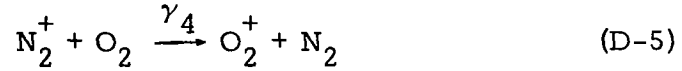
(see, e.g., Donahue, 1966). Production is from X-rays in the upper portion and from galactic cosmic rays in the lower portion of the region under consideration.

In order to evaluate the relative importance of reactions (D-3) and (D-4), we compute what the total production of ion pairs would have to be for these sources to be of the same magnitude as dissociative recombination of NO^+ (reaction D-2). Let us assume that production of O^+ and N_2^+ is a fraction of the total ion-pair production equal to the mixing ratio of neutral O and N_2. This procedure may, if anything, result in overestimating the production of these ions.

The production of N from reactions (D-2) through (D-4) is, respectively:

$$q_{NO^+} = \alpha [NO^+] \, n_e \qquad \text{(D-7)}$$

120

$$q_{N_2^+} = \gamma_2 \, [N_2^+] \, [O]$$
(D-8)

$$q_{O^+} = \gamma_3 \, [O^+] \, [N_2]$$
(D-9)

where the subscripts denote the ion lost in the process.

The equilibrium equations for N_2^+ and O^+ are:

$$[N_2^+] = \frac{q[N_2]}{[M] \, \gamma_4 \, [O_2]}$$

and
(D-10)

$$[O^+]' = \frac{q[O]}{[M] \, \gamma_5 \, [O_2]}$$

where [M] stands for the atmospheric number density and q is the total rate of ion-pair production by nonselective mechanisms (i.e., excluding NO, $O_2(^1\Delta)$, etc.).

Equating the production of N from N_2^+ and O^+ (D-8 and D-9) to that from NO^+ (D-7), we can solve for q with the help of (D-10) and (D-11). For the case of N_2^+ we have:

$$q = \frac{\alpha \, [NO^+] \, n_e \, [M][O_2]}{\gamma_2 \, [O][N_2]} \, \gamma_4$$
(D-12)

121

where q is then the total ion-pair production rate necessary for the N_2^+ reaction (D-3) to be a source of N as important as the NO^+ reaction (D-2). Similarly, the O^+ reaction (D-4) will be important if q is:

$$q = \frac{[NO^+] n_e [M][O_2]}{\gamma_3 [O][N_2]} \gamma_5 \qquad (D-13)$$

The rate coefficients for reactions (D-3) through (D-6) are:

$$\gamma_2 = 2.5 \times 10^{-10} cm^3 \ sec^{-1} \ (Ferguson \ et \ al., \ 1965 \ );$$

$$\gamma_3 = 2 \times 10^{-12} cm^3 \ sec^{-1} \ (review \ by \ Fite, \ 1969);$$

$$\gamma_4 = 1 \times 10^{-10} cm^3 \ sec^{-1} \ (review \ by \ Fite, \ 1969);$$

$$\gamma_5 = 2 \times 10^{-11} cm^3 \ sec^{-1} \ (review \ by \ Fite, \ 1969).$$

The dissociative recombination coefficient of NO^+ is given in Chapter V.

Using the atmospheric data from Appendix E, we computed q from Eqns. (D-12) and (D-13):

Height (km)	$q(cm^{-3} sec^{-1})$ for N_2^+	$q(cm^{-3} sec^{-1})$ for O^+
70	1.7×10^{-3}	9.0×10^{-2}
80	3.8×10^{0}	1.4×10^{2}
90	3.6×10^{2}	1.9×10^{4}
100	2.9×10^{3}	1.5×10^{5}

These values are higher than the accepted ion-pair production rates by X-rays and cosmic rays by at least one order of magnitude (see, e.g., Bourdeau et al., 1966). We therefore conclude that reactions (D-3) and (D-4) can be neglected as sources of ground state atomic nitrogen in a first approximation, between 70 and 100 km. This is true in spite of the fact that a substantial fraction of the nitrogen atoms are required to be in the excited (^2D) state by the reaction scheme used in Chapter V.

APPENDIX E

OTHER EXPERIMENTAL DATA

In other Chapters we made use of experimental data from different sources in the interpretation of our results. Also, for mesospheric ozone and atomic oxygen, a theoretical model was used. We find it convenient to present them together here.

Solar Ultraviolet Flux

Use was made of the spectrum reported by Tousey (1963) and presented in digitized form by Brinkmann et al. (1966), for the calculation of the synthetic Rayleigh scattering background. Figure E-1 shows the solar flux before and after convolution with the slit functions of the monochromator, for the wavelength range of our instruments. The gross features of the smoothed spectrum can be easily correlated with those in the flight data (Fig. B-8). Of particular interest is the region around 2150 Å, where the solar flux is higher than at neighboring regions. The coincidence of this maximum with the (1,0) gamma band of nitric oxide makes the precise subtraction of the Rayleigh scattering background of even greater importance.
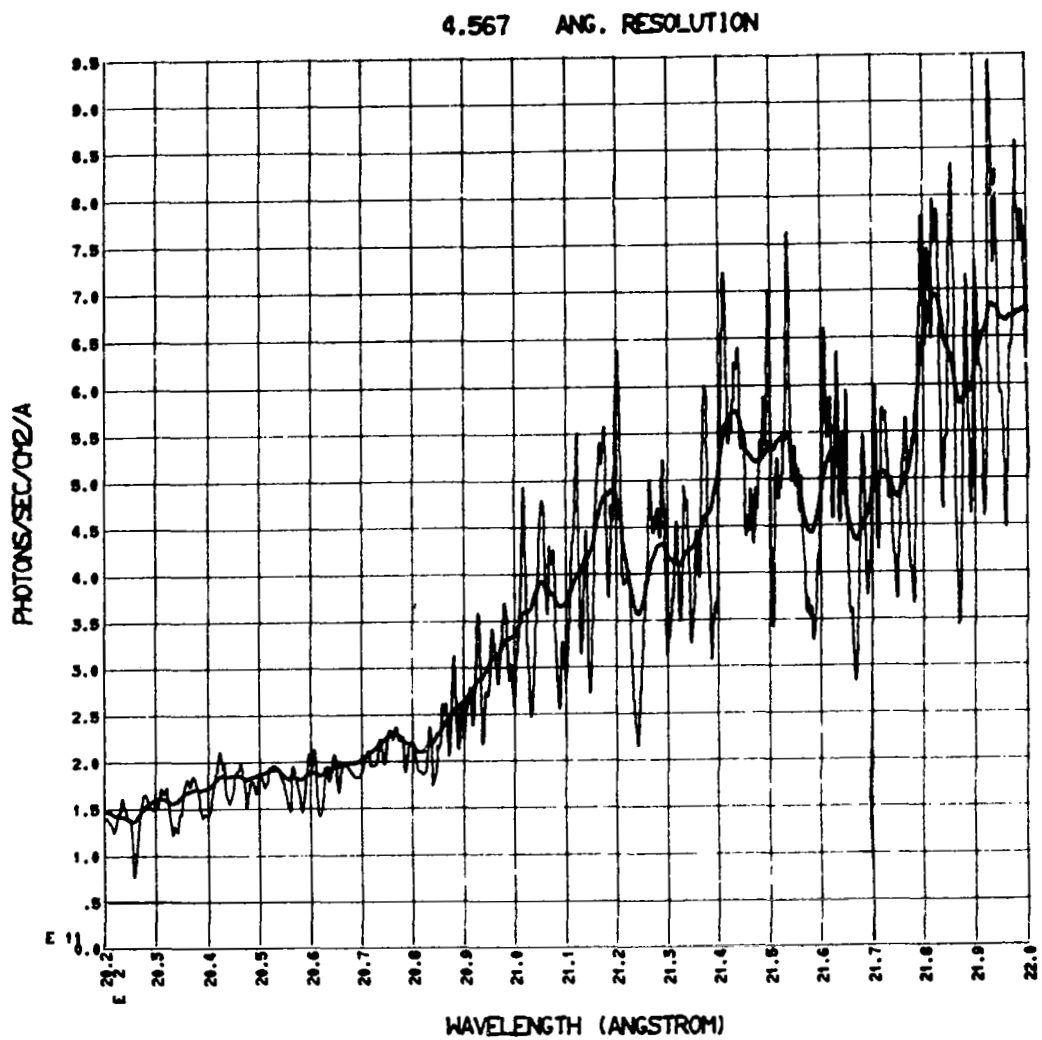
Figure E-1. High Resolution Solar Spectrum (Brinkmann et al. 1966) and Smoothed (4.6Å) Spectrum.

126

Solar Lyman-alpha Flux

The attenuation of the solar Lyman-alpha flux was measured on both days of our experiments by University of Illinois – Geophysical Corporation of America ionospheric payloads which included nitric oxide-lithium fluoride ionization chambers. In the calculation of nitric oxide production rates we used the Lyman-alpha optical depths derived from these experiments (L. G. Smith, 1969).

The solar Lyman-alpha flux outside the atmosphere has been measured several times and most of the results found to be between 3 and 7 $erg/cm^2/sec$ (see, e.g., Weeks, 1967). The same author found that the measurements with a corresponding smoothed monthly sunspot number above 40 have a mean of 6.1 $erg/cm^2/sec$, while those with a sunspot number below 40 have a mean of 4.3 $erg/cm^2/sec$. Within the first group (high sunspot number) he also found that the lower Lyman-alpha fluxes correspond to daily values of the solar radio flux at 10.7 cm below 170×10^{-22} $W/m^2/Hz$. From the ESSA Solar-Geophysical Data (1969) we find that the smoothed monthly Zurich sunspot number was 105 and 121 for January and February 1969, respectively; the daily values of the 10.7 cm radio flux were 126 and 130×10^{-22} $W/m^2/Hz$ for 31 January and 6 February 1969, respectively. Although the ionization chambers mentioned above were not calibrated, there are indications that their currents were relatively high on both occasions, compared to other flights with similar

chambers (L. G. Smith, 1969). All this evidence led us to adopt

5.5 erg/cm^2/sec as the solar Lyman-alpha flux outside the atmosphere.

Neutral Atmosphere Temperatures and Densities

There are three distinct regions that must be considered according to the source of the data.

Below 96 km, we used the data derived from rocket grenade experiments flown on the same days as our experiments, roughly two hours later (W.S. Smith, 1969). The accuracy of these data is questionable in the upper portion of their useful range; however, we only need to know well the neutral atmospheric densities in the calculations of the Rayleigh scattering background, below about 85 km (see Chapter III). Above this height, the neutral atmosphere enters only in photochemical calculations which are approximate anyway. We shall therefore not concern ourselves also with the variability of the atmosphere above 96 km, where we use model density profiles (see below), beyond the variations allowed for in the models themselves.

Between 96 and 120 km, the mean was taken of the "January, 30 °N" and the "January, 45 °N" tables of the U.S. Standard Atmosphere Supplements, 1966.

For the region above 120 km, use was made of the equations suggested in the U.S. Standard Atmosphere Supplements, 1966, for

128

the diurnal, seasonal, geomagnetic and solar activity effects on the "exospheric temperature." The 10.7 cm solar flux at the time of the launchings and the geomagnetic indices seven hours earlier were (ESSA Solar - Geophysical Data, 1969):

	$F_{10.7 \text{ cm}}$	K_p (-7 hours)
31 January 1969	$126.4 \times 10^{-22} \text{ W/m}^2/\text{Hz}$	2+
6 February 1969	$138.5 \times 10^{-22} \text{ W/m}^2/\text{Hz}$	1

From the same source, the 3-month average of the solar radio flux at 10.7 cm is found to be $155.4 \times 10^{-22} \text{ W/m}^2/\text{Hz}$. The resulting "exospheric temperature" is then found to be approximately 1100 $^\circ$K for both occasions, and this value is used to select the appropriate tabulation of temperature and number densities of N_2, O_2 and O in the U.S. Standard Atmosphere Supplements, 1966.

Atomic oxygen densities below 80 km are from time-dependent photochemical calculations for an oxygen- hydrogen atmosphere (Park and London, 1970).

The atomic oxygen densities in the region from 80 to 120 km were adopted from Colegrove et al. (1965) to fit the other models at both limits.

Ozone densities are from the same calculations as for atomic oxygen (Park and London, 1970). The ozone profile measured under

129

twilight conditions by Weeks and Smith (1968) by absorption spectroscopy is also considered in some instances.

Figures E-2 and E-3 show the temperature and number density profiles employed.

Electron Densities

Below 97 km, we used the values measured by the University of Illinois (Mechtly, 1970) with a probe and propagation technique (Mechtly, 1967). The data were smoothed to conform with the lower altitude resolution of the other experiments. Real height electron density profiles derived from the Wallops Island ionosonde were used to extend the measurements upward, after a minor adjustment of the lower portion for a better fit with the rocket profiles. Figure E-4 shows the resulting electron density profiles for both days.

Positive Ion Densities

Abundances of the positive ions NO^+ and O_2^+ relative to the total positive ion density were taken from Narcisi and Bailey (1965), for the region below 82 km. Above 85 km, the ion currents from a mass spectrometer flown by Narcisi on 31 January 1969 (Narcisi, 1969) were interpreted in terms of ratios of the densities of the same ions to the total positive ion density, a procedure which implies neglecting ions compared to electrons. Figure E-5 shows the adopted density ratios in the 70 to 150 km region.
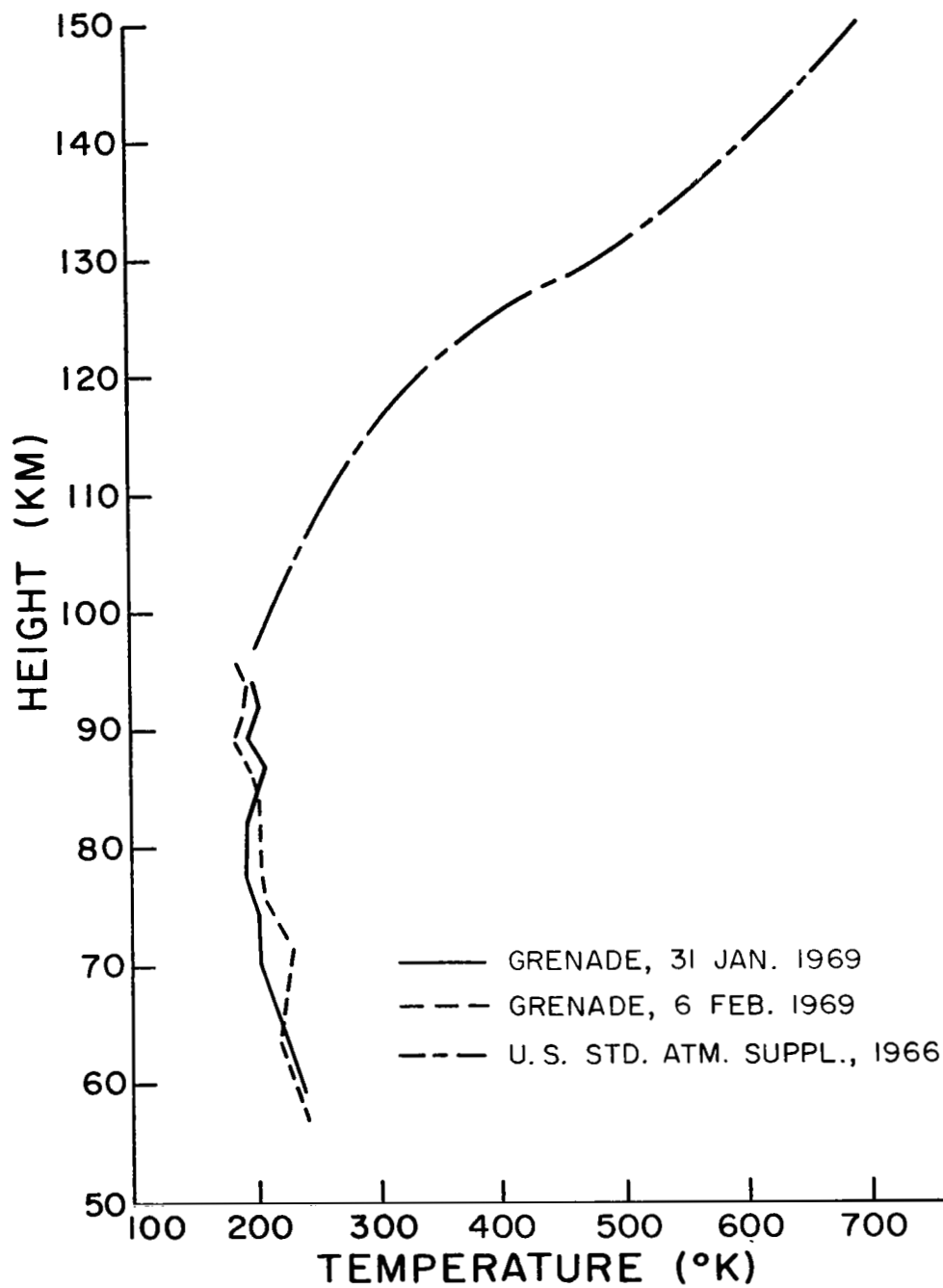
Figure E-2. Temperature Profiles from Grenade Experiments and U.S. Standard Atmosphere Supplements, 1966.
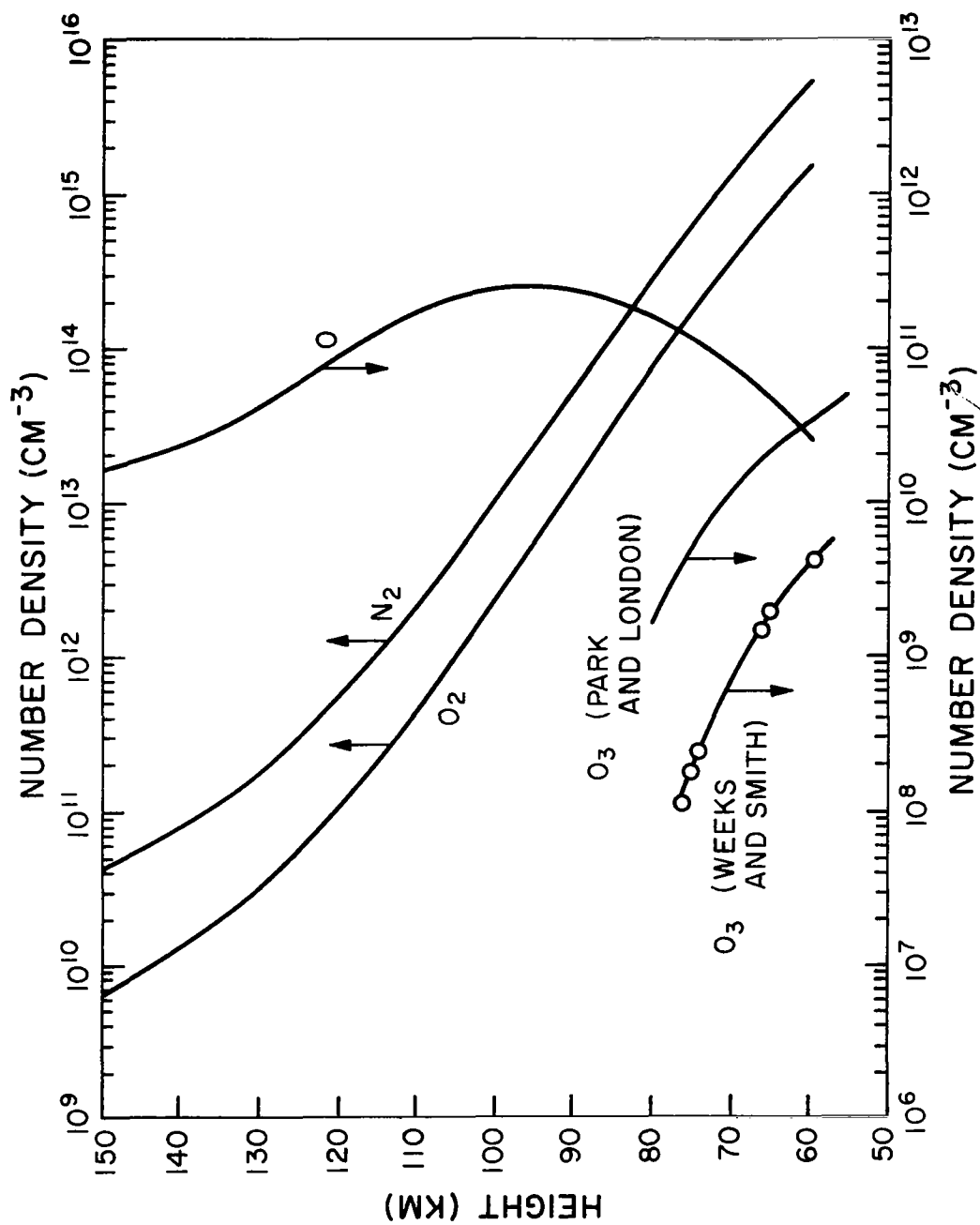
Figure E-3. Atmospheric Density from Measurements and Models
(see text). Upper Scale for N_2 and O_2; Lower Scale
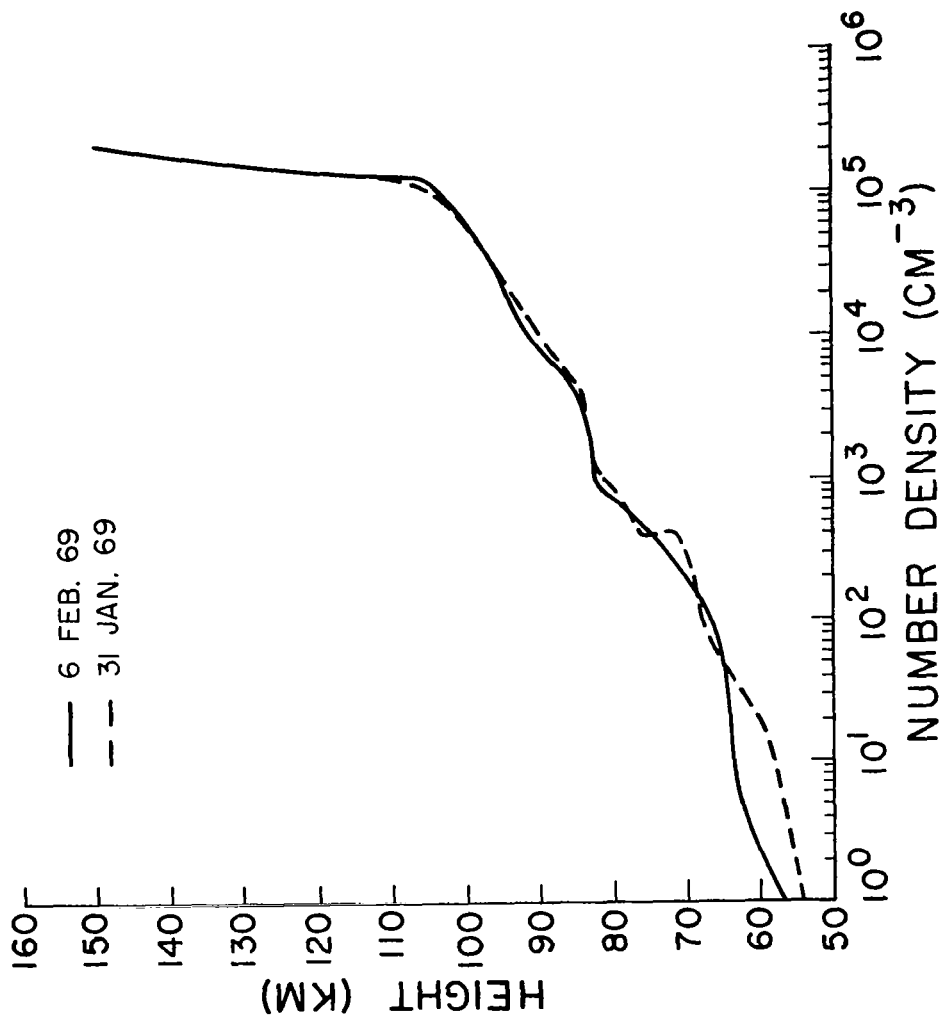for O_3 and O.

Figure E-4.   Electron Density Profiles from Rocket and Ionosonde
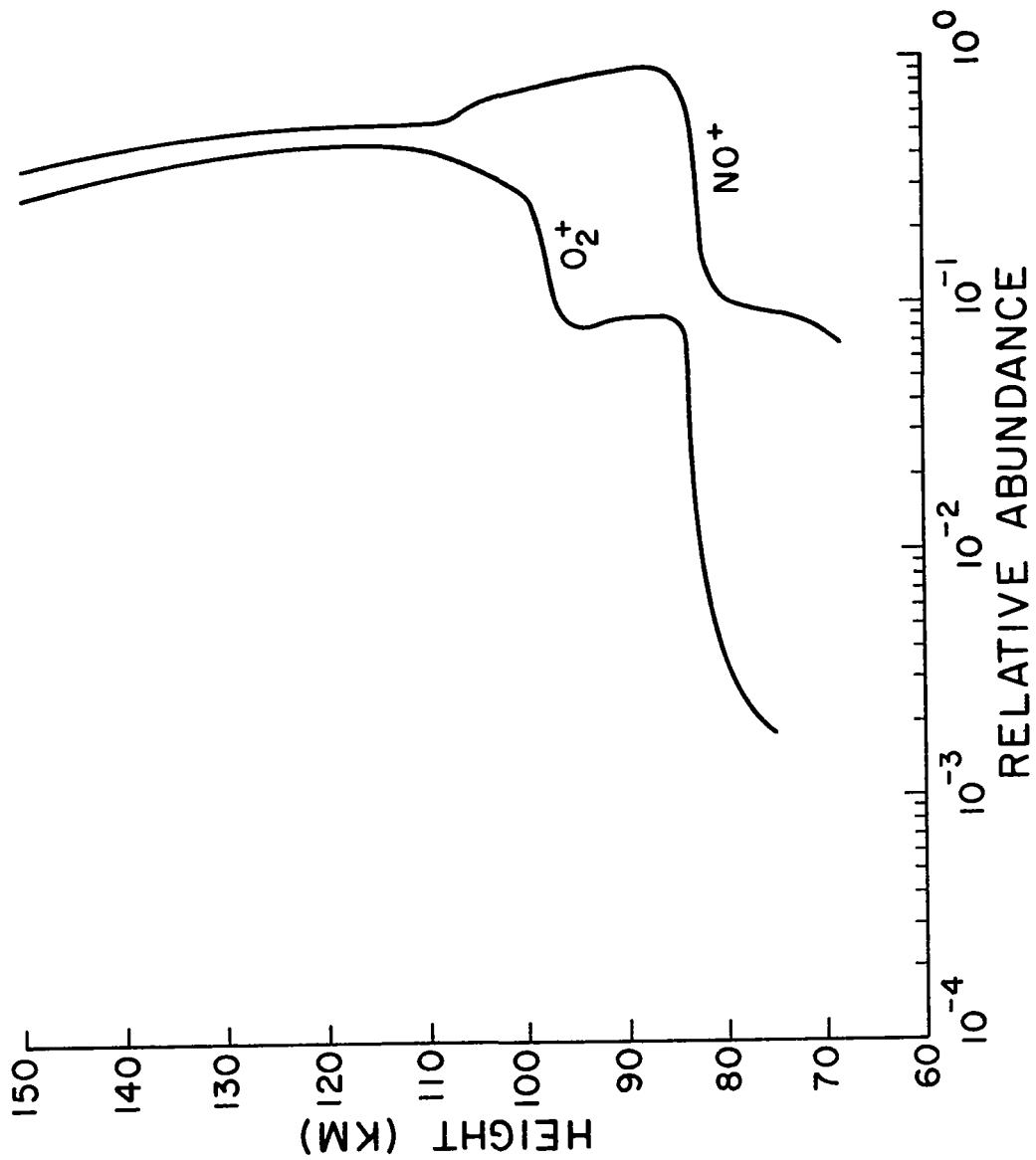Data.

Figure E-5. Ratios of NO^+ and O_2^+ Number Densities to the Total Positive Ion Density.